2015

Fabrication and Study of Graphene-Based Nanocomposites for Sensing and Energy Storage

Matthew McInnis
University of Central Florida

STARS Citation

McInnis, Matthew, "Fabrication and Study of Graphene-Based Nanocomposites for Sensing and Energy Storage" (2015). *Electronic Theses and Dissertations, 2004-2019*. 5007.
https://stars.library.ucf.edu/etd/5007

FABRICATION AND STUDY OF GRAPHENE-BASED NANOCOMPOSITES FOR SENSING AND ENERGY APPLICATIONS

by

MATTHEW D. MCINNIS
B.S. University of Central Florida, Orlando

A dissertation submitted in partial fulfillment of the requirements
for the degree of Doctor of Philosophy
in the Department of Chemistry
in the College of Sciences
at the University of Central Florida
Orlando, Florida

Summer Term
2015

Major Professor: Lei Zhai

ABSTRACT

Graphite is an allotrope of carbon made up of atomically thin sheets, each covalently bound together, forming a π-conjugated network. An individual layer, called graphene, has extraordinary electrical, thermal and physical properties that provide the opportunity for innovating new functional composites. Graphene can be produced directly on a metallic substrate by chemical vapor deposition or by chemical oxidation of graphite, forming a stable aqueous suspension of graphene oxide (GO), which allows for convenient solution processing techniques. For the latter, after thermal or chemical reduction, much of the properties of the starting graphene remerge due to the reestablishment of π-conjugation.

The π-conjugated basal plane of graphene has been shown to influence the crystallization of π-conjugated polymers, providing thermodynamically strong nucleation sites through the relatively strong π-π interactions. These polymers can homocrystallize into 1-D filaments, but when nucleated from graphene, the orientation and geometry can be controlled producing hierarchical structures containing an electrical conductor decorated with wires of semi-conducting polymer. The resulting structures and crystallization kinetics of the conjugated polymer, poly(3-hexylthiophene-2,5-diyl) (P3HT) nucleated by graphene was studied. Further, field-effect transistors were developed using graphene as both the electrodes and the polymer crystallization surface to directly grow P3HT nanowires as the active material. This direct crystallization technique lead to higher charge mobility and higher on-off ratios, and this result was interpreted in terms of the morphology and polymer-graphene interface.

Besides these thin-film technologies, neat GO suspensions can be lyophilized to produce monolithic, free-standing aerogels and then reduced to produce an electrically conductive porous material with a surface area greater than 1000 m^2/g. The present research focuses on functionalizing the aerogel surfaces with metal nanoparticles to increase electrical conductivity and to impart functionality. Functionalization was carried out by adding a metal salt as a precursor and a chelating agent to inhibit GO flocculation. The GO and metal salt were simultaneously reduced to form rGO aerogels homogeneously loaded with metal nanoparticles. The size and distribution of these nanoparticles was controlled by concentration and chelating agent identity and abundance. Optimum aerogel formulations were used as a functioning and reversible conductometric hydrogen gas sensor and as an anode in an asymmetric supercapacitor with excellent properties.

for the best wife

ACKNOWLEDGEMENTS

Firstly, I acknowledge Jesus Christ as my Lord and Savior for whom all that I do is done. Thank you to Dr. Zhai who has been instrumental in the miraculous conversion of a construction worker to a chemist. More than just the good advice and constant availability, the quiet example you've been to me in both my personal and professional life will never be forgotten.

Thank you to my committee members Dr. Cherie Yestrebsky, Dr. Howard Miles, Dr. Shengli Zou, and Dr. Quanfang Chen for taking the time to evaluate and guide me through candidacy and defense.

I would like to thank my group members, labmates and classmates through both undergrad and graduate school at UCF, for this I am truly grateful. Additionally, I'd like to thank the Nanoscience Technology Center and the Department of Chemistry for the support and platform needed to study and obtain this degree. I'd like to thank Jordan, Jean, Joe and Astha for their friendship. Our long conversations and comradery made the lab feel like a home. Thanks to all the folks at Garmor for your support through this process.

Lastly, I couldn't have done this without the love and support of my family. Thank you so much, especially to my sister Andrea who pulled my head from the sand and pushed me down this road.

TABLE OF CONTENTS

LIST OF FIGURES

LIST OF TABLES

CHAPTER 1. BACKGROUND

1.1 Graphene: Structure and Properties

Graphene is a relatively new and exciting material with a unique structure resulting in high electrical and thermal conductivity, incredible mechanical strength, chemical stability, and interesting optical properties all while being just one atom thick. These properties result new in new opportunities in a wide variety of fields, such as in energy storage and conversion, sensing, and polymer composites. With the emergence of new synthetic techniques and commercial availability of graphene, an emerging interest has focused on adapting graphene into pre-existing technologies for enhanced performance, and producing novel functional materials.

Motivated by intense scientific and industrial interest in this material, these research projects were focused on the synthesis and design and graphene-based composites to understand and overcome the challenges associated with utilizing graphene and to produce functional composites. Graphitic surfaces are those made up by each atomically thin layer of carbon in graphite and dependent on their arrangement can be fullerenes, carbon nanotubes or graphene (Figure 1). Additionally, chemical oxidation of graphite can lead to so-called graphene oxide (GO) which can be dispersed as single layers in various solvents due to the oxygen functional groups imparted by the oxidation. After solution processing, the GO can be reduced to RGO, regaining much of the original properties of graphene (Figure 2).

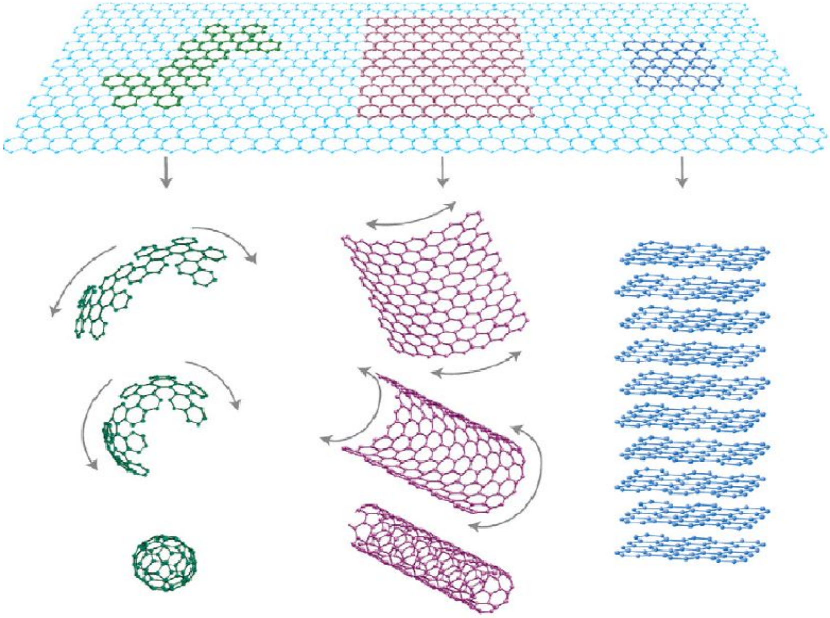

Figure 1. Graphene sheet adapting different conformations to form (from left to right) fullerenes, carbon nanotubes and graphite.[1] [Reproduced with permission from Nature Publishing Group]

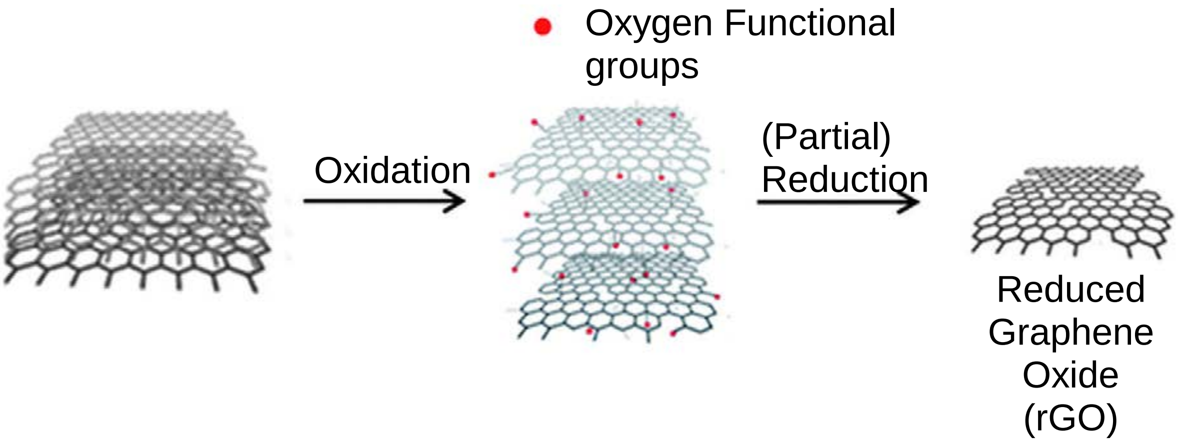

Figure 2. Schematic representation of the process of oxidation of graphite followed by the reduction of GO to RGO.

Although the properties of graphene are unique and sought after, its chemical stability makes it difficult to utilize as a functional material.

1.2 Conjugated Polymer Crystallization from Graphitic Surfaces

The directed crystallization of polymers, seeded by graphitic surfaces such as CNTs can produce hierarchical structure in polymer-graphene composite materials on the nanoscale.[2]. Both from dilute solutions and from the melt, conjugated polymers are known to self-assemble from into intrinsic one-dimension charier transport paths by crystallization primarily through the π-conjugated face grows to form lamellar structure (Figure 3).[3] Crystallization nucleated by graphene then proceeds primarily one-dimensionally, but perpendicularly graphene basal plane axis due to CP-graphene π-π stacking interaction. This affords a unidirectional alignment of the π-π stacking crystallization direction, providing better charge mobility from the graphene surface, which has been a limitation of widespread utilization of conjugated polymers. Similar structures were made using carbon nanotubes (CNTs) by our group.[2a]. Liu et al. used a chloroform solution of CNTs and P3HT was ultrasonicated for two hours in an ice-water bath to form a stable dispersion of CNTs. P3HT was then dissolved in hot anisole (a marginal solvent), a small amount of the CNT-P3HT dispersion was added, and the mixture was cooled and aged resulting in deep purple dispersions which were stable for months at room temperature. As seen in Figure 4, transmission electron microscopy (TEM) revealed CNTs with highly dense wires of P3HT nanowires from the surface with no observable free P3HT nanowires in solutions. In-situ UV-Vis spectroscopy revealed that the 1D P3HT quasi-isothermal nanowire growth rate to follow first-order kinetics.

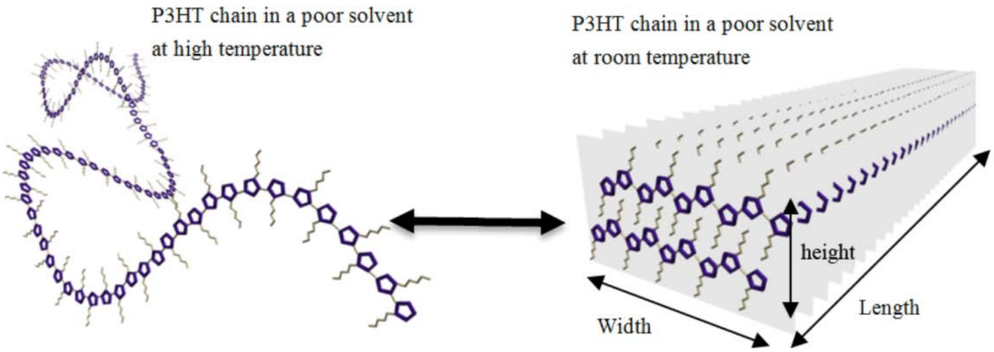

Figure 3. Schematic of the crystallization of P3HT into an ordered, lamellarly stacked wire.[4] [Reproduced with permission from Beilstein 2012]

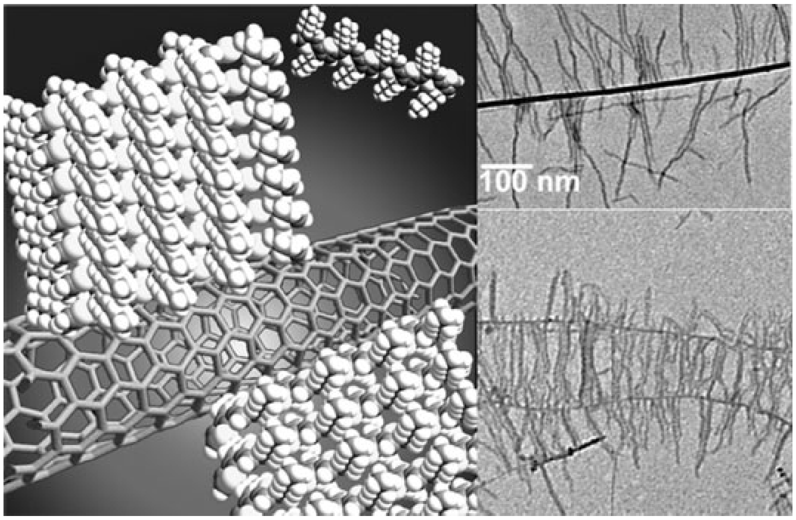

Figure 4. Carbon nanotubes induced crystallization of conjugated polymer[2a] [Reproduced with permission from Wiley]

Current organic field effect transistors (OFET) device performance limitations are set by the crystallinity and contact resistance with metal electrodes of the semiconducting channel material.[5] Graphene-P3HT composite materials has high induced crystallinity imparted on P3HT by the graphitic surface, and necessarily optimum contact .[6]

1.3 Asymmetric Supercapacitors Using Metal-Decorated Graphene Aerogels

Asymmetric supercapacitors (ASCs) have played a leading role in realizing energy storage devices with high energy and power densities. While both anode and cathode materials are important for high performance ASCs, more research effort has been devoted to developing cathode materials because the energy source of an ASC is mostly attributed to the cathode. However, the development of anode materials is essential in order to achieve high power density as well as stable long-term cycle life of ASCs. In this study, functionalized graphene aerogel (GA) decorated with palladium (Pd) nanoparticles is used as an efficient ASC anode material. The high surface area (328 m^2 g^{-1}) and low electrical resistivity (a 50 times lower than one without Pd) of the GA composite grants a high specific capacitance (175.8 F g^{-1} at 5 mV s^{-1}), excellent rate capability (48.3% retention after a 10 fold increase of scan rate), and remarkable reversibility. ASCs assembled from manganese dioxide (cathode) and GA composite (anode) show stable extended cell voltage, fast charge-discharge capability, excellent cycle stability (89.6% retention after 3,000 cycles), and high energy and power densities (average of 13.9 Wh kg^{-1} and 13.3 kW kg^{-1}). These results demonstrate the great potential of the GA composite as an efficient anode material for high performance energy storage devices.

CHAPTER 2. EXPERIMENTAL

2.1 Procedures and Techniques for CHAPTER 3

2.1.1 Materials and Instrumentation.

Regioregular-P3HT (M_n = 18kDa) was synthesized in our lab using the Grignard metathesis method. Molecular weight of rr-P3HT was determined by size exclusion chromatography (SEC, A JASCO HPLC system equipped with PL gel 5 μm MIXED-C coluMn) using polystyrene as standard and tetrahydrofuran as the eluent. Morphology of the graphene/P3HT film surface was characterized by scanning electron microscope (SEM, ZEISS ULTRA55) with 5kV acceleration voltage. Transmission electron microscopy (TEM) images were obtained on a JEOL 1011 electron microscope at 100 kV. The digital image was taken with a HTC Thunderbolt camera-phone. Raman spectroscopy was performed using a Renishaw InVia Raman microscope comprised of a laser (532nm line of solid Si laser), a single spectrograph fitted with holographic notch filters, and an optical microscope (a Leica microscope with a motorized XYZ stage) rigidly mounted and optically coupled to the spectrograph. The spectrometer was calibrated with a Si standard using a Si band position at 520.3 cm-1. Graphene platelets were purchased from Angstron Materials, Dayton, OH (item number: N008-100-P). QCM experiments were carried out on polished EQCM crystals coated with a 100 Å Au. QCM experiments were performed on a Maxtek Research QCM system (Inficon). FLG was synthesized by chemical vapor deposition according to literature procedure using a Lindburg Blue M tube furnace, with hydrogen and methane purchased from Airliquide. The catalytic copper substrate (0.025mm thick 99.8% metals basis) and Iron(III) chloride (anhydrous, 98%) were purchased from Alfa Aesar. Anisole, 99%, extra pure was purchased from Acros Organics. PMMA was purchased from TCI.

Chloroform was purchased from Fisher Scientific (C607-4). All chemicals were used as received. The digital image was taken with a HTC Thunderbolt camera-phone.

2.1.2 Nanowire formation on graphene platelets.

2 mg P3HT and 2 mg GPs were added to 4 mL of chloroform, and sonicated using a horn sonicator. Then 40 µg of this solution was added as crystallization seeds into a hot (80OC) solution of 0.1 mg/mL P3HT in anisole and cooled at >20 OC/min and left overnight before transfer to a TEM grid.

2.1.3 Transfer of FLG to substrates.

A square piece of graphene coated copper was taped to a microscope slide and a 3 mg/mL solution of PMMA in chloroform was cast on it before spinning at 300 rpm for 20 seconds followed by 1300 rpm for 30 seconds. The foil was placed atop a 1.0 M FeCl3 solution until the bottom copper layer was completely etched away. Next the target substrate was carefully placed into the solution, to one side of the suspended film, angled underneath at around 30O from vertical, and slowly raised after touching the edge of the film. The target substrate was wetted with water, lifting the film which floated, and removed via osmosis by touching the water with a paper towel three times and allowed to dry in air. The film adhered well enough at this point to rinse the surface thoroughly with acetone to remove the PMMA film, and dried.

2.1.4 QCM analysis.

A general procedure for the QCM analysis is as follows. The quartz stage (coated or bare) on the holder was immersed into a hot solution of anisole (with or without P3HT) which sat into a hot water bath equipped with a thermometer and the QCM monitor was begun. The temperature was held constant until the QCM equilibrated to a point where the mass change was constant. The solution was cooled in stages to room temperature while monitored, then lifted out of solution and placed on a paper towel face-up to wick away excess solution and allowed to air dry. Once dry, the sample was placed under vacuum overnight before characterization.

2.2 Procedures and Techniques for CHAPTER 4

2.2.1 Reduction of graphene oxide

GO powder (Cheap Tubes Inc) was diluted in deionized (DI, 30 ml) water with sonication followed by 24 hrs magnetic stirring. To obtain chemically reduced-GO (RGO) solution, 200 µL of 5% NH_3 aqueous solution is added to adjust the pH of solution, and 30 µL of hydrazine solution is added, and heated at 90˚C for 60 min. The reduction efficiency was determined from carbon sp^2 fraction using x-ray photoelectron spectroscopy (XPS). From XPS spectrum of RGO sheets of different reduction efficiency , the carbon sp^2 fractions are calculated as 80 % for 60 min of reduction time of RGO sheets.[7]

2.2.2 Electrode fabrication

Our devices are fabricated onto heavily doped silicon (Si) substrates with 250 nm thermally grown silicon dioxide (SiO_2). Pd patterns (L : W = 5µm : 25µm) are defined using ebeam lithography (EBL) and ebeam evaporation of Cr (3 nm)/Pd (27 nm) followed by lift off. We optimized the dielectrophoresis (DEP) assembly technique to obtain a thin RGO film in large channel geometry. RGO solution (3 µL) is dropped between Pd source and drain, and an AC voltage of 5 V with 1 MHz frequency is applied for 30 sec. Room-temperature current-voltage characteristics show that the assembled RGO sheet has a standard ambipolar behavior as an intrinsic property of graphene, with a mobility of ~0.1 cm^2/Vs. RGO sheets are then cut by second EBL (L:W=2μm:25μm) and subsequently oxygen plasma etched for 2 min. Finally, the devices are kept into acetone to remove the residual PMMA on the devices. We investigate the thickness of RGO sheets using AFM and all the films have similar morphology with an average thickness of ~20 nm.

2.2.3 P3HT growth on rGO electrodes

For growth of P3HT nanowires on RGO electrodes, P3HT and anisole were purchased from Rieke Metals, Inc. and Acros Organics (New Jersey, USA) respectively and used as received. In this experiment, no additional surface treatment such as octadecyltrichlorosilane (OTS) or hexamethyldisilazane (HMDS) was performed on SiO_2 surface. P3HT nanowires were grown across the gap between the RGO electrodes through controlled crystallization from the marginal solvent anisole under nitrogen atmosphere. In a glovebox, ~2 mg P3HT (M_w = 34 kDa) was dissolved in 10 mL of anhydrous anisole by heating to 90°C for 2 hours. This solution was diluted to the appropriate concentration (between 0.01 and 0.35 g/L) with more anisole and kept at 90°C on a hotplate until use. To ensure the accuracy of the solution concentration, an aliquot of this stock was taken and diluted with chloroform for UV-Vis spectroscopic analysis against a calibration curve at 450 nm absorbance. Devices with RGO electrode pairs each were loaded into separate vials and heated to 90°C. 2 mL of the P3HT solution was pipetted into the vials, completely covering the devices. The vials were then capped and cooled at a rate of 20°C/hr by decreasing the hotplate temperature in increments of 10°C every 30 minutes down to room temperature without stirring. They were then kept at room temperature for 12 hours. During this time the translucent orange yellow solutions became an opaque purplish red color, indicating the crystallization of free P3HT in solution. The P3HT solutions were then pipetted out and replaced with room temperature fresh anisole 5 times to remove any P3HT crystallites from solution. The devices were then removed from vials, allowed to air-dry for 1 hour and further annealed at 130°C for 10 minutes.

2.2.4 Preparation of control electrodes

As a control experiment, similar devices containing Pd instead of rGO electrodes were prepared with P3HT as the active material. P3HT nanowires, as expected, did not grow on devices prepared containing Pd electrodes with the same gap dimensions so a suspension of P3HT nanowires were deposited by drop casting from P3HT nanowires solution. The P3HT nanowire solution was prepared in the same manner outlined above, except that the solution was cooled in a vial containing no device. After drop-casing, the drying and annealing steps were identical to those for the RGO/P3HT devices.

2.2.5 Characterization.

TEM was accomplished using a Jeol TEM-1011. Tapping mode atomic force microscopy (AFM) images were acquired by Dimension 3100 AFM (Veeco). The scanning electron microscopy (SEM) images were taken using Zeiss Ultra 55 SEM with an accelerating voltage 1 kV. Raman spectroscopy was performed using a Renishaw InVia Raman microscope comprised of a laser (532 nm line of solid Si laser), a single spectrograph fitted with holographic notch filters, and an optical microscope (a Leica microscope with a motorized XYZ stage) rigidly mounted and optically coupled to the spectrograph. The spectrometer was calibrated with a Si standard using a Si band position at 520.3 cm^{-1}. The electrical transport measurements of SWNT array were carried out by DL instruments 1211 current preamplifier and a Keithley 2400 source meter interfaced with LabView program. The electrical transport measurements of the OFETs with different reduction times of RGO were performed using Hewlett-Packed (HP) 4145B semiconductor parametric analyzer connected to a probe station inside an enclosed glove box system with nitrogen (N_2) gas flow. A total of 18 devices were investigated within each category.

2.3 Procedures and Techniques for CHAPTER 5

2.3.1 Reagents and Instrumentation.

All aqueous solutions were prepared from triply distilled water with a resistivity of 18 MΩ/cm (Barnstead B-Pure). Potassium hexachloroplatinate, palladium(ii) chloride, nickel(ii) chloride, potassium permanganate, and sulfuric acid were obtained from Acros. Graphene oxide was produced from powdered graphite (Dixon). Silver paste (SPI 05001-AB) used to make electrical contact with the aerogels. Dry ice was produced in-house using a syphon-tube equipped carbon dioxide tank (Liquidaire). Lyophilization was carried out using a Labcono freeze drying chamber at 20 µBarr with the collector set at -52^{o}C. The temperature was monitored using a type-K thermocouple. All chemicals were used as received unless otherwise specified.

2.3.2 Synthesis of Metal Nanoparticle Decorated Graphene Oxide Aerogels.

GO was prepared by modified Hummers method starting from graphite powder. Graphite was oxidized by concentrated H_2SO_4 and $KMnO_4$ and the resulting GO was purified and isolated via centrifugation then dried under vacuum. The GO was then sonicated in water at 40W for 30 minutes to create a 10mg/mL stock solution. The solution was then diluted with an appropriate amount of metal salt solution to form 1 mL solutions in straight-walled vials. The solutions were then frozen vertically along the length of the vial at -72°C by placing the dispersed GO/metal salt solution onto dry ice. Lyophilization was performed for 24 hours. The lyophilized samples were then visually inspected to determine whether or not they had formed stable aerogels. The light brown GO aerogels were placed in a 4 inches quartz boat and the boat was placed in a quartz-tube furnace with a 22 mm inner diameter for high temperature reduction. The 12 inch furnace has a single heating zone of 4 inches for the desired temperature. The chamber was evacuated to obtain a base vacuum pressure of 10 mtorr. Hydrogen gas was introduced to the chamber at a flow rate of 150 sccm, the furnace was heated to 400^{o}C at a rate of 10^{o}C/min and was maintained at 400^{o}C for 60 min for the reduction of the metal salts and to form RGO. After the 60 min, the chamber was further heated to 900^{o}C at a rate of 20^{o}C/min for the particle formation. This process reduced the metal salts to metals and produce nanoparticles in addition to reducing the GO.

2.3.3 Preparation of Pt and Pd solutions with GO with chelating agent

GO was prepared by modified Hummers method starting from graphite powder. Graphite was oxidized by concentrated H_2SO_4 and $KMnO_4$ and the resulting GO was purified and isolated via centrifugation then dried under vacuum. A 100 mM stock solution of EDTA- or acetate-ligated metal ions was prepared by slowly adding 0.002 moles of $PdCl_2$, $PtCl_2$, or $PtCl_4$ into 20mL of a 100 mM chelating agent solution while stirring. Both the Pd and Pt salts required refluxing for 30 minutes to achieve dissolution and were used immediately after cooling to room temperature. After appropriate dilution of the metal ligand complexes to desired concentration with a total volume of 800 µL, 200 µL of a freshly sonicated (15 minutes Branson S-450D horn sonicator at 10% amplitude) 20 g/L suspension of graphene oxide was added and thoroughly mixed in a 1 cm x 1 cm plastic cuvette. Each solution was then placed onto a block of dry ice and allowed to freeze fully (~20 minutes) before lyophilization. The lyophilized samples were then visually inspected to determine whether or not they had formed stable aerogels, and then placed into a tube furnace for reduction. Reduction procedures for these samples were identical to those used in the metal-loaded GO aerogels in section 2.3.2

2.4 Procedures and Techniques for CHAPTER 6

2.4.1 Electrical Measurement of Aerogel Response to Hydrogen.

Procedures for fabricating aerogels used for hydrogen sensing are the same as those outlined in chapter 5. Aerogels were adhered to an acrylic microscope slide (1” x 3” X 1/8”) using silver paste and dried, allowing connection to leads from a CHI 660D electrochemical workstation. The device was then placed into a home-built controlled gas flow apparatus equipped with a gas proportionator (Matheson Trigas). Because the aerogels show relatively significant changes in resistivity due to temperature fluctuations, the chamber containing the aerogel was placed into a thermostat controlled water bath (Buchi 490). Electrical measurements were carried out in a custom-made apparatus designed to house the sample, regulate its temperature, and expose it to a regulated gas flow of controlled composition. The sensing response of the graphene aerogels was measured in by monitoring the current passed through an aerogel over time with a source-drain voltage of 1 V. After establishing a baseline current under flow of pure argon, the valve on a flow regulator was opened to allow the introduction of 4% hydrogen by volume in argon. Once the current passing through the sensor stabilized, hydrogen gas was cut off at the flow regulator for sufficient time to allow the hydrogen to desorb and this was repeated. The temperature inside the apparatus was maintained at 18°C.

2.5 Procedures and Techniques for CHAPTER 7

2.5.1 Preparation of Pd Salt-Loaded GO Aerogels.

GO was prepared by modified Hummers method starting from graphite powder [8], Briefly, graphite was oxidized using concentrated H_2SO_4 and $KMnO_4$ and the resulting GO was purified and isolated via successive centrifugation and dispersion cycles in water, then dried under vacuum. A 100 mM stock solution of ligated palladium ions was prepared by slowly adding 0.002 moles of palladium chloride ($PdCl_2$) into 20mL of a 100 mM ethylenediaminetetraacetic acid (EDTA) solution while stirring. This mixture was refluxed for 30 minutes to achieve dissolution and to degas the solvent, and was then used immediately after cooling to room temperature. After appropriate dilution of the metal ligand complex to the desired concentration with a total volume of 500 µL, 500 µL of a freshly sonicated (30 minutes Branson S-450D horn sonicator at 10% amplitude) 20 g/L suspension of GO was added and thoroughly mixed in a 1 cm x 1 cm plastic cuvette. Parafilm was used to seal the bottom, to better facilitate freezing. Each solution was then placed onto a block of dry ice and allowed to freeze fully (~20 minutes) before lyophilization. Lyophilization was carried out using a Labcono freeze drying chamber at 20 µbarr with the collector set at -52 °C.

2.5.2 Synthesis of Pd Nanoparticle Decorated GA.

The freshly lyophilized light brown GO aerogels were first reduced using hydrazine hydrate. Samples were placed under flowing nitrogen environment for 1 hour, then the nitrogen flow was passed through a solution of hydrazine monohydrate to provide an atmosphere saturated with hydrazine vapor. After 0.5 hours at room temperature, the vessel was heated in an oil bath at 30°C/hr to 90°C and held at this temperature for 1 hour. The hydrazine vapor was purged with pure nitrogen gas while the system cooled to room temperature. To further reduce the GO and Pd ions, the samples were placed in a furnace under the flow of hydrogen gas and were first heated to 400 °C for 60 min for the formation of GA and further heated to 900 °C for 10 min for the formation of Pd nanoparticles.

2.5.3 Fabrication of electrodes and ASCs.

An anode was prepared by placing the P-GA (pre-cut and pressed into small slices) onto a nickel substrate with silver paste (SPI 05001-AB) in between in order to form ohmic contact. A cathode was prepared by anodic electrodepositing MnO_2 onto a nickel substrate at a constant current of 0.5 mA cm^{-2}. The electrolyte for the deposition was prepared by dissolving 0.01M manganese acetate ($MnAc_2$) and 0.02 M ammonium acetate (NH_4Ac) in a solvent mixture of 90% DI water and 10% dimethyl sulfoxide (DMSO). The ASCs were assembled by sandwiching the cathode and anode with a separator (Celgard 3501, NC) in between. A 0.1 M sodium sulfate (Na_2SO_4) solution was employed as the electrolyte.

2.5.4 Materials characterization and electrochemical measurement.

Morphologies were characterized using scanning electron microscopy (SEM, ZEISS ULTRA 55). Chemical compositions were analyzed by X-ray photoelectron spectroscopy (XPS, PHI 5400). Cyclic voltammetry (CV), galvanostatic charge-discharge (GCD) and electrochemical impedance spectroscopy (EIS) measurements were performed on an electrochemical workstation (Bio-Logic, SP-150). EIS measurements were performed by applying an AC voltage with 5 mV amplitude in a frequency range from 10 mHz to 100 kHz. To study the electrochemical properties of individual electrodes (half-cell test), a three-electrode configuration including a working electrode, a platinum counter electrode and a saturated calomel electrode (SCE) reference electrode was used. For the ASCs (full-cell) test, a two-electrode configuration was directly connected to the cathode and anode of an ASC.

2.5.5 Charge Balance Adjustment:

As for a supercapacitor, the charge balance will follow the relationship q+ = q-, where q+ means the charges stored at the cathode and q- means the charges stored at the anode.[9] The stored charges (q) can be calculated using the following the Equation:[10]

$$q = C \times \Delta \mathrm{U} \times \mathrm{m}$$

where C is the specific capacitance of electrode, ΔU is the operation voltage window, and m is the mass of electrode materials. In order to keep the charges balanced, loading mass of active material from cathode and anode should be adjusted and kept at a constant ratio (k) using the following Equation:[10]

$$k = \frac{m_+}{m_-} = \frac{C_- \times \Delta U_-}{C_+ \times \Delta U_+}$$

On the basis of the specific capacitance values and operation voltage windows of each electrodes, the optimal mass ratio k between cathode and anode is about $m_{(MnO_2)}/m_{(P\text{-}GA)} = 0.53$.

CHAPTER 3. GRAPHENE/POLY(3-HEXYLTHIOPHENE) COMPOSITES

3.1 Introduction

Harvesting sunlight in large amounts would provide abundant eco-friendly energy and is currently a subject of much debate and research. Even with the advantage of an in-place infrastructure developed for computer component manufacture, inorganic photovoltaic devices are not presently effective enough to compete with hydrocarbon combustion as an energy source. The cost of producing these solar cells simply outweighs the energy produced over their relatively long life-times. Alternatively, polymer-based solar cells (PSCs) are much cheaper to manufacture, they can be produced by roll-to-roll techniques in large quantities, can be fabricated onto flexible substrates and have the advantage of being processed through solution. Unfortunately, PSCs suffer from lower power conversion efficiency and poorer environmental stability, though they are commercially produced for niche markets.

A primary limitation to PSC power conversion efficiency is the low distance over which excitons travel before undergoing recombination (~3-10 nm). This means that for a planar bilayer heterojuntion PSC, the only light-harvesting portion is a small volume at the interface between the electron donor and accepter in the active layer. To increase the interfacial portion of the active layer, both the donor and accepter are spin-cast onto an electrode from a common solvent. The two materials separate due to their differing solubility in the drying solution. This produces a much larger interfacial region as the materials are thoroughly integrated, and is called a bulk heterojunction solar cell (BHSC). Reproducibility of these PSCs is low because control over the morphology is difficult to obtain by this method. One solution to this problem is to impose order upon the active layer to optimize performance. These devices, called ordered heterojunction solar cells (OHSCs) are typically made by expensive top-down, multi-step procedures. The progression of solar cell types, by order is shown in Figure 5.

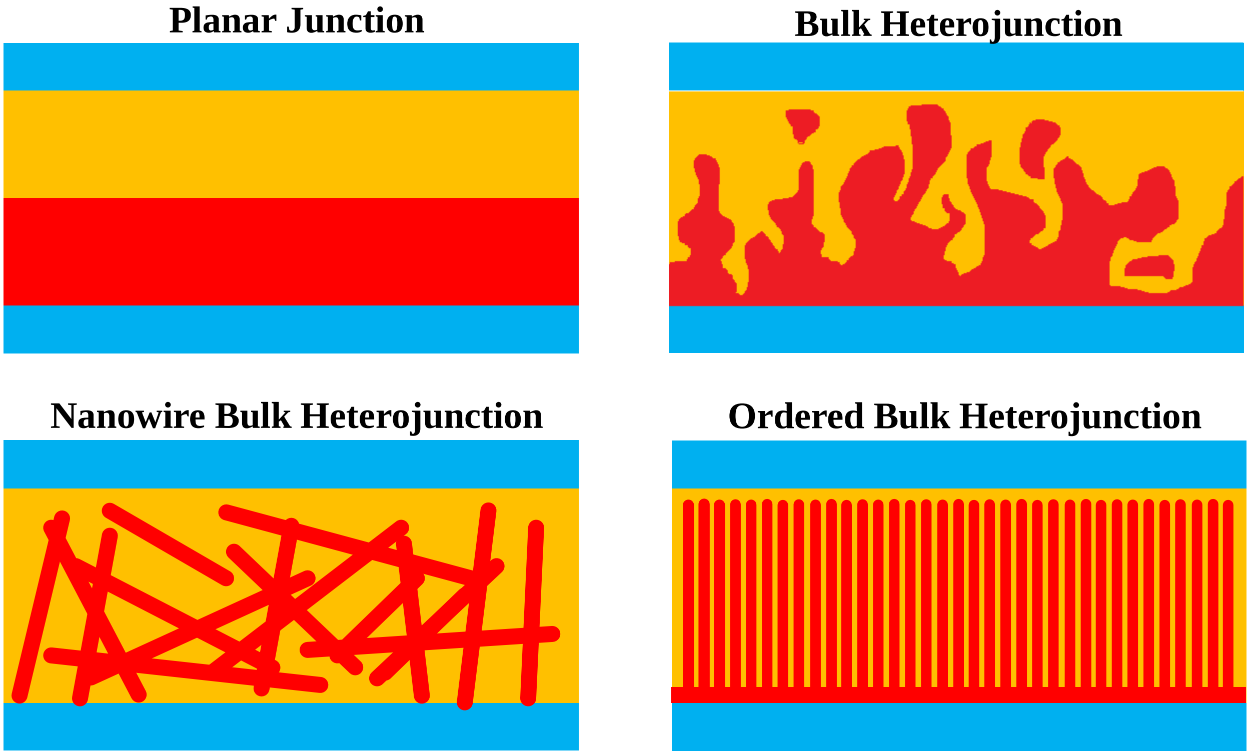
Planar Junction

Bulk Heterojunction

Nanowire Bulk Heterojunction

Ordered Bulk Heterojunction

Figure 5. Representation of different ordering and orientation of P3HT (red) and an n-type material (yellow) in organic solar cells.

The π-conjugated backbone of poly(3-hexylthiophene) (P3HT) – a common p-type material for BHSCs – facilitates π-π intermolecular interaction allowing it to crystallize into one-dimensional fibril-like crystalline domains as the fundamental structure in complex polycrystalline films. It has been shown that the performance of P3HT-based BHSCs is dependent on this morphology. Previously, our group has used carbon nanotubes (CNTs) to induce the crystallization of P3HT to generate centipede-like supramolecular structures on CNTs. This methodology offers a non-invasive bottom-up approach to construct intriguing CNT/nanowire (NW) hierarchical supramolecular structures.

Recently our group has used our experience with controlled conjugated polymer crystallization from CNTs and graphene oxide to assemble P3HT NWs on graphene platelets (GPs) and large area few-layer graphene (FLG). The dimensions of the wires are about 15 nm wide and up to several um long. This width is optimal for PSC performance, as it is approximately twice the exciton diffusion length. Also, the long dimension of the P3HT wires is π-stacked, so the charge mobility of each wire is optimal. P3HT adsorbs onto graphene to provide a flat, ordered growth front for NWs formation. These NWs could increase the efficiency of PCS and eliminate the need for problematic spin-casting/annealing procedures if it is possible to controllably grow wires from the surface of graphene and fill the gaps between the wires with an n-type material like fullerenes. This study mainly focuses on the formation and characterization of P3HT nanowires grown from the surface of graphene for the ultimate purpose of OHSC fabrication.

3.2 Results and Discussion

It was expected that because both CNTs and FLG have the same surface composition, P3HT would crystallize from the surface uniaxially because the graphene surface directs the P3HT to adsorb on the π face. This would lead to two interesting possibilities: an ordered 3D crystal, or a forest-like arrangement of NWs. To confirm the plausibility of P3HT growth directed by graphene, GPs were exfoliated in a chloroform solution of P3HT using a horn sonicator and these were added to a hot solution of P3HT in the marginal solvent anisole. The solution was then cooled slowly to allow for NW formation. Ordered growth of NWs from a suspended platelet of few layered graphene is evidenced the TEM image in Figure 6. Although, there were free wires on the TEM grid as well, P3HT clearly forms wires directed from each side of the GP.

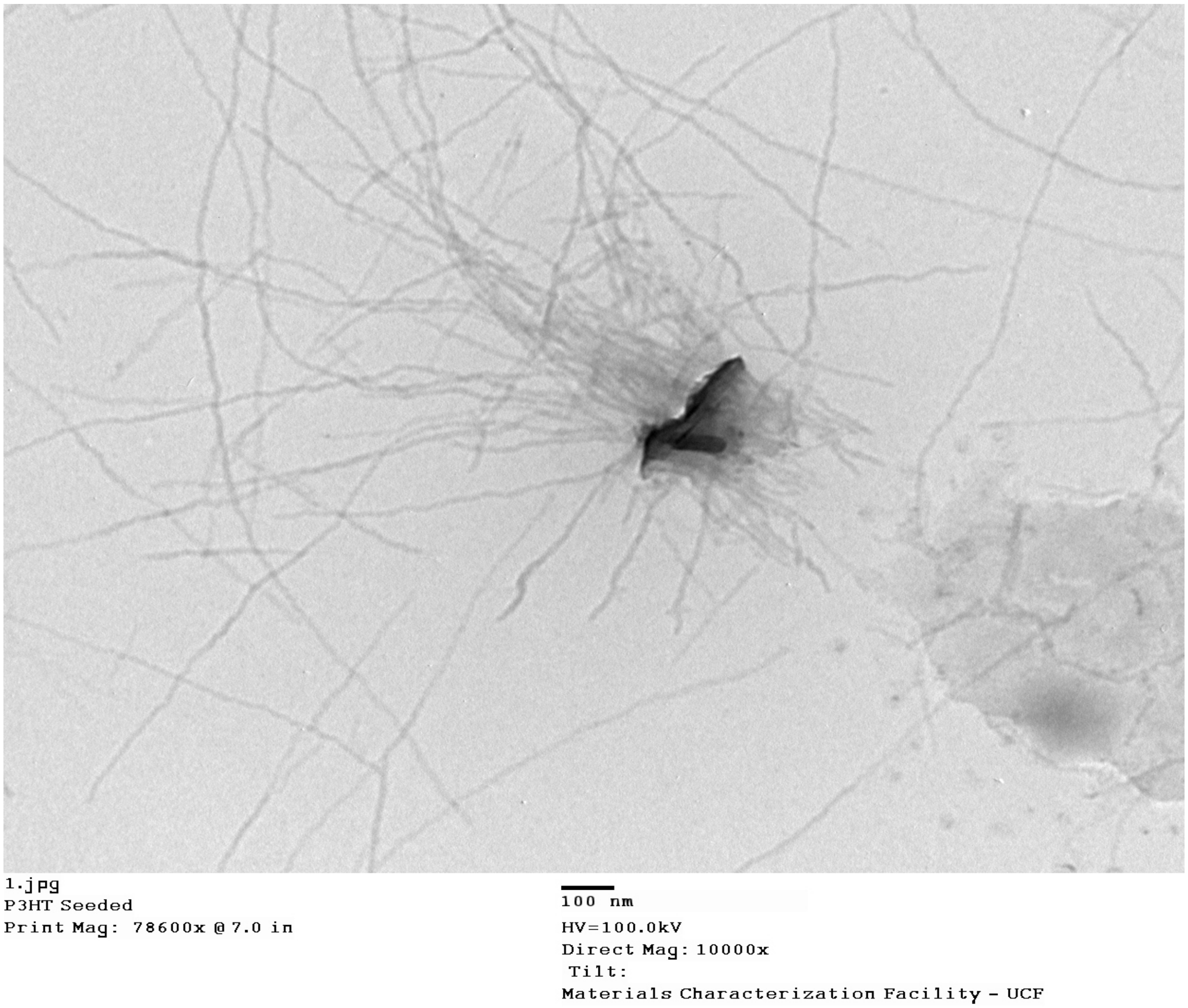

Figure 6. TEM image of P3HT nanowires that have grown from the surface of a graphene platelet.

For the NWs to be a viable material for OHSC devices, the height of the NWs should be controlled. Understanding the crystallization kinetics of this process would help facilitate such control. Attempts to monitor the crystallization of P3HT onto GPs by UV-Vis spectroscopy proved inconclusive. In previous studies, P3HT nanowire formations on CNTs were monitored by the absorbance of 600 nm light, characteristic of solid state P3HT. When the solution cooled, the absorbance at 600 nm increased due to P3HT nanowire formation on the CNTs. The challenges met were that with GPs, the absorbance at this wavelength went up and then down, evidencing an unlikely decrease in NW concentration in solution. This makes sense when coupled with observation of precipitation of the GP-P3HT composite. This process is additionally complicated by the presence of any free P3HT nanowires suspended in solution, which would be taken as wires on the graphene surfaces. To solve this problem, QCM – a technique widely used to investigate film growth for polymers or metals – was employed. To date, this is the first use of QCM to monitor polymer crystallization onto chemical vapor deposited (CVD) graphene.

3.2.1 Transfer and Characterization of FLG

In order to monitor polymer growth using QCM, a resonator must be constructed with a graphene film deposited on the surface of a quartz crystal. FLG was catalytically grown on a copper foil and characterized by Raman spectroscopy. The D and G bands are clearly seen in Figure 7 (a), and the relative heights and positions indicate that the graphene is 1-2 layers (depending on location of analysis), as the G peak at 1585 cm^{-1} is comparable in intensity with the 2D peak at about 2705 cm^{-1}.

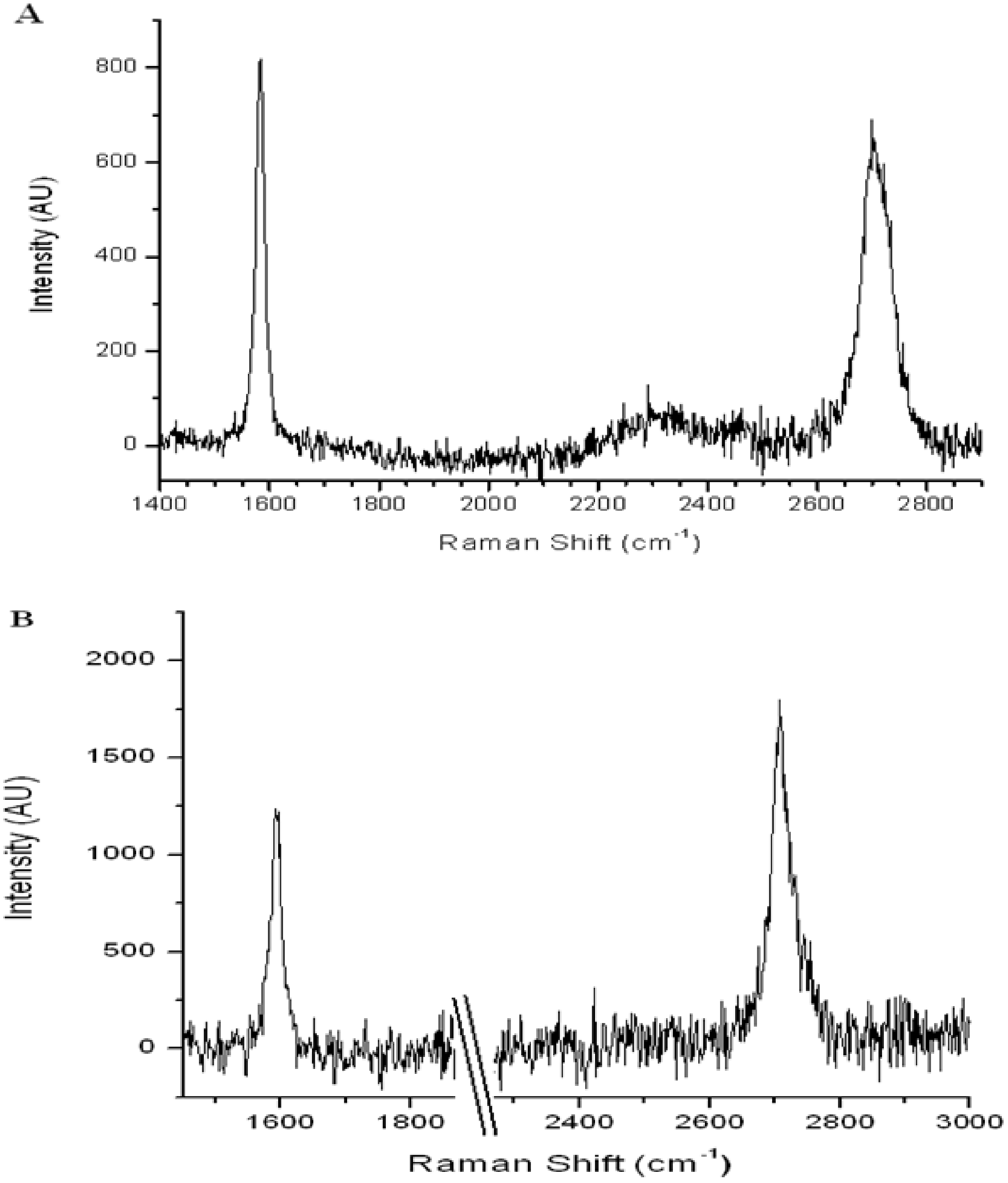

Figure 7. (a) Raman shift of 1-2 layers of graphene on copper. The peak at 1585 cm^{-1} and 2705 cm^{-1} are the G and 2D peaks, respectively. (b) Raman spectrum of graphene transferred to glass. The portion analyzed in A is likely 2 layers, and in B 1 layer. A portion of the Raman spectrum containing only one narrow, intense peak attributed to ambient light was removed for clarity.

Poly(methyl methacrylate) (PMMA) was spin coated onto one side and the foil was floated, copper side down, onto an etchant solution of $FeCl_3$ until fully dissolved. The FLG/PMMA was then lifted out onto a QCM crystal over the gold layer, rinsed with distilled water and the PMMA was washed away with acetone. Although, several reports indicate that acetone washing usually leaves residual PMMA on the surface, that any residual PMMA is dissolved while heating in an anisole solution for the equilibration time (2-4 hr). Figure 7 (b) is a Raman spectrum showing the graphene transferred to glass, indicating that the transfer methodology is sound.

3.2.2 QCM Analysis

Both as-purchased QCM crystal (bearing a gold coating) and a QCM crystal bearing the transferred FLG were separately immersed into a hot anisole solution of P3HT and cooled slowly to room temperature while the mass change was monitored. Since sulfur-containing compounds are widely known to bind with gold, it was thought that a comparison of the relative mass changes of the unmodified and FLG-coated QCM crystals should provide insight into the relative affinity of P3HT for FLG and gold. When a hot P3HT solution was cooled from 80˚C to 55˚C over an hour, the mass change fluctuated somewhat. This was found to be the characteristic response of the QCM crystal to temperature changes over this range. This was verified by cooling a solution of pure anisole on an unmodified QCM crystal, which showed the same response.

While monitoring the mass change, the bare QCM crystal was immersed in hot P3HT solution and cooled to 55˚C then held for 4 hours. At that point, the solution was allowed to cool to room temperature, while an immediate increase in mass change was observed, which began to taper off after 20 minutes. After 4 hours, the mass change stopped increasing, giving a total mass change of about 30 μg/cm^2 (Figure 8) and a purplish film of P3HT was observed on the gold surface after removal. No film was observed on the quartz portion of the crystal, indicating that there is an affinity for P3HT adsorption on gold over quartz.

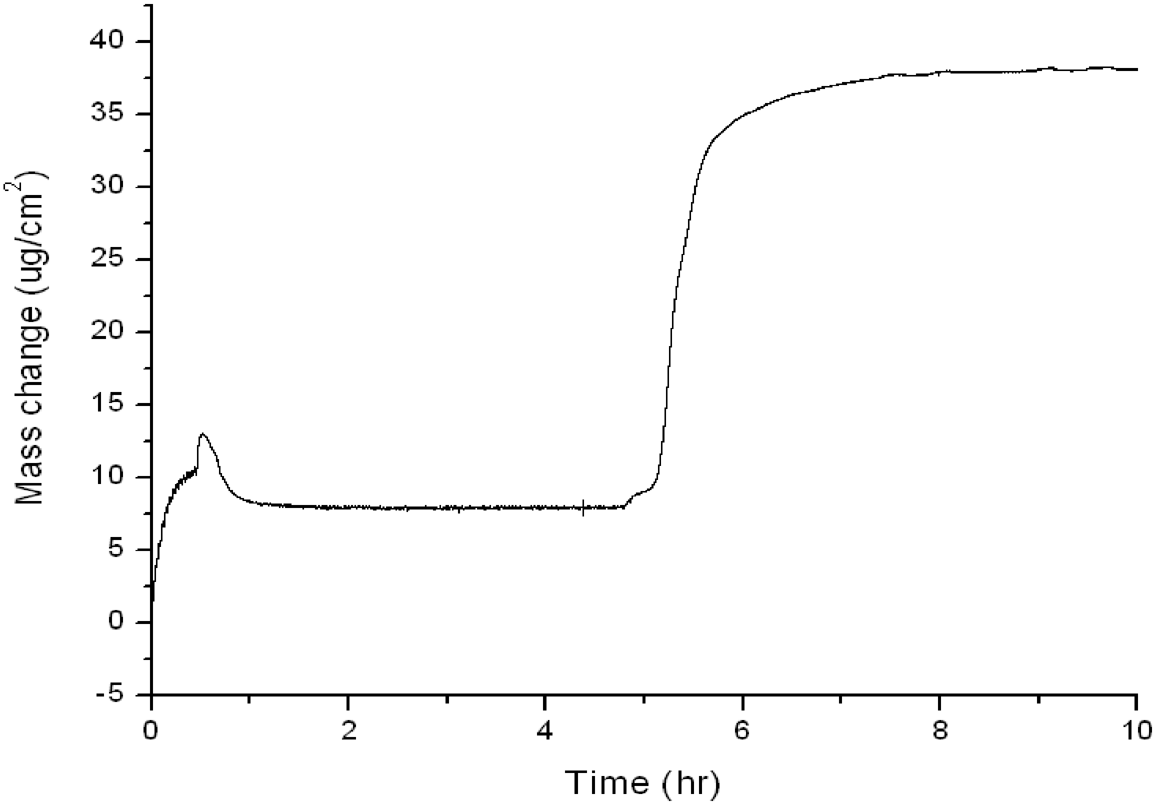

Figure 8. Graph of mass change of P3HT on gold obtained by QCM. The temperature was held at 55˚C until hour 5, then the source was turned off, allowing the solution to cool to room temperature.

After inspection of the graphene on the QCM stage, it was immersed into a hot anisole solution of P3HT and cooled slowly to room temperature while the mass change was monitored (Figure 9). Overlaid in the resulting graph are blue points which are temperatures recorded during analysis. At each of these points the temperature of the solution was recorded and the water bath was set to subsequent temperatures. The black curve is the corresponding mass change on the surface of the QCM crystal.

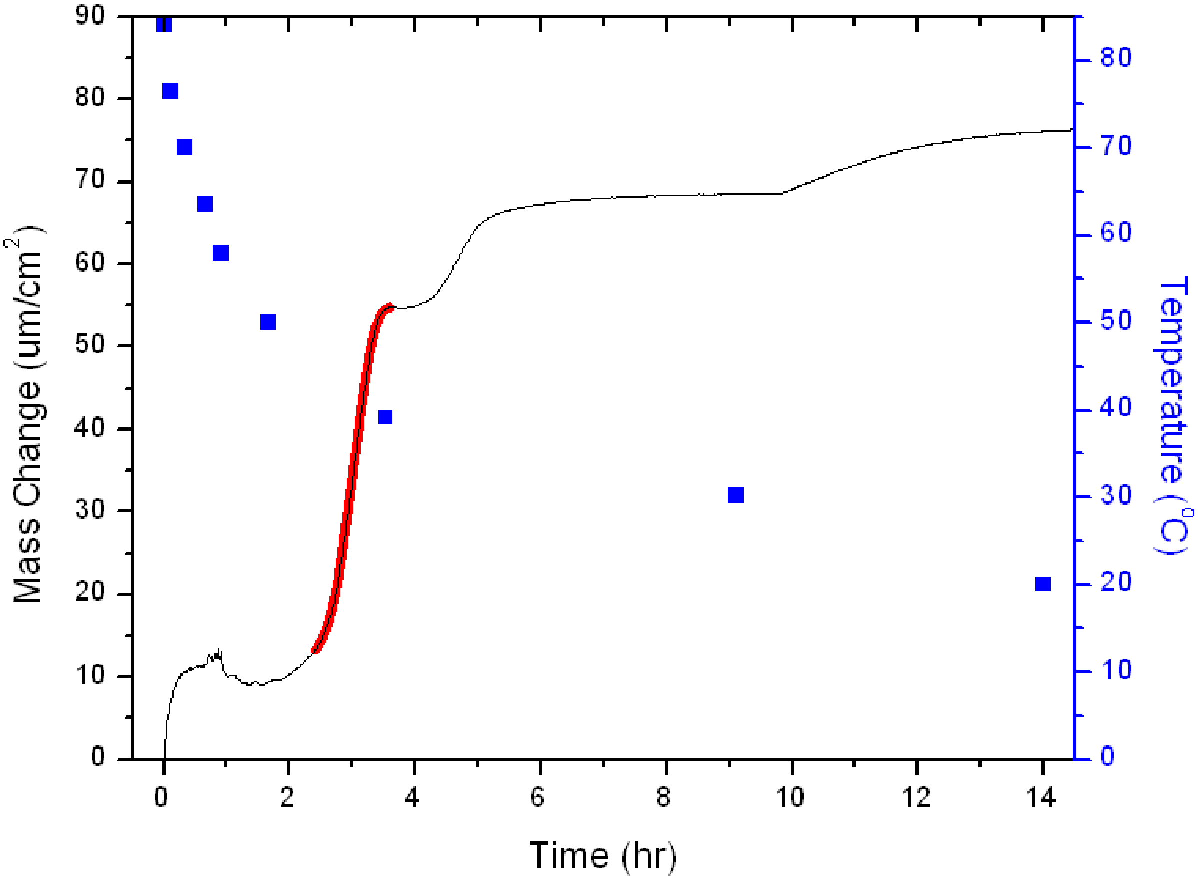

Figure 9. Graph of mass change of P3HT on graphene and the corresponding temperatures at which this mass change occurred obtained by QCM. The portion of the curve used in kinetic analysis is highlighted in red.

Some interesting features of the mass change behavior of P3HT crystallizing from graphene can be seen in the inflection points. Following each reduction in bath temperature there was a rapid increase in the mass followed an eventual decline in the slope to zero. The temperature change from 50˚C to 40˚C showed the largest mass change (47 µg/cm2) over about two hours. At this point the solution stayed transparent and yellow, indicating that the polymer did not precipitate in solution. The graphene coated portions of the QCM crystal did, however darken substantially from the adsorption of P3HT. After the mass reading became constant, the temperature was again reduced to 30 ° C which was followed by a less drastic mass change of 15 μg/cm^2 over a 5 hour period. During this period the solution became opaque and red, indicating crystallization of the polymer in solution. Lastly, when the solution allowed to cool to room temperature there was a final increase in mass by 8 μg/cm^2 over 4 hours which then remained stable for the next 6 hours giving a total mass change of 75 μg/cm^2. From the two graphs, it seems that the selectivity for P3HT adsorption onto graphene over gold is about a factor of two. Another comparison between the two surfaces that shows how P3HT preferentially deposited onto the graphene covered regions of the same QCM crystal rather than the exposed gold surface during the former experiment. The selectivity is readily seen upon visual inspection of the resulting QCM crystal shown in Figure 10.

Figure 10. Image of the P3HT grown onto graphene deposited onto the QCM stage. Note the cracks in the graphene during transfer are clearly evident, as P3HT has deposited quite selectively onto the graphene portion.

3.2.3 Calculations Utilizing Avrami Equation

Each mass change brought on by cooling has quasi-sinusoidal shape which is characteristic of polymer crystallization. This can be subdivided into three portions: nucleation, growth, and depletion for the increasing, constant and reducing rates of crystallization. Avrami exponent is a widely used mathematical tool to elucidate crystallization processes and has been used in the study of P3HT crystallization. To better understand the kinetics of the crystallization process the Avrami equation was applied to the isothermal crystallization portion of the curve highlighted in red in Figure 9. The red portion of the curve was chosen because it is late enough after temperature change to ensure that the process is isothermal. Additionally this portion is not complicated by the crystallization of polymer in solution. The Avrami equation is

$$\lambda(t) = \exp\{-kt^n\}$$

Here $\lambda(t)$ is the fraction of untransformed material at time t, k is a constant that depends on the geometry and growth rate, and n is the Avrami exponent which is indicative of nucleation and growth acts. A more functional version of the Avrami equation for our purposes is

$$\ln \ln (1/\lambda(t)) = \ln k + n \ln t$$

A plot of ln ln λ*(t)* vs. ln *t* will produce a slope of *n* as seen in Figure 11.

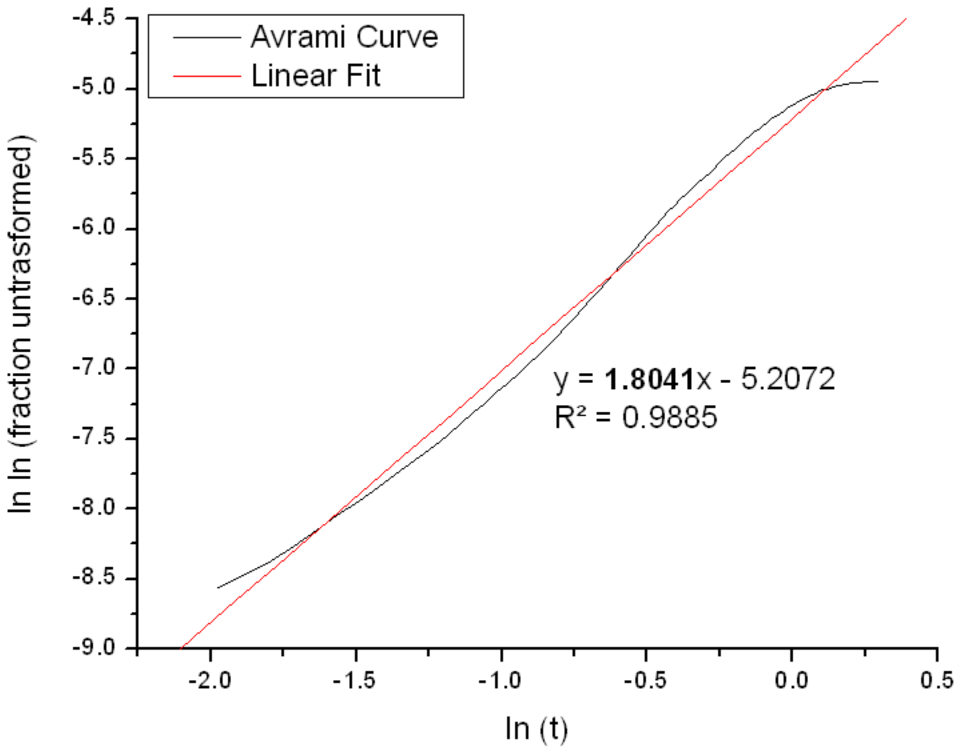

Figure 11. Graph of ln ln λ*(t)* vs. ln *t* with a best fit line. Bolded is the Avrami exponent in the linear fit equation.

The slope of this curve is 1.8, which is similar to Avrami exponents experimentally determined by crystallization of P3HT from the melt (~1.3). Values of *n* between 1 and 2 are indicative three things: that nucleation is heterogeneous, growth is linear and most importantly that crystal growth is one-dimensional. Heterogeneous nucleation means that the P3HT is most likely nucleated at the graphene surface and growing from that surface. This is supported by observation of the darkening of the graphene film and not of the solution. Linear growth is supported by observation of a linear regime in the growth stage of crystallization from 50 °C to

40 ° C. These data combined with the following electron microscopic study support our claim that NWs are growing from the graphene surface.

Probably the most exciting feature of the QCM study is that the amount of mass deposited has dependence on the crystallization temperature, reaching a maximum value. Because the wire height is dependent on the solution temperature, controlling this parameter could be as easy as removing a film from solution at a temperature corresponding to the desired height.

3.2.4 Electron Microscopy

In order to determine if the surface of the graphene is indeed covered with wires, transmission electron microscopy (TEM) and scanning electron microscopy (SEM) analysis was performed. Because the P3HT film on graphene proved to be so thick as to be opaque under TEM, a TEM image of P3HT nanowires grown in the solution which the QCM analysis was carried out is shown in Figure 12. As with the study of P3HT-GP composites, P3HT wires clearly formed in this solution.

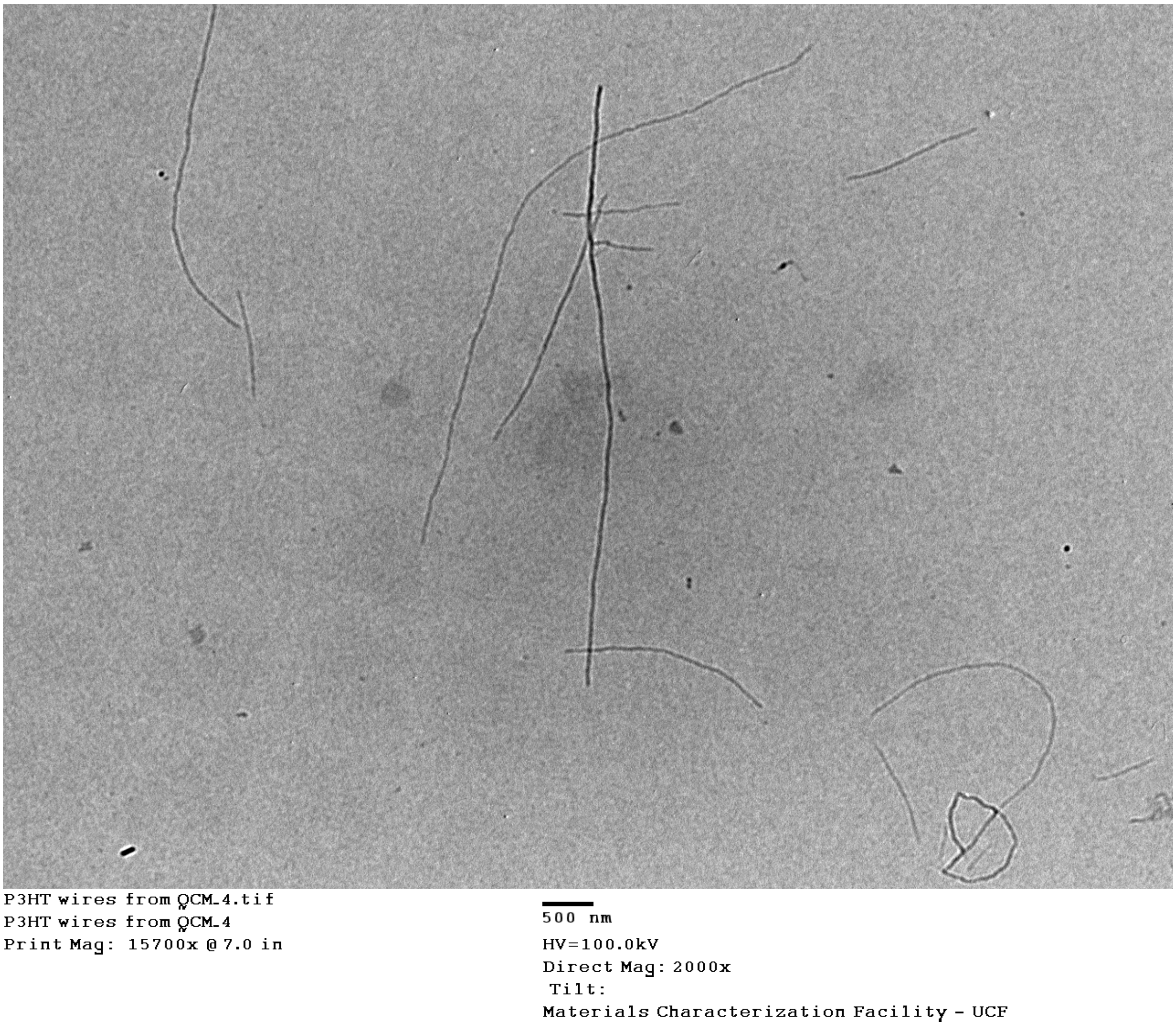

Figure 12. TEM image of P3HT nanowires deposited onto a TEM grid from the solution after QCM analysis of P3HT crystallization onto graphene was performed.

To characterize the surface morphology of the P3HT, SEM was carried out. The resulting image (Figure 13) is somewhat blurred because of charging of the semi-conducting rather than conducting material, but anisotropy is clearly evident. This periodic and directional structure implies that the P3HT is indeed crystalline and is in the form of NWs. It should be noted that higher resolution images can be taken if the material is first coated with a metal, but in this study the NW dimension is of critical importance. The width of each wire was determined to be ~15 nm which is in agreement with P3HT NWs formed form CNT surfaces. Possibly the clearest indicator that the wires grew from the surface rather than were deposited onto graphene is that the wires are unidirectional. P3HT NWs deposited onto TEM grids, or spin cast display a more random orientation than what is observed here. This uniform arrangement can be explain by unidirectional growth perpendicular to the graphene, and then they likely bend during the removal and drying process after QCM analysis. The unidirectional orientation of P3HT could have further reaching effects than for PSCs, as the morphological anisotropy will invariably lead to anisotropic electrical properties, which would be useful in field effect transistors and sensors.

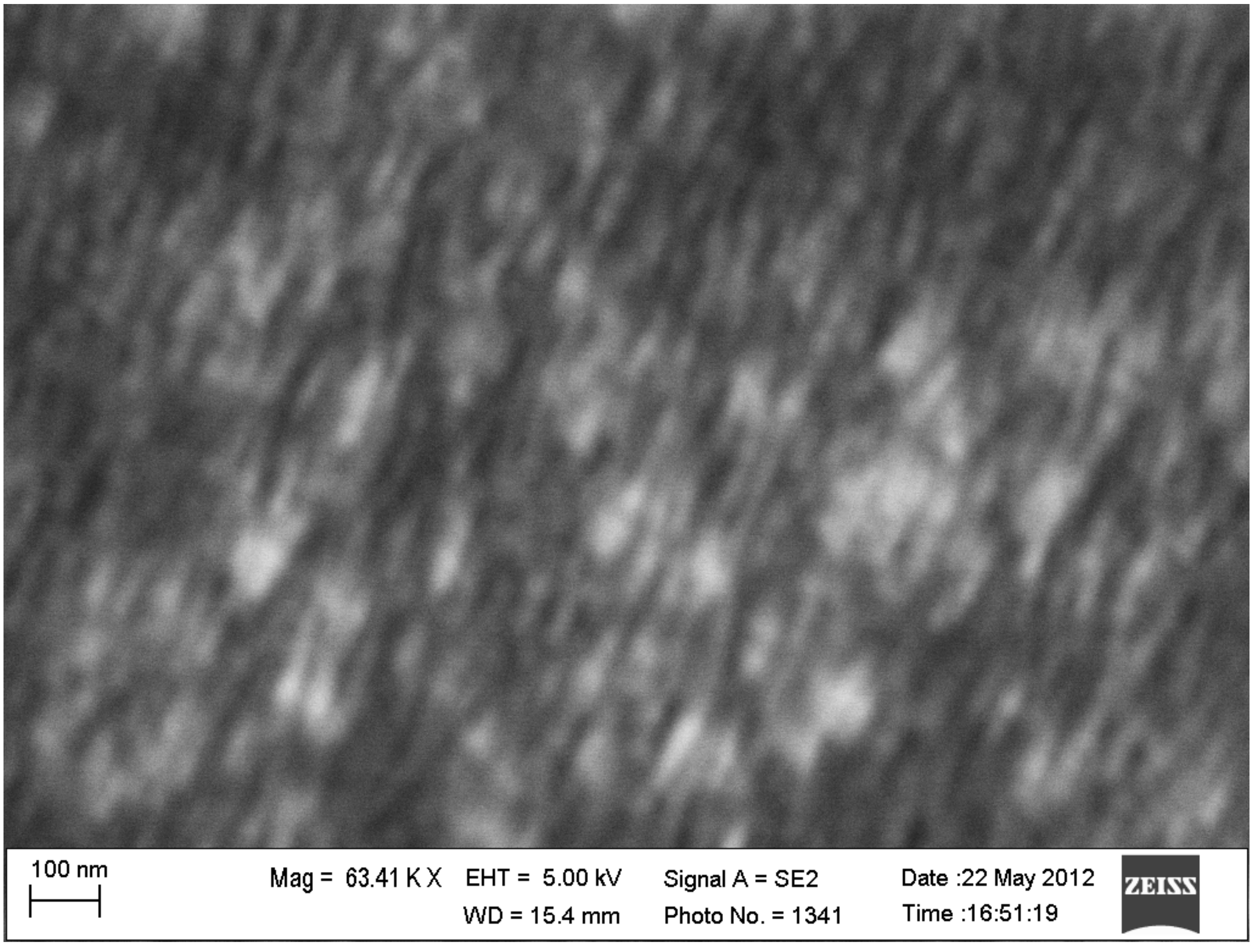

Figure 13. SEM image of P3HT grown from graphene during the QCM analysis.

3.3 Conclusion

Graphene was observed to drastically effect the crystallization of P3HT from a marginal solvent, such that P3HT will selectively stick to graphene, and grow NWs from the surface at temperatures above the normal crystallization temperature of P3HT in anisole. This study indicates that graphene directs the growth of P3HT to form NWs from the surface in a forest-like arrangement. QCM has proven to be a power tool in facilitating understanding of a complex system. This preliminary study of graphene/P3HT composites showed that controlled P3HT NW growth and the directed orientation of P3HT NWs is an interesting system which is capable of application in OHSCs and possibly other organic electronic devices.

The techniques necessary to produce organized graphene/P3HT composites with control over wire density and/or height requires further study. Firstly, as some PMMA residue may be left behind after the washing process, the effect of a pyrolysis step to remove the PMMA may be interesting to eliminate the possibility of contamination. By reducing the concentration of P3HT in solution and observing changes in the crystallization rate, more kinetic data can be obtained to produce better control of film thickness. Once this has been done, and some higher quality SEM images obtained, incorporating fullerene derivative into the material to determine how well it will integrate between and adsorb to the P3HT NWs can be done. In the proposed OHSCs, graphene would function dually as a template to grow uniaxial NWs, as well as a window electrode, as it is highly conductive and transparent. Improvement of the transfer process is ongoing, and graphene films without such cracking as seen in Figure 5 are now possible.

This technology of wire formation leads to several different avenues, as the polymer identity can be changed for tuned device performance, as P3HT is not the only polymer which can form NWs. Further, as stability is an issue with these wires, cross-linking of the P3HT in the wires, will be explored. It was shown that NWs can be used as a temple to form alternative one dimensional materials via the use of co-polymers which can be made with diverse functionalities. The advantage of P3HT copolymers is that they can crystallize from CNTs (so likely graphene as well), with functionality extending over the whole wire. This opens the potential for producing hybrid composites of graphene surfaces with additional materials extending from the surface, held in place by the NWs or holding NWs in place.

Another method of producing graphene films is by electro-deposition of reduced graphene oxide from graphene oxide. Recent literature suggests that this is possible, and depending on the extent of the reduction the graphitic portions may be extensive. It may be possible they reduced graphene oxide may be a more facile way to accomplish the same templating seen in this study without the need for CVD or transfer.

CHAPTER 4. ORGANIC FIELD-EFFECT TRANSISTORS USING DIRECTLY CRYSTALLIZED P3HT ON RGO ELECTRODES

4.1 Introduction

Semiconducting conjugated polymers have attracted an enormous interest for use in organic field-effect transistors (OFETs) due to its flexibility, transparency, easy processing, low-cost, low-weight, and large-area coverage.[11] OFETs can be considered as fundamental building blocks for integrated circuits in organic electronics. In order to achieve high performance in OFETs, controlling the quality of organic semiconductor and the degree of crystallinity is essential. It has been shown that the morphology of conjugated polymer is extremely sensitive to the processing parameters such as molecular weights, deposition methods, solvent types, and substrate treatments.[12] For example, typical mobility of poly (3-hexylthiophene) (P3HT) can vary by several orders of magnitude depending on these processing parameters. Therefore, designing a molecular structure of organic semiconductor is highly demanded for making high-performance OFETs.

Reduced graphene oxide (RGO) has been introduced due to its solubility, relatively low-cost, moderate production volume, easy-processing, and its chemical functionality.[13] Our previous work has shown that RGO can be also used as graphitic domains to fabricate RGO-induced supramolecular two-dimensional (2D) P3HT crystalline nanowire structure.[14] This unique preferential supramolecular 2D structure is in special interest because one-dimensional (1D) electronic properties of its π-conjugated polymer chains are modified by the increased interchain stacking that results from their π-π interactions.[15] Thus, it will be of great importance to investigate the electrical performance of OFET devices using such crystalline nanowires. In addition, RGO has been reported as a promising candidate electrode material for OFETs as counterpart of metal electrodes due to lower injection barrier from strong π-π interaction at graphene/organic interface[16], it is also interesting to explore the electrical properties of OFETs using rGO electrodes with crystalline P3HT nanowires.

In this work, the performance of OFETs using direct growth of P3HT crystalline nanowires on solution-processed RGO electrodes is demonstrated. RGO was also used as source and drain electrodes in OFETs. Interestingly, improved performance of P3HT nanowire OFET devices using RGO electrodes when compared to conventional metal electrodes was found. Electronic transport measurements on OFET devices indicated that, compared to metal electrodes, RGO electrodes can have a better device performance, in terms of on-current, mobility, and the current on-off ratio, and this improvements can be attributed to better morphology of P3HT due to one-dimensional crystalline nanowire structure with RGO domains as well as the favorable π-π interaction at RGO electrodes and the crystalline P3HT nanowires interface.

4.2 Results and Discussion

The schematic of fabrication steps of making RGO electrodes is described in Figure 14. AFM morphological investigation of RGO/P3HT devices (Figure 15(a)) show clearly defined P3HT nanowires extending between RGO electrodes. RGO/P3HT devices were then analyzed by Raman spectroscopy, displayed in Figure 15(b). The bare RGO electrodes showed two peaks at 1604 cm^{-1} (in-plane vibrational G band) and 1357 cm^{-1} (disordered vibrational D band), which are typical for RGO. The spectrum of an RGO/P3HT device shows the addition of two large new peaks at 1380 and 1448 cm^{-1} which are assigned to the C-C skeletal stretching and C=C ring stretching of P3HT, respectively. The D band of RGO and the C-C skeletal stretching peak of P3HT are superimposed in the composite in the 1300-1400 cm^{-1} range (indicating that the P3HT nanowires remain unaltered by RGO), while the G peak is slightly shifted to 1600cm^{-1}. Such a shift to low frequency shift in the G band of RGO has been found to be due to the effect of electron donors such as P3HT.[14] In this study, the shift (~4 cm^{-1}) is much less than previous studies (~15 cm^{-1}) because these RGO electrodes are many layers thick, so the signal is that of RGO overlaid with that of the RGO/P3HT interaction. These structures are stable after several washes with anisole at room temperature, whereas Pd electrodes prepared the same way did not have P3HT on the surface. A TEM image of P3HT wires crystallized from solution is shown in Figure 15(c). For comparison, Figure 16 shows the AFM morphology of P3HT nanowires on Pd electrodes after drop-casting of P3HT nanowires crystallized such a solution.

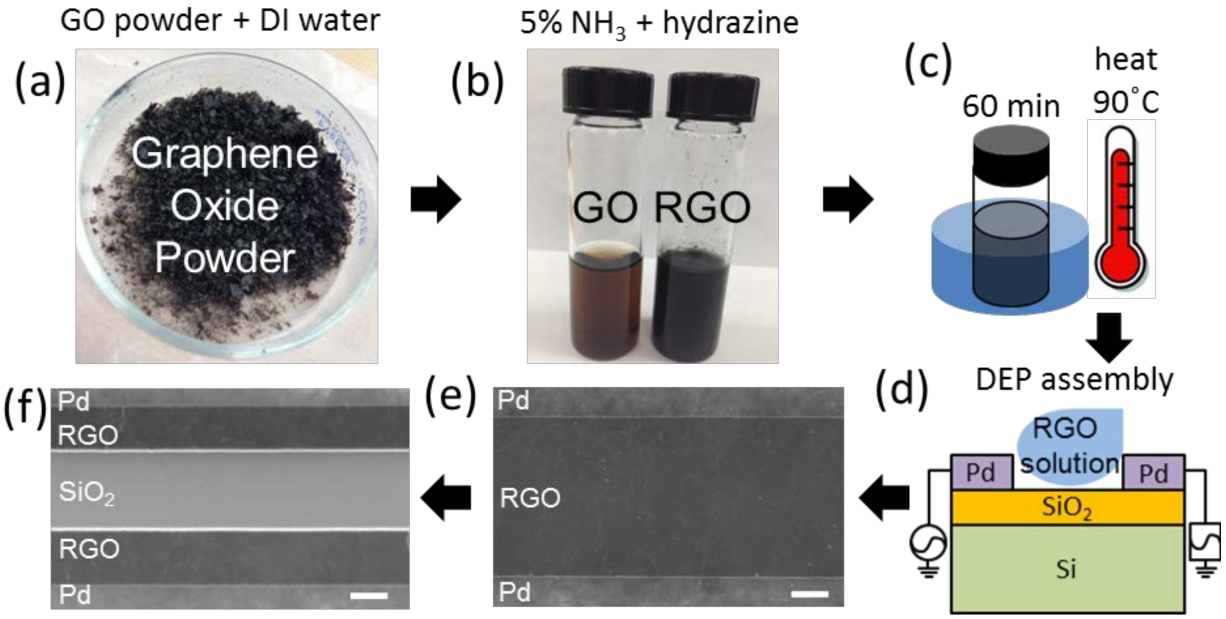

Figure 14. Schematic illustration of the preparation method of rGO electrodes. (a) Commercially available GO powder is diluted in deionized water. (b) Hydrazine solution is added to GO solution and (c) the solution is heated at 90˚C for 60 min in order to make chemically reduced-GO (RGO) solution. (d) RGO solution is

dropped and assembled via dielectrophoresis (DEP) method. SEM image of (e) RGO assembly and (f) RGO electrodes. (Scale bar : 1µm)

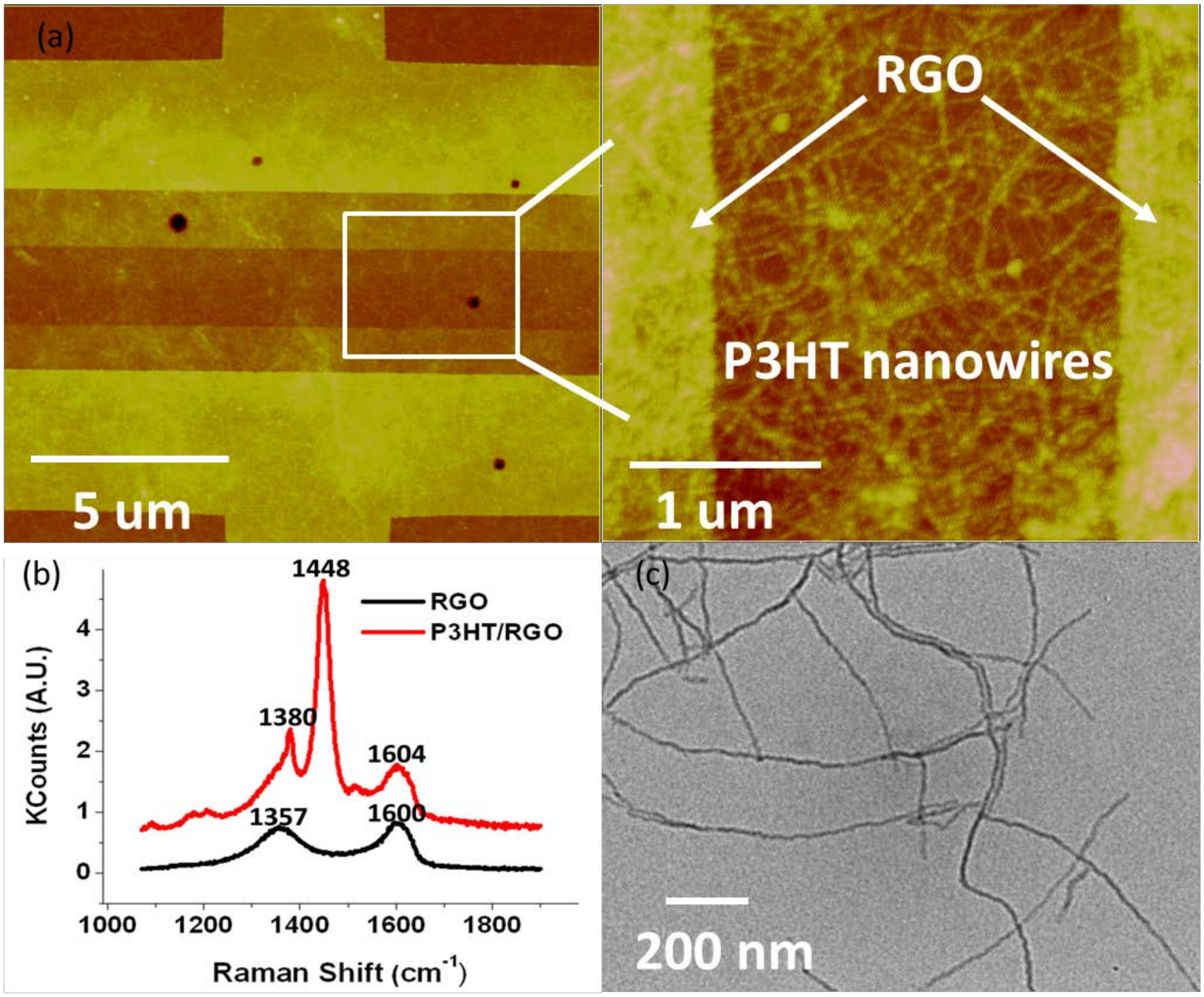

Figure 15. (a) AFM images of crystalline P3HT nanowires on RGO electrodes, with a close-up on the right (b) Raman spectra of RGO and P3HT-coated RGO electrodes in devices. (c) TEM image of P3HT nanowires.

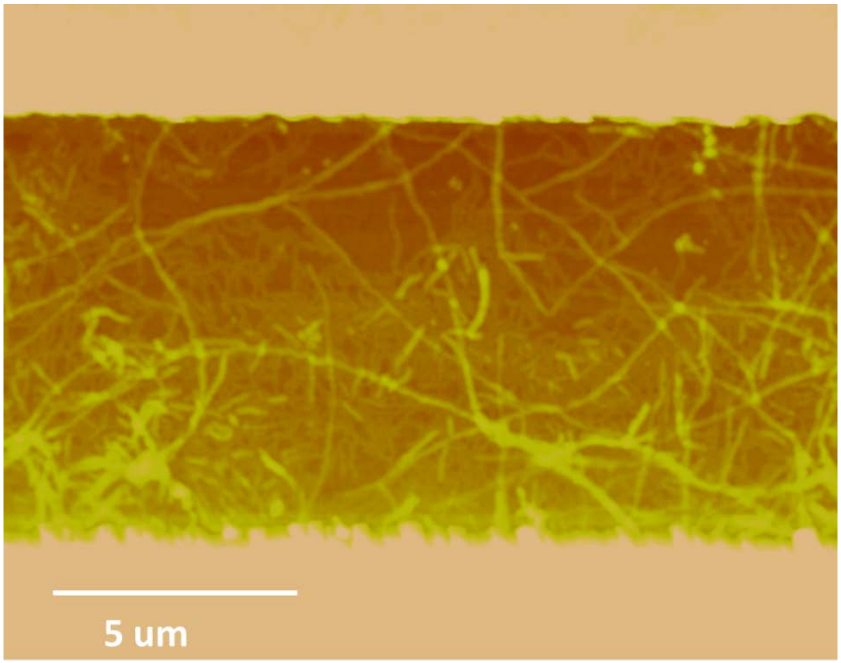

Figure 16. Atomic force microscopy (AFM) images of P3HT crystalline nanowire with control Pd electrodes.

Figure 17(a) and (b) show the drain current (I_d) vs. source-drain bias voltage (V_d) curves (output characteristics) at different gate-voltages (V_g) for our representative P3HT crystalline nanowire OFET devices with RGO electrodes and Pd electrodes. All the devices show a good gate modulation with linear behavior at low bias and saturation behavior at higher bias, thereby displaying typical p-channel OFETs behavior. For the comparison of device characteristics, we plotted all the curves in the same scale. From here, we observed that the output current (V_g = -20V, V_d = -100V) of RGO/P3HT and Pd/P3HT is 0.16 and 0.10 µA, respectively.

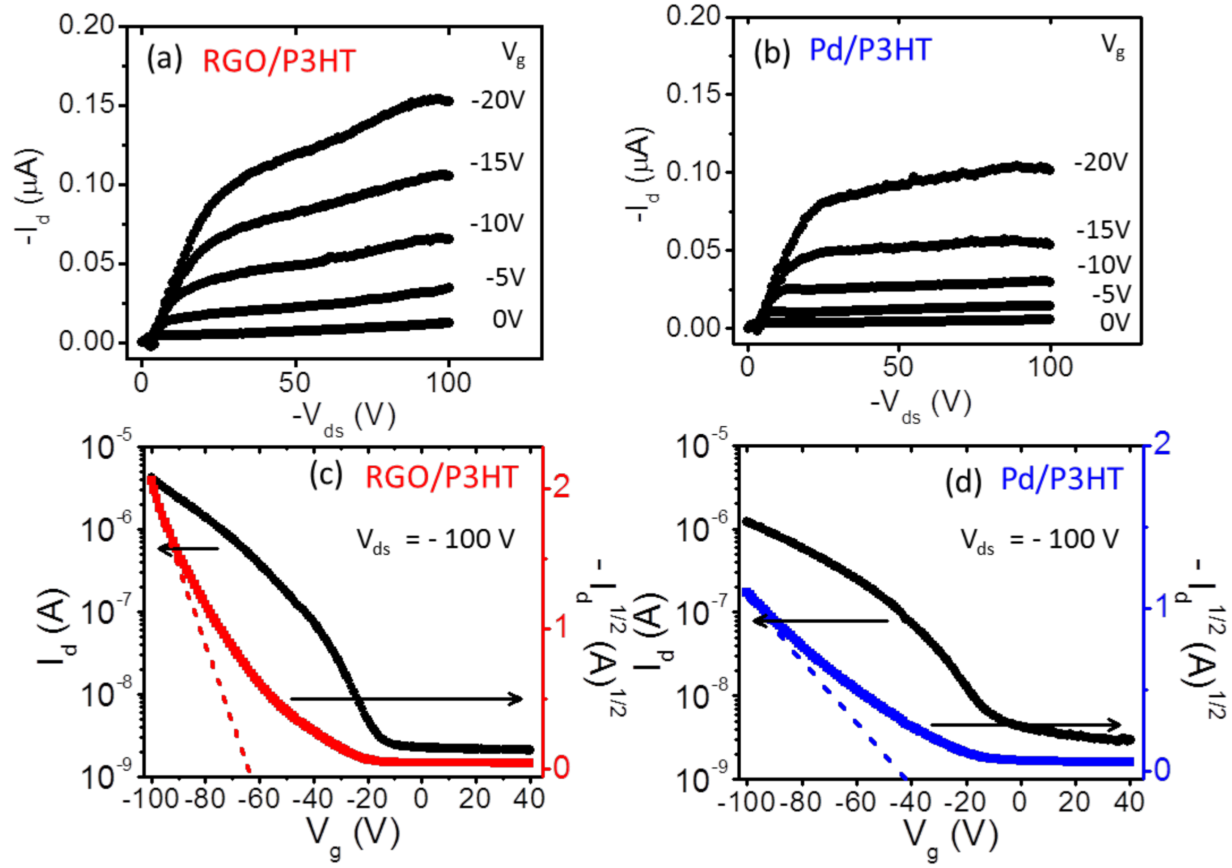

Figure 17. Output characteristics $(I_d$-$V_d)$ of P3HT nanowire FETs using (a) RGO electrodes and (b) Pd electrodes. Transfer characteristics $(I_d$-$V_g)$ at V_d = -100 V (left axis) and $(I_d)^{1/2}$ (right axis) of the devices with (c) RGO electrodes and (d) Pd electrodes.

For further investigation of the effect of electrodes on the device performance, we also measured the corresponding transfer curves (I_d *vs.* V_g) of the same devices at V_d = -100 V (Figure 17(c) and(d)) and extracted the field effect mobility (μ), on-off ratio (I_{on}/I_{off}) and on-current (I_{on}) of the devices. The mobility is calculated using the standard formula, $\mu = (2LI_{d,sat})/(WC_g(V_g-V_T)^2)$, where $I_{d,sat}$ is saturation current, C_g is gate capacitance, and V_T is threshold voltage, respectively; where $I_{d,sat}$ is saturation current, and C_i is the gate dielectric capacitance (13.8 nF/cm^2). The value of μ for RGO/P3HT is 0.49 cm^2/Vs, and for Pd/P3HT is 0.006 cm^2/Vs. The mobility of RGO/P3HT is 8 times higher than Pd/P3HT. In addition to μ, other important parameters such as current on-off ratio ($I_{on/off}$), and I_{on} are extracted to evaluate the performance of the OFETs. The transfer curves show that the $I_{on/off}$ and I_{on}/ (I_d at V_g =-40V) for RGO/P3HT are 2.43×10^3 and 4.46 μA, and for Pd/P3HT are 6.16×10^2 and 1.54 μA. Therefore, mobility, $I_{on/off}$, and I_{on} of RGO electrodes with P3HT crystalline nanowires are improved considerably when compared to Pd electrodes.

The device characteristics measured from 9 devices for RGO/P3HT, and Pd/P3HT are summarized in Figure 18, where we plot the Ion, μ, and Ion/Ioff. Figure 18 shows that, similar to our representative devices, the maximum (average) Ion is 4.73(3.78) μA for RGO/P3HT, whereas 2.51(1.77) for Pd/P3HT. Similar improvement found in maximum (average) μ and Ion/off showing 0.053(0.045) cm2/Vs and 2.46×103(2.43×103) for RGO/P3HT, while for Pd/P3HT they are 0.027(0.012) cm2/Vs and 1.08×103 (7.72×102), respectively. The increase in the average mobility for RGO/P3HT is three times higher compared to the devices without RGO in the electrode. From this study, it is clear that the different type of electrode, which controls the injection barrier as well as work function at the electrode/organic interface, plays a key role in determining the performance of OFETs. From the table (Table S1, supporting information), we can see that the mobility and current on-off ratio of our control P3HT devices are in agreement with the devices that have been reported in other literature. We also note that all of our devices didn’t use any substrate treatment in the fabrication process.

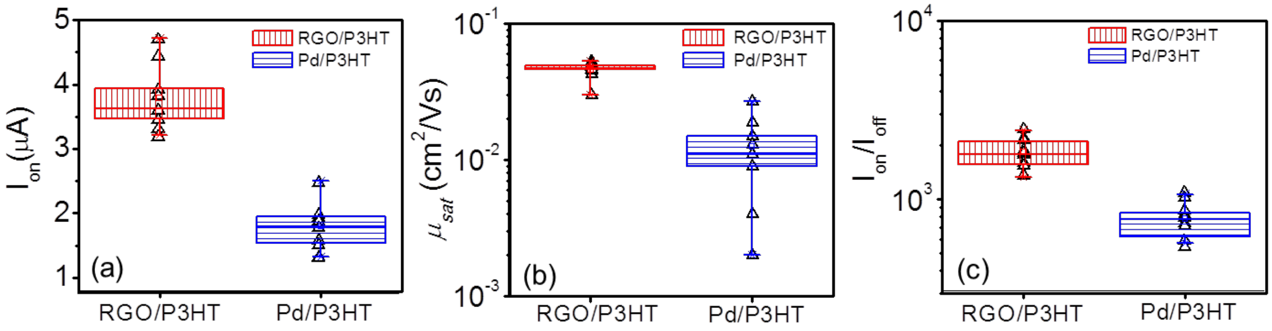

Figure 18. Summary of P3HT nanowire FET device performance from 18 devices. (a) On-current (I_{on}), (b) Saturation field-effect mobility (μ_{sat}), and (c) On/off ratio (I_{on}/I_{off}) for both RGO electrodes and Pd electrodes.

The improved device performance from RGO/P3HT OFET devices can be attributed to not only (i) the crystallinity of P3HT nanowire on RGO domains, but also (ii) small interfacial dipole formation at graphene/organic interface from favorable π-π interaction, leading to a small carrier injection barrier. It is believed that the better morphology formation of P3HT can be a significant impact to enhance the device performance due to its unique crystalline nanowire structures directly grown from RGO domains.[14] As seen in Figure 18(a), it is clear that RGO/P3HT devices can provide more output current than Pd/P3HT devise under the same applied voltages, which led to enhanced mobility and current on-off ratio.

In addition, the interface between graphene/organic has been reported as favorable interface compared to conventional metal electrodes. The current (I_d) at the interface at a fixed bias voltage and temperature (T) can be approximated as $I_d \propto exp(-\phi_B/kT)$, where ϕ_B is the Schottky barrier between the electrode/semiconductor interface and k is the Boltzmann constant. A decrease in ϕ_B will result in an increase of current at the interface. However, when Pd is contacted with P3HT nanowire, the effective work function of Pd is significantly reduced due to large dipole barrier at Pd/pentacene interface known as the ‘push back effect’, which resulted in reduced effective work function of Pd electrode, giving rise to a large Schottky barrier for hole injection at electrode/organic interface. In contrast, a strong π-π interaction exists at RGO/P3HT interface, therefore, significant dipole formation may not occur and the work function of RGO may not be modified significantly due to contact with the organic semiconductor, which keeps the barrier height lower.

4.3 Conclusions

In conclusion, we studied the performance of OFETs using directly growth of poly (3-hexylthiophene) (P3HT) crystalline nanowires on solution-processed reduced graphene oxide (RGO) electrodes. We found the device performance of OFETs using P3HT nanowires with RGO electrodes can be improved compared to conventional metal electrodes, mainly in terms of on-current, mobility, and the current on-off ratio. The performance improvements can be attributed to better morphology of P3HT due to one-dimensional crystalline nanowire structure with RGO domains as well as the favorable π-π interaction at RGO electrodes and the crystalline P3HT nanowires interface. Enabling to fabricate OFETs using crystalline nanowires directly grown from RGO domains can open up new areas in science with a host of applications in many next generation applications.

CHAPTER 5. FABRICATION OF METAL-LOADED GRAPHENE AEROGELS

5.1 Introduction

Aerogels are a class of porous materials that have extremely low density and high surface area. This makes them ideal candidates as catalyst supports and sensors. Graphene has received research interest due to its remarkable properties of electrical conductivity, high aspect ratio, chemical stability and the ability to be solution processed through the oxidation of graphite to produce graphene oxide (GO) as single layers. GO can be then be reduced to form sheets of electrically conductive reduced graphene oxide (rGO). Through lyophilization of graphene oxide suspensions, free-standing GO aerogels can be fabricated. To fully utilize the internal volume, rGO aerogel pores should be continuous throughout the bulk to allow reactants or analytes to penetrate the aerogel. The needle-like crystals of ice formed during rapid freezing of the GO suspension push the GO sheets into a columnar orientation in the freezing direction, affording long, continuous pores throughout the aerogel.

The surface chemistry of GO is complex and is sensitive to multivalent metal ions, which induce precipitation, making rGO-metal composite fabrication challenging. The negatively charged GO aggregates in the presence of multivalent ions forming GO hydrogels. To overcome this, chelating agents were used to screen the electrostatic interaction between the ions and GO, increasing the stability of dispersions. Lyophilizing a solution of well-suspended GO and chelated metal ions provides metal salt decorated GO aerogels where the GO and salt are simultaneously reduced to form metal decorated rGO aerogels. This chapter details the results of using chelating agents to get dramatic improvement in the loading of metals in graphene aerogels and how some control over particle size and surface density was realized by control of metal ion concentration and metal to chelator ratio.

5.2 Results and Discussion

5.2.1 RGO Aerogel Formation

Although aerogels are often formed through lyophilization of a gelled GO solution, we found that lyophilizing solutions with GO concentrations as low as 2.0 mg/mL formed stable free-standing aerogels with negligible shrinkage. Even though the mass of the aerogels were lowered by approximately 50% by reduction, the resulting aerogels were free-standing. Samples with lower concentrations collapsed during lyophilization. It was found that GO precursor solutions of 4 mg/mL were more stable and easier to handle than the relatively fragile aerogels formed at lower concentrations. The lack of shrinkage is readily apparent in Figure 19, which shows a GO solution and the resulting GO aerogel after freezing and lyophilization. The reduction process causes the aerogel to become black and conductive (10-100 Ω) whereas GO aerogels were light brown and insulating. Both the color change and change in electrical conductivity is commonly attributed to re-aromatization of the grapheme structure and removal of oxygenated sites. Figure 20 shows the morphology of the rGO aerogels.

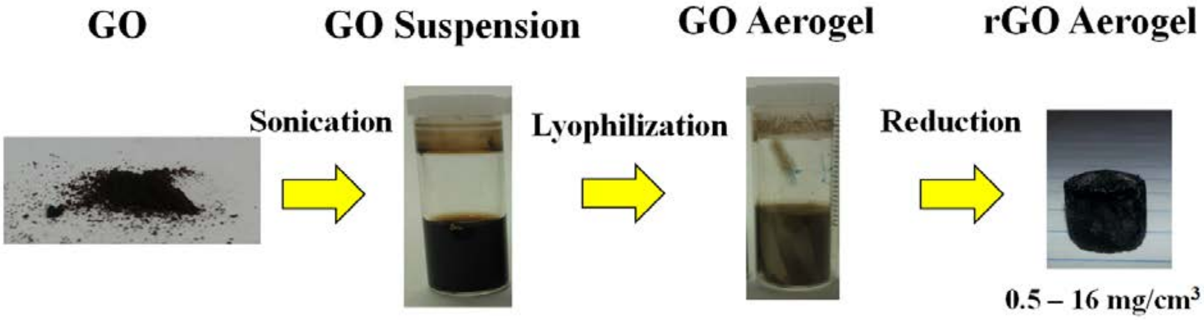

Figure 19. Schematic process of rGO aerogel fabrication.

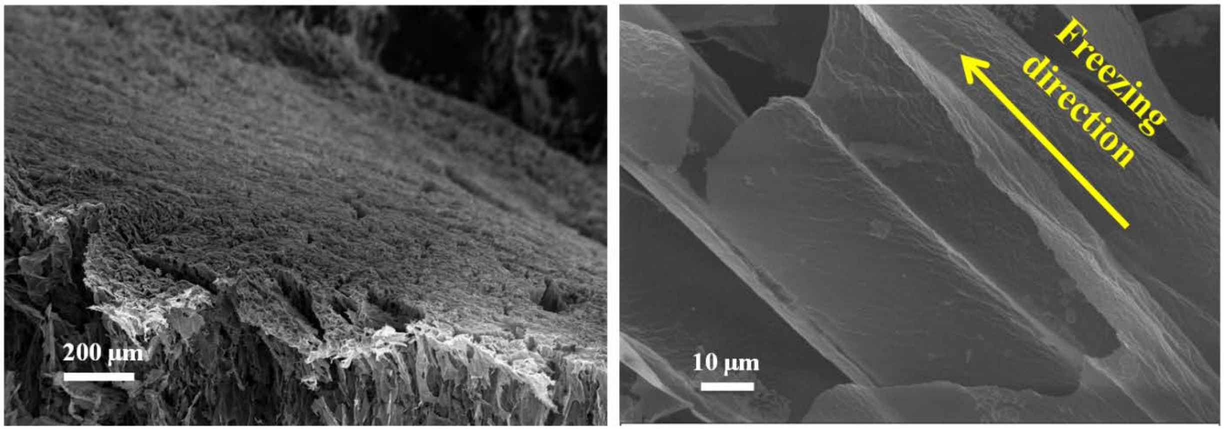

Figure 20. SEM micrograph of the top surface (left) and vertical cross-section of rGO aerogel.

5.2.2 Metal-Decorated Graphene Aerogels

The BET specific surface area for all the RGO-metal nanoparticles-decorated composites is between 852-1523 m^2g^{-1}. These specific surface areas are relatively high, compared to the RGO aerogels reported previously.[17] In addition, using 2600 m^2g^{-1} as the theoretical specific surface area for a single layer of graphene, it is possible to calculate the average number of layers in the RGO/graphene flakes in the aerogels. Aerogels loaded with Pd, Pt, and Ni nanoparticles have layer numbers of 3.0, 2.2, and 1.7 respectively. These numbers provide an indication of how agglomerated the graphene sheets are in the RGO composite material. This data is important in connecting aerogel composite morphology to its makeup.

The morphology of these high surface area and low density aerogels is of particular interest, especially that of the metal particles. To investigate this, a SEM study of each rGO aerogel was carried out Figure 20 which shows the morphology of the rGO aerogels. SEM images of a rGO aerogel show that the network frame of RGO aerogels are composed of graphene flakes and the aerogels possess three-dimensional pore-structure. This composite structure is composed of large pores structure due to ice crystal formation during the freezing process which is retained during lyophilization and reduction. In addition, these images illustrate that RGO nanosheets may loosely assemble at the surface to form smaller pores creating a high surface area structure.

Furthermore, due to the promising high surface area of this material it is of great interest to functionalize these structures. Because the chemical environment surrounding this structure can alter the bulk resistivity, it is a promising composite material for gas sensors, especially for hydrogen sensor. Metal and metal alloys are commonly used for these types of sensors as hydrogen’s affinity for the metal leads to adsorption, which alters the resistivity. Figure 21 shows SEM images of GO and loaded $NiCl_2$ salts after hydrogen reduction at 400^oC for 60 min. It was expected that these conditions would be sufficient to reduce the nickel salt to nickel metal. Unexpectedly, as shown in Figure 21, after reduction of this composite at 400^oC there is no evidence of nickel metal in any form. This may be due to the fact that more energy is needed to allow migration of nickel atoms across the graphene surface to aggregate, forming nanoparticles. To test this idea, the sample was placed back into the chamber and was re-heated to 900^oC in presence of hydrogen. The product of this reduction setup is shown in Figure 22 (a), where well dispersed Ni nanoparticles with a diameter ranging from 100-200 nm are evident. In addition to the Ni nanoparticles loaded onto the RGO aerogel, Pd metal nanoparticles were loaded using the same procedure as described above using $PdCl_2$ as the precursor. As shown in Figure 22 (b), the Pd nanoparticles have a smaller diameter (25-100 nm) than Ni nanoparticles. Moreover, these nanoparticles are homogeneously dispersed throughout the graphene sheets.

As it has been extensively reported that Pt readily adsorbs hydrogen, K_2PtCl_4 was used as Pt metal precursor[18]. Following the same procedure used for forming Ni and Pd nanoparticle decorated RGO aerogel composites, a Pt nanoparticles-RGO aerogel was successfully synthesized. Contrary to the nanoparticle morphology seen with Ni and Pd, the SEM micrograph in Figure 22 (c) shows that Pt nanoparticles form particle clusters with sizes ranging 2-5 μm throughout the graphene sheets. Within the nanoparticles clusters are Pt nanoparticles with diameters of 10-30 nm.

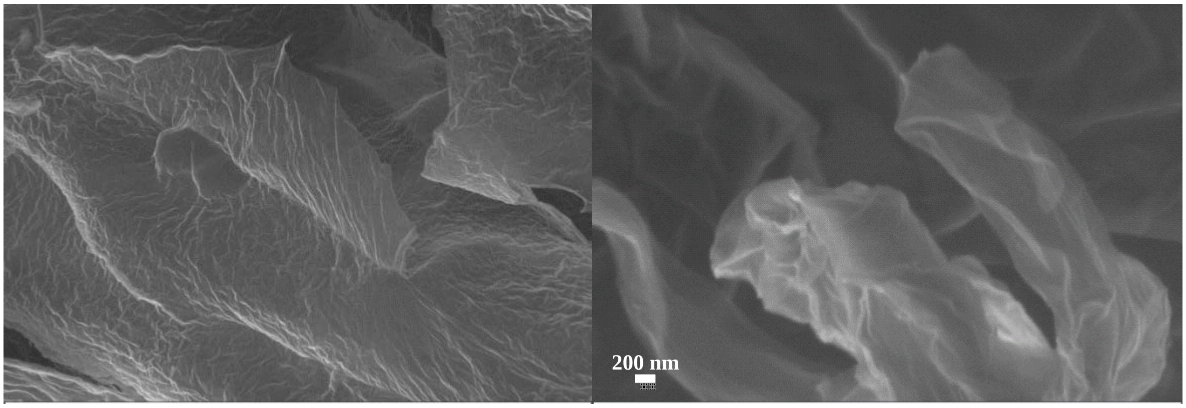

Figure 21. SEM micrograph of metal salt loaded rGO aerogel reduced at 400°C.

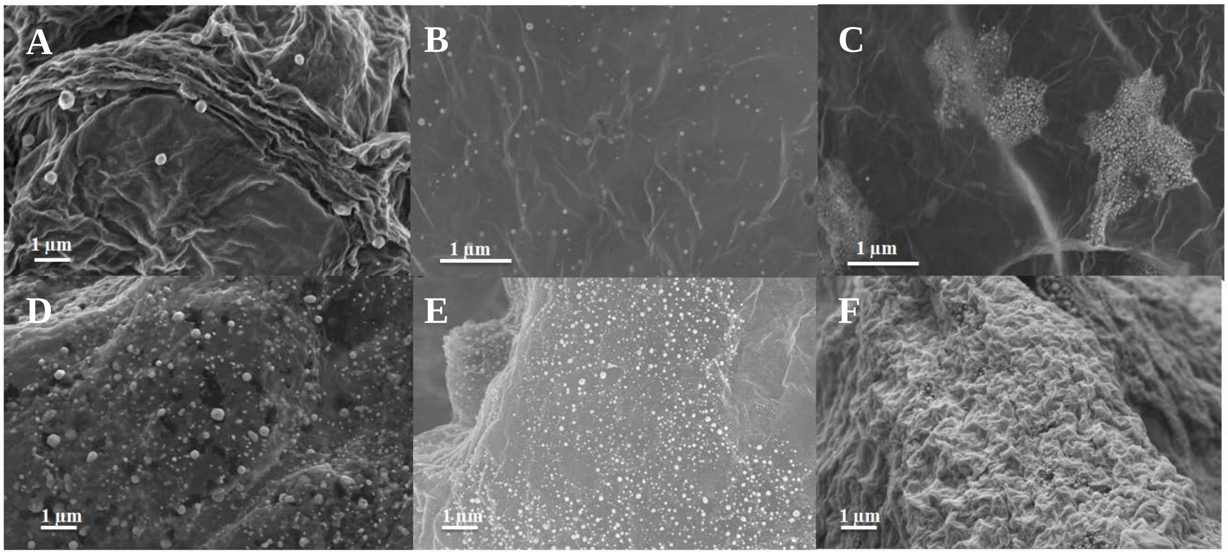

Figure 22. Metal decorated aerogel surfaces after reduction without (A-C) and with (D-F) chelating agent. A and D contain Ni, B and E contain Pd and C and F contain Pt.

Figure 23 and Figure 24 show the XPS analysis of GO aerogels loaded with Pt salt and after the reduction of Pt salt to form Pt nanoparticles. It is clear that Pt is present in the aerogel and that upon reduction, the oxygen concentration dramatically drops. Additionally, the Pt 4f7 peaks shift to a lower binding energy, which can be explained by their reduction from Pt^{2+} to metallic Pt[18]

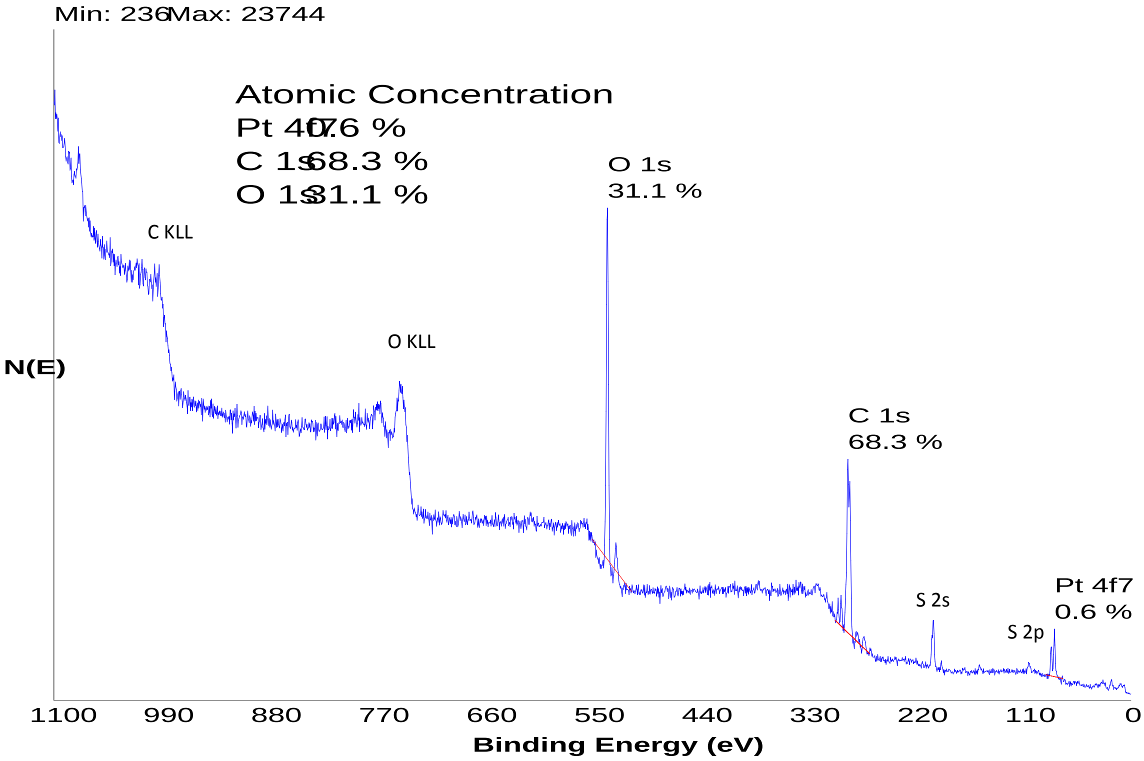

Figure 23. XPS spectra of GO aerogel loaded with K_2PtCl_4

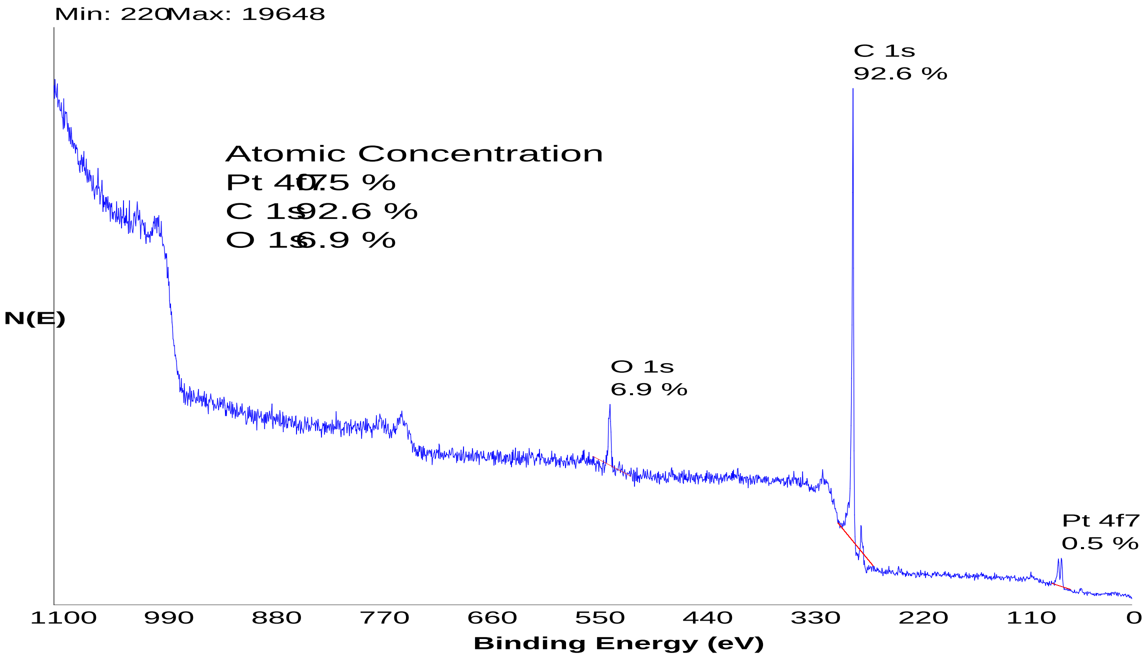

Figure 24. XPS spectra of RGO aerogel loaded with Pt nanoparticles

5.2.3 Using chelating agents to screen GO and metal ion electrostaticinteractions

GO aerogels were previously limited to a relatively low metal salt loading. We found that aerogels could only be formed with ratios of divalent metal ions of less than 0.75 mmol per gram graphene oxide (GO) for GO concentrations of 4 g/L. Ratios above 15 mmol ions per gram GO resulted in hydrogels that passed the inversion test but collapsed during lyophilization (Figure 25). Bai et al. found electrostatic interaction (ESI) from multivalent ions has been found to be an efficient cross-linker of graphene oxide, producing hydrogels which re-disperse upon addition of ethylenediaminetetraacetic acid (EDTA).[19] Based on these observations, the relatively strong ion-ion interactions between the metal and GO are not effective in producing stable aerogels. This could be because of a large hydration sphere surrounding the locations where metal ions bridge two GO sheets that stabilize a hydrogel, but become unstable upon removal of water. Because the freeze-drying process is the mechanism of forming the aerogels after lyophilization, it is not dependent so much on the assembly of GO sheets in solution. We only need homogeneous distribution of metal ions in the GO suspension before freezing which can be accomplished using hydrogen bonding. To reduce the ESI of added ions, we first introduced ligands containing functional groups that participate in hydrogen bonding and are known to bind strongly with Pt and Pd, such as EDTA, before introduction of GO. This allows for the relatively weak hydrogen bonding between the ligands and GO to be the dominant interaction so that after freeze-drying, ligated metal ions decorate the GO surface. The ligand is removed during the high temperature reduction process leaving behind metal nanoparticles that decorate the reduced GO aerogel.

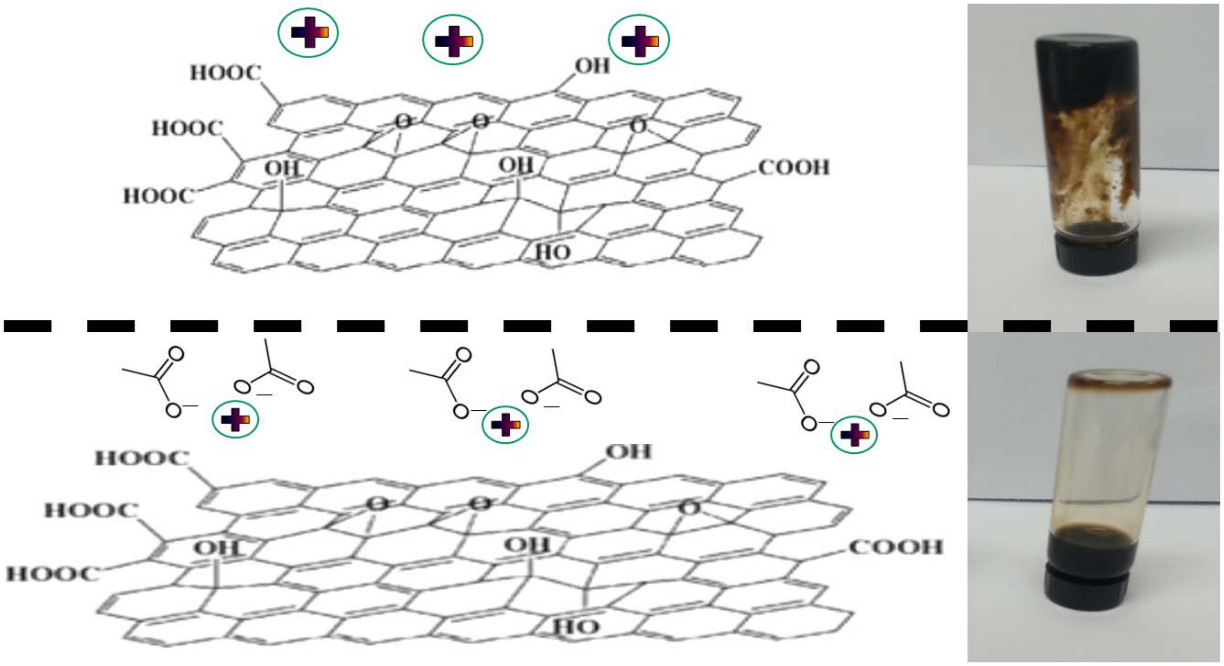

Figure 25. Schematic representation of GO and metal salts in suspension (left) and the results of the corresponding inversion test (right(. GO-metal salt dispersions without chelator (top) to screen electrostatic interaction between the sheets have relatively strong interactions between the multivalent ions and carboxylate groups on the GO resulting in flocculation and gelation (top right). With chelator (bottom), the dispersion is stable and remains a flowable liquid that can be lyophilized into aerogels.

While Pd loaded aerogels could be prepared using EDTA, both the EDTA complexes with $PtCl_4$ and $PtCl_2$ offered poor Pt solubility and resulted in aerogels with reduced volume (60%) and macroscopic pores (~0.7mm). Because Pt coordinates strongly through nitrogen lone pairs, several ligands were tried including bi- and tri- primary, secondary and tertiary amines, but all ligands produced similar results even at lower temperatures (~4°C). We believe this is due to the partial reduction of GO by nitrogen containing compounds, increasing the hydrophobicity of GO which induces sheet aggregation. This phenomenon is clearly demonstrated by the rapid color change of light brown GO solutions to black in a matter of seconds with the addition of disodium EDTA. This reduction is not evident in Pd-EDTA complexes because of the stronger interaction of Pd with the nitrogen on EDTA, preventing reduction.

As a simple solution to this, sodium acetate was used as a model compound to screen the Pt ESI with GO while limiting GO reduction. $PtCl_2$ in sodium acetate solutions were sparingly soluble, but $PtCl_4$ was found to be very soluble with $PtCl_4$:sodium acetate mole ratios of 1:1 and above, forming bright orange solutions. Further, stable GO aerogels could be prepared using these Pt salt solutions at concentrations of up to 100mM. This is very promising, as Pt loaded aerogels have proved to be more sensitive than their Pd counterparts in our initial study (0.8% vs. 0.03% for Pd). The reduction of these aerogels is ongoing, and will be followed by hydrogen sensing analysis.

Further, some degree of control of nanoparticles surface density and particle size could be controlled using different metal ion concentrations and electrostatic interaction screening agent ratios. Figure 26 depicts a drastic change of nanoparticles size and distribution on the graphene aerogel surfaces due to different Pt and sodium acetate concentrations. At a constant Pt concentration, increasing sodium acetate leads to larger particle sizes. The underlying reason of this is yet unexplained because of two reasons. Firstly, larger sodium acetate concentrations should yield better screening of charge, and thereby produce more uniformly distributed Pt and GO sheets, which is not the case. Overview SEM images show that the overall aerogel morphology between different concentrations show little or no change, which is expected because the primary aerogel morphology forming influence is ice crystallization. Secondly, the actual formation of particles occurs at high temperature or upon cooling, so a more exotic mechanism such as spalling upon cooling could be at work that is difficult to observe. Also, doubling the Pt content doesn't seem to change particle size as much as particle density. This can be explained by the fact that nanoparticles formation occurs at 900°C, and could be due to a thin semi-melt of Pt over the graphene surface, which forms particles upon cooling.

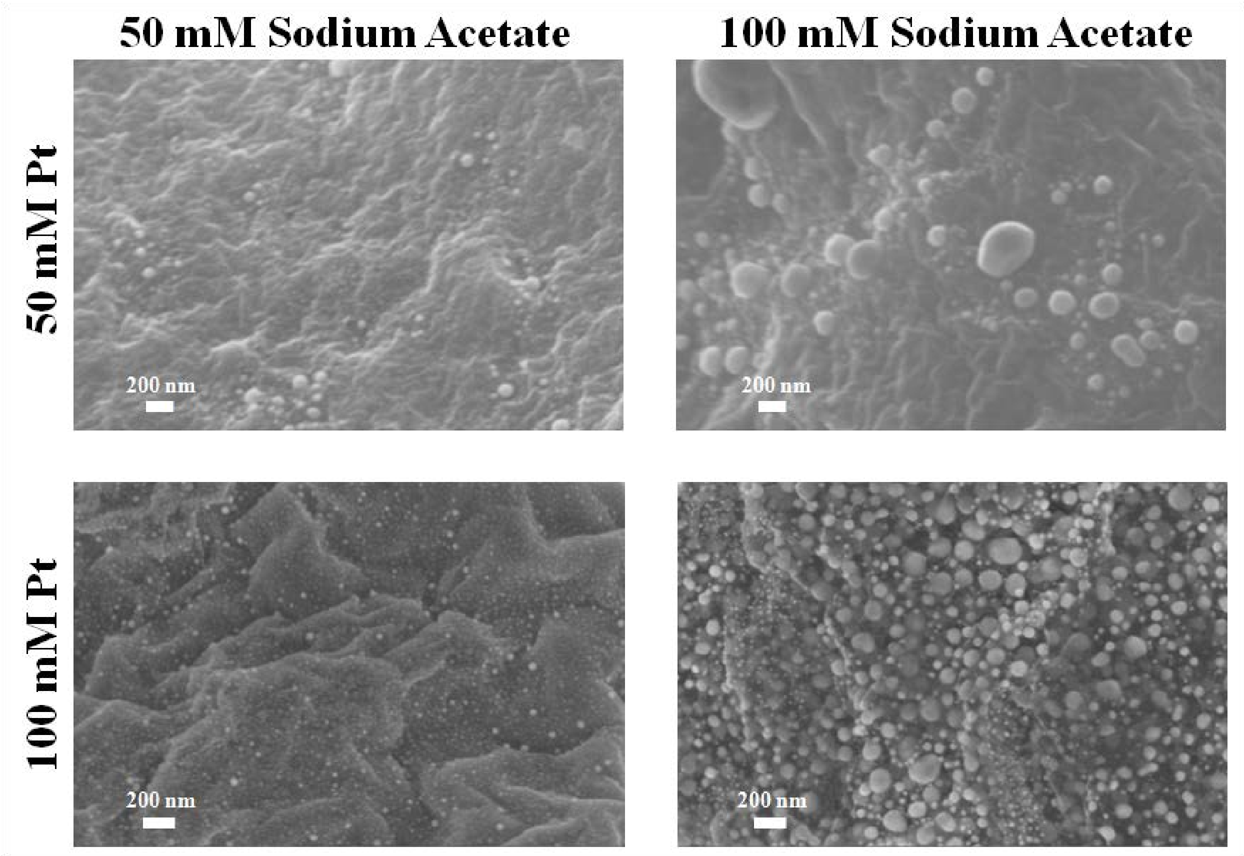

Figure 26. SEM micrographs of Pt-decorated RGO aerogels with various Pt and sodium acetate solution concentrations prior to lyophilization and reduction.

5.3 Conclusions

Due to the highly porous nature of these RGO aerogels, in situ loading of metal salts which are co-reduced with the GO provides the most likely solution to homogenous and extensive metal functionalization of the surfaces. The greatest impediment to this process is that flocculation induced gelation of the GO-metal salt solutions prior to lyophilization. With proper use of chelating agents as electrostatic screening agents, the metal loading could be increased by more than 30 times. Further, it was found that by judicious control of metal salt and chelating agent some control of the nanoparticles surface density and particle size could be controlled. This is of great potential interest to sensors, catalysts and other devices.

CHAPTER 6. PALLADIUM-LOADED REDUCED GRAPHENE AEROGELS FOR HYDROGEN GAS SENSING

6.1 Introduction

Hydrogen gas is critically important to a wide range of fields, both commercial and academic. However, owing to difficulty of storage, a relatively high explosion risk, and difficulty in detection, the need for an effective, reliable, and fast-acting hydrogen sensor is an ever-growing one. Since hydrogen gas is explosive at concentrations as low as 4% in air, safety at facilities that employ hydrogen gas can be dramatically improved by a sensor with a low limit of detection that can respond to changes in hydrogen concentration very quickly.

Graphene aerogels are low-density structures composed of sheets of graphene that are stabilized by pi-pi interactions. Materials made from reduced graphene oxide have been shown to have semiconductor properties, which lends them to use in electrochemical sensors. Because of the exceptionally high surface area and gas-permeability of aerogel materials, it is speculated that sensors made from them will be faster and have lower limits of detection than comparable film-based sensors.[18b]

6.2 Results and Discussion

6.2.1 Pd-decorated RGO aerogels for hydrogen sensing

In order to determine the influence of processing and experimental conditions of the aerogels on hydrogen sensing, RGO aerogels attached to electrical leads was inserted into a flow chamber. It was quickly found that variation in room temperature due to air-conditioning cycling caused relatively dramatic changes in aerogel resistivity, reducing measurement sensitivity. To solve this, the flow chamber was placed in a thermostat controlled water bath and a thermocouple was added to the interior of the flow chamber. This allows for further studies regarding the temperature dependence on sensor response. Pd was chosen as the metal for hydrogen sensing because it has a known affinity for hydrogen. Such affinity causes the electron density of the metal particle to be reduced, thereby increasing the work function of the graphene-metal-gas system.[18] A schematic diagram showing the mechanism of conductometric hydrogen gas sensing is seen in Figure 27.

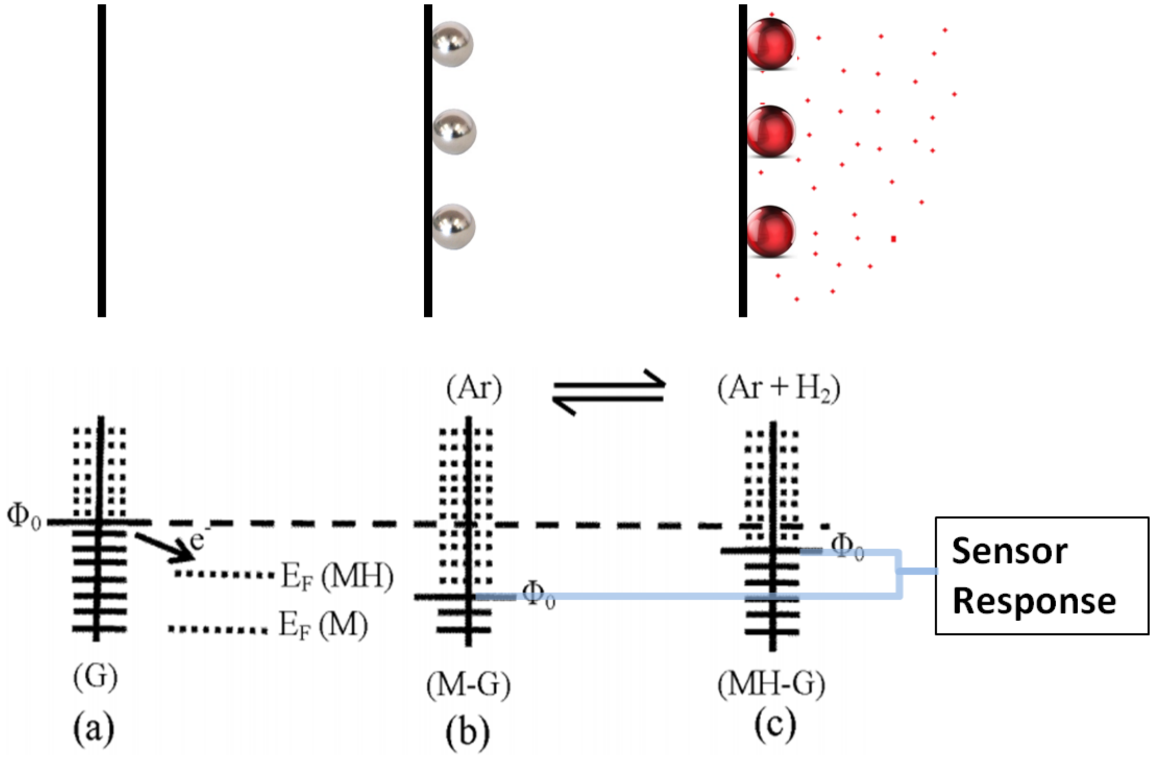

Figure 27. Schematic showing the mechanism of conductometric response hydrogen gas. A-C on the top depicts bare graphene aerogel wall (vertical black line), coated with metal nanoparticles (grey spheres), and those metal nanoparticles in the presence of hydrogen gas (red), respectively. The bottom three depict the corresponding Fermi energy levels of each of the states.

Conductometric response to hydrogen gas was carried out by monitoring the current through each aerogel under the condition of a steady flow of inert gas with periodic inclusion of 1000ppm hydrogen gas into the stream. To get a clear idea of the sensor response, the relative change in resistivity (ΔR/R %) was calculated from the current and the voltage applied. These values were plotted, after baseline correction, as a function of time. A plot of % change in conductance plotted vs. time over four on-off cycles of hydrogen is shown in Figure 28. The sensor response depends on the Pd loading and does not uniformly increase with increasing Pd content.. A summary of the data collected for each aerogel with different loadings are summarized in Table 1. It should be noted that the resistivity of samples with Pd is much lower than those without, but that increasing Pd concentration doesn’t affect the resistivity further. This shows that the primary conductivity enhancement comes from the interfacial effect and not from total loading. Figure 29 shows the dependence of sensor response on Pd concentration with a clear peak at 30 mM Pd precursor concentration.

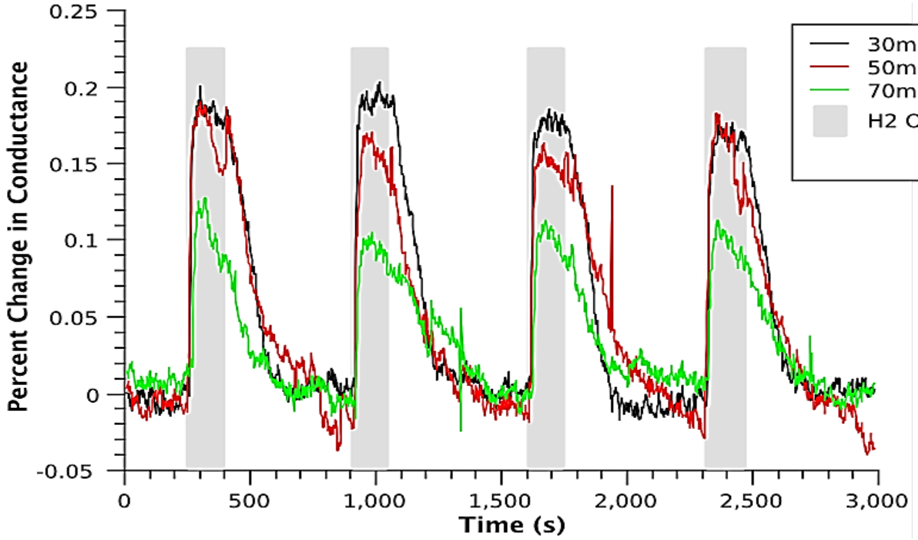

Figure 28. Sensor responses of different loadings of Pd salt precursors showing reversible responses during cycling of Hydrogen gas.

Table 1. Summary of Pd salt loaded rGO aerogel properties

Metal Salt Added (µmol)	Density (mg/cc)	R (Ω*cm)	BET Surface Area		Sensor Response %*(R-R_o)/R_o
			(m^2/g)	(m^2/cc)	
0	1.56	950	947	1.48	0%
3 (no EDTA)	7.25	115	852	6.18	0.02%
3	7.31	28.6	99	0.72	0.03%
10	13.5	16.2	190	2.57	0.12%
30	25.3	21	328	8.31	0.19%
50	38	17.7	304	11.55	0.17%
70	51.7	22.1	249	12.88	0.11%

This trend shows the effects of two conflicting effects. With increasing Pd concentration, the total surface area increases, leading to a per-device increase in sensitivity. Along with this is the reduction of each portion of Pd's direct interaction with graphene due to increasing particle size. This effect was explored in the last chapter in the comparison (Figure 26) of metal loading and chelator loading on the metal particle size. Because in this study, the chelator and metal salt were kept at a constant ratio, the particle size increases with increasing loading. It is expected that the concentration of ~30mM Pd let to the most complete coverage of the surface, while keeping particle size to a minimum.

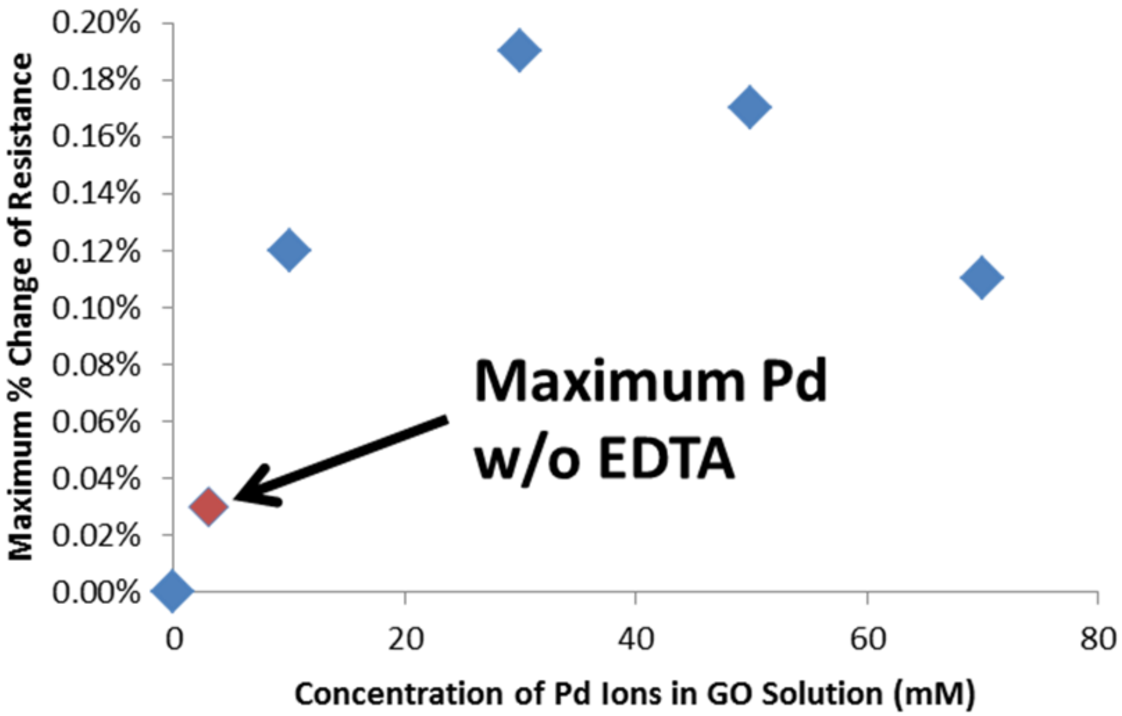

Figure 29. Graph of sensor response plotted against Pd loading.

6.3 Conclusions

Using the morphological control of particle size developed in CHAPTER 5 and the techniques to get improved Pd loading onto RGO aerogels, a reversible hydrogen sensor was developed. The sensor showed a conductometric response of up to 0.2% change in resistance upon exposure to 1000ppm hydrogen gas. A morphology-performance relationship was developed to explain maximal sensor performance at sub-maximal Pd loading. All measurements were conducted at room temperature, which is an advantage in this industry as it most closely mimics the environs of hydrogen gas storage areas. This work can lead to relatively cheap sensor devices that do not depend on microfabrication techniques such as lithography or an underlying silicon substrate. Certainly, environmental effects such as temperature and humidity play a critical role in this type of sensor and should be explored.

CHAPTER 7. FUNCTIONALIZATION AND FABRICATION GRAPHENE AEROGELS FOR HIGH-PERFORMANCE ASYMMETRIC SUPERCAPACITORS

7.1 Introduction

Bridging the properties of batteries and conventional capacitors, supercapacitors (SCs) are an emerging technology that fills a crucial gap in today's rapidly evolving energy storage needs. With desirable properties of high power density, fast charge-discharge rate, and excellent cycle stability [20], SCs can be used in a wide range of applications such as hybrid vehicles, portable electronics, pacemakers, etc [21]. Improving the energy density of SCs is critical for widespread use. The energy density of a SC is calculated using the equation $E=1/2CV^2$, where E is the energy density, C is the cell capacitance, and V is the cell voltage [22]. Obviously, the exponent of 2 in the above equation makes the cell voltage to play an essential and efficient role in enhancing energy density. There are two major approaches to broaden the cell voltage. One is to use organic or ionic liquid electrolytes which raise the voltage window up to 3 V [23]. However, the toxicity, high-cost, and poor ionic conductivity of organic electrolytes and the limitation of working temperature of ionic liquid electrolytes make this approach unfavorable. Second is to develop aqueous electrolyte-based asymmetric supercapacitors (ASCs), which include a battery-type Faradic cathode as an energy source and a capacitor-type anode as a power source [24]. An ASC takes advantage of the different voltage windows of both the cathode and anode so that an enhanced operation voltage in a cell system can be readily achieved, resulting in an improved specific capacitance and substantially boosted energy density.

Despite the considerable effort dedicated towards the development of cathode materials such as MnO_2 [25], NiO [26], $Ni(OH)_2$ [27], CoO_x [28], etc, less attention is focused on anode material development. Carbon-based materials commonly serve as an anode in ASCs including activated carbon [9, 29], carbon nanofiber [30], carbon nanotube (CNT) [31], graphene [32], etc. Among them, graphene has stood out due to its outstanding characteristics such as large surface area, solution processability, high electrical conductivity, excellent mechanical properties, and superior electrochemical stability [1a, 33]. However, a significant surface area loss is normally observed during processing because of the aggregation of graphene nanosheets [34], resulting in a reduced electrochemically active area which considerably limits the specific capacitance. A feasible approach is to fabricate graphene nanosheets into a graphene aerogel (GA); a stable 3D network which can effectively hamper the aggregation of graphene nanosheets [35]. The GA electrode's open 3D network structure provides maximal active surface area while the honeycomb structure (~10 µm pore diameter) facilitates effective electrolyte ion transportation. One significant limitation is that the oxidation-reduction process lowers the electrical conductivity relative to pristine graphene due to defect site formatiofigure 1. Therefore, it is advantageous to fabricate a GA with enhanced electrical conductivity. Functionalization of the GA with metal nanoparticles increases the bulk electrical conductivity as the metal nanoparticles preferentially anchor at the otherwise electrical impeding defect sites [36], and lowers the work function of the composite [18a].

This is a novel functionalized GA fabrication method of producing a high surface area electrode material (328 m^2 g^{-1}) for ASCs. In this method, palladium (Pd) nanoparticles are introduced into the 3D network structure of GA (denoted as P-GA), which reduces the electrical resistivity from 950 to 16 Ω cm (more than 50 times improvement). Although Pd is a relatively expensive metal, it is environmentally and electrochemically stable, making it a potential candidate to improve the device performance. Electrodes prepared based on P-GA show high specific capacitance (175.8 F g^{-1} at 5 mV s^{-1}), excellent rate capability, superior columbic efficiency, and remarkable reversibility. Moreover, ASCs assembled using this functionalized GA show stable extended cell voltage, fast charge-discharge capability, excellent cycle stability, and high energy and power densities. In addition, the applicability of this ASC is further demonstrated in energy storage by lighting up a LED, highlighting the significant potential of our functionalized GA for high performance energy storage devices.

7.2 Results and Discussion

7.2.1 Fabrication and characterization of P-GA

Fabrication of P-GA, as shown in Figure 30(a), involves two major steps: (1) lyophilization of a well-dispersed graphene oxide (GO) sheets and $PdCl_2$/EDTA solution and (2) reduction of the GO aerogel with embedded Pd salt through low temperature hydrazine vapor and high temperature hydrogen separately. GA samples were prepared in an identical manner, except without addition of $PdCl_2$/EDTA solution. This gas-phase reduction technique was utilized to retain the porous 3D morphology in the GA while providing highly reduced GO. The GO aerogel loaded with Pd salt has a brown color, while the reduced P-GA exhibits a black sponge-like appearance. The 3D morphology of as-prepared GA is verified by scanning electron microscopy (SEM) characterization. A well-defined and interconnected framework of ultrathin graphene nanosheets with a porous structure can be easily observed in Figure 30(b). From the enlarged image in Figure 30(c), ripples and wrinkles are evidenced on the graphene nanosheets, which may have been caused by the high surface energy combined with the strain formed during the thermal reduction process [37]. As displayed in Figure 30(d), Pd nanoparticles were embedded onto

GA with a uniform dispersion. The specific surface area and volumetric surface area of GA are 947 m^2g^{-1} and 1.48 $m^2\,cm^{-3}$, respectively. For P-GA, the specific surface area decreases to 328 $m^2\,g^{-1}$ due to the high density of Pd, while the volumetric surface area increases to 8.31 $m^2\,cm^{-3}$ due to an increase in the surface roughness. Furthermore, the BJH pore size distribution centered at ~ 2 nm for both GA and P-GA (Figure 31), suggesting the loading of Pd does not affect the pore size distribution. The electrical resistivity is decreased from 950 Ω cm to 16 Ω cm when samples are loaded with Pd nanoparticles. This is due to the fact that defect sites on the GO act as anchors for nanoparticle formation [36], effectively bridging insulating areas. This, as well as the well-known effect that the metal nanoparticles are able to lower the composite's work function [18a], which produces higher electrical conductivity, and therefore improved capacitance as charge more efficiently travels though the electrode.

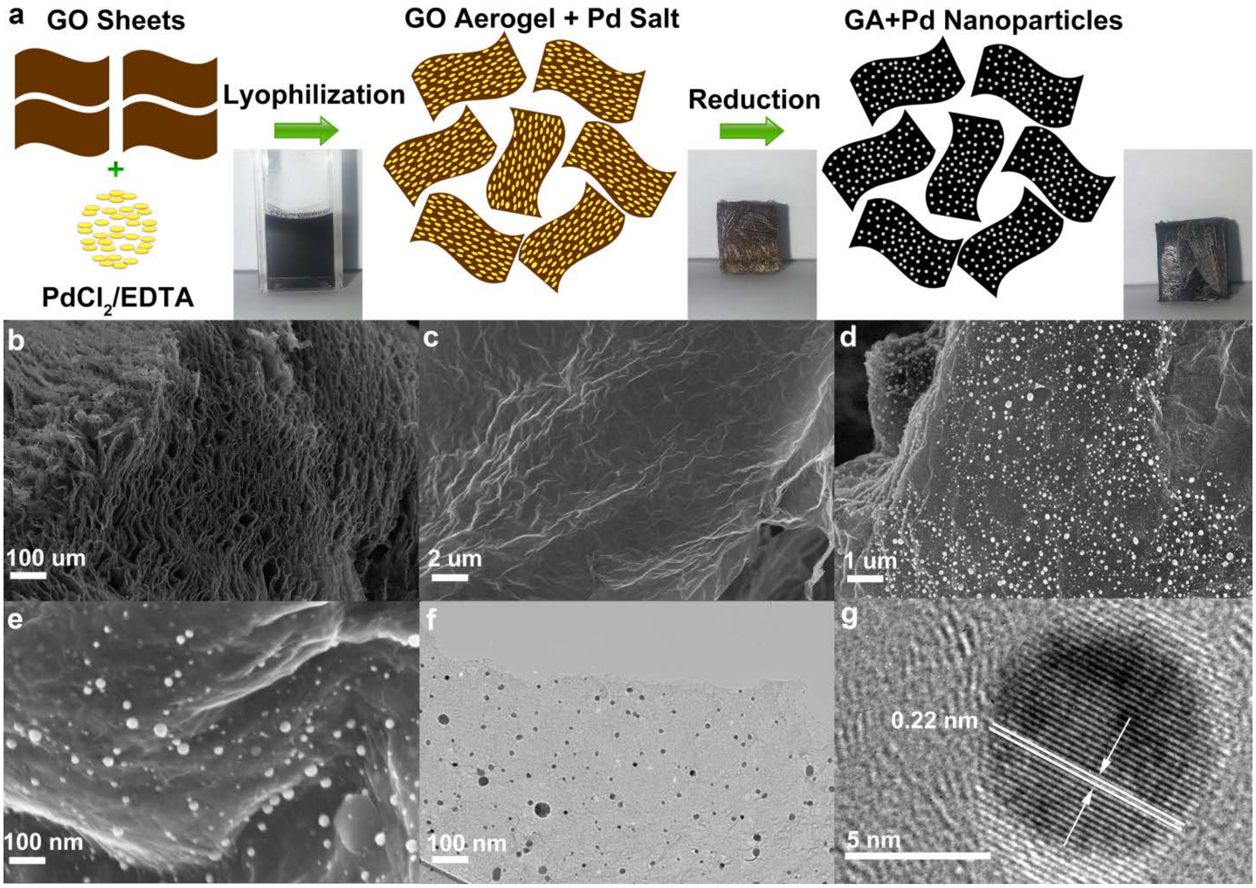

Figure 30. (a). Schematics illustration showing the fabrication process of P-GA. SEM images of the (b, c) GA and (d, e) P-GA. (f) TEM and (g) HRTEM images of P-GA.

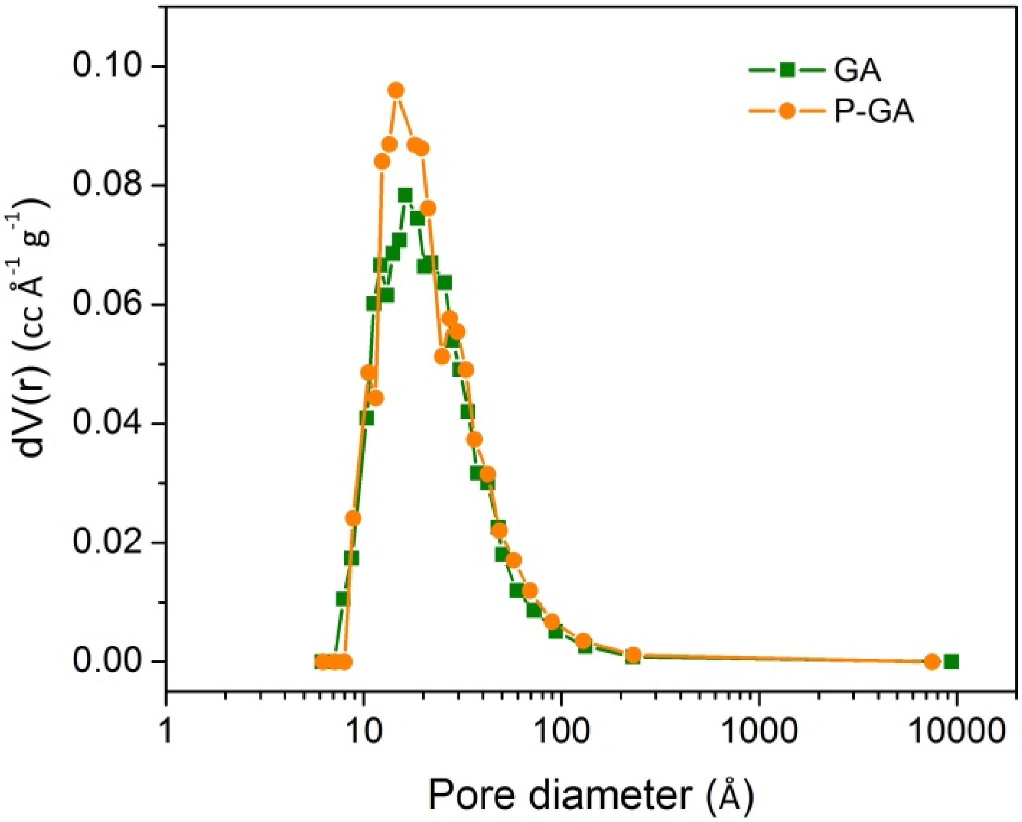

Figure 31. BJH pore size distribution of GA and P-GA

The size of the Pd nanoparticles ranges from a few nanometers to several dozens of nanometers (Figure 30 (e)). Local energy-dispersive X-ray spectroscopy (EDS) analysis was also performed for the P-GA (Figure 32). In addition to the carbon peak from the graphene nanosheets, signal of Pd peak was clearly detected in the spectrum. The uniform dispersion and size distribution of Pd nanoparticles are further confirmed by transmission electron microscopy (TEM) as shown in Figure 30(f). In addition, Pd nanoparticles are located in between the graphene nanosheets, as shown in Figure 33, suggesting that the Pd nanoparticle might also help in preventing the restacking of graphene nanosheets. A high resolution TEM is provided in

Figure 30(g) to examine the crystallinity of Pd nanoparticles. The fringe spacing of the particle lattice is 0.22 nm, which agrees well with the (1 1 1) lattice spacing of face-centered cubic (fcc) Pd (0.224 nm).

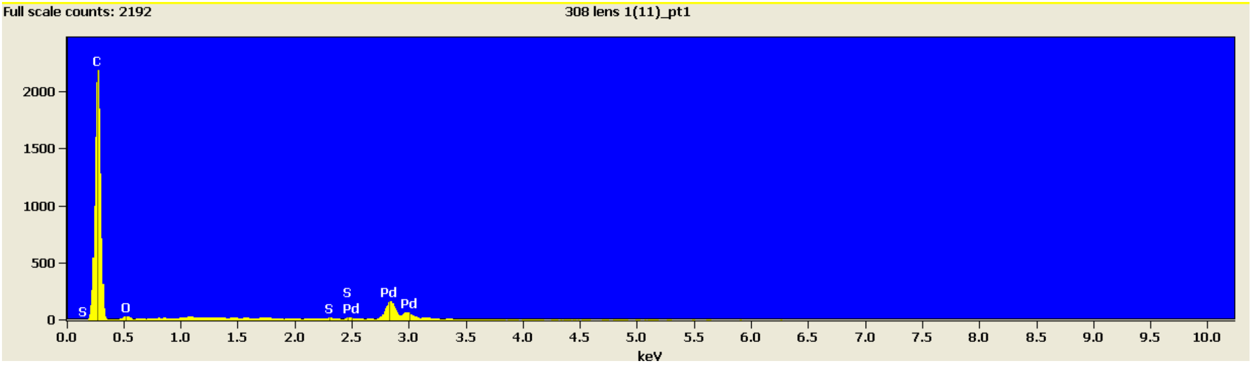

Figure 32. EDS spectrum for the P-GA.

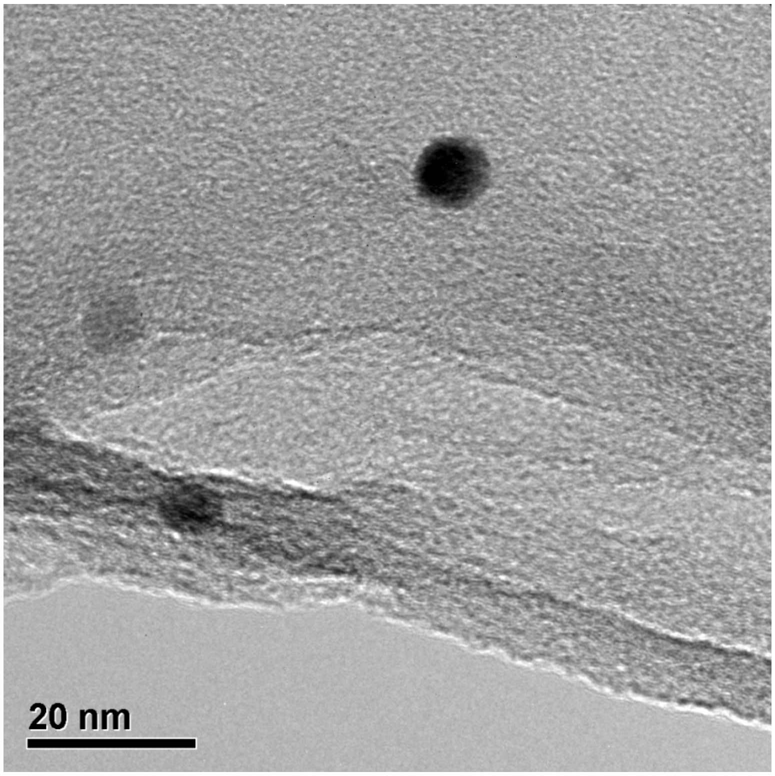

Figure 33. TEM image of P-GA. The difference in the darkness of the Pd nanoparticles provide an impression that the nanoparticles are located at different depths.

The chemical composition of P-GA was analyzed using X-ray photoelectron spectroscopy (XPS) in Figure 34. Deconvoluted C 1s spectra shows five peaks which correspond to sp^2 C – C bonds of graphene at 284.6 eV, alcohol, phenolic, and ether C – O bonds at 286.2 eV, carbonyl C = O bonds at 287.2 eV, carboxyl O = C – O bonds at 289.3 eV, and carbonitride C – N bonds at 285.6 eV (Figure 34(a)) [35a, 35c]. The presence of C – N bonds may attribute to either a residual product of EDTA or the hydrazine reduction process. The efficient reduction of GO is evidenced in the XPS spectrum where the contribution of the C-C signal makes up most of the total C1s signal. The binding energies of 335.5 eV and 340.8 eV correspond to Pd 3d$_{5/2}$ and Pd 3d$_{3/2}$ for the metallic Pd^0, respectively (Figure 34(b)) [38], further confirm the presence of metallic Pd. Additionally, Pd^{2+} binding energies at 343.2 eV and 337.9 eV were also observed, which is likely due to surface oxides on the Pd nanoparticles. Additionally, table S1 in SI exhibits the carbon/oxygen (C/O) ratio of GA and P-GA before and after reduction. C/O ratio of GA and P-GA are fairly close (1.99 and 1.83) before reduction. After reduction, these two values considerably enhance to 5.52 and 4.20 for GA and P-GA, respectively, indicating the graphene oxide has been reduced. The difference of C/O ratio after reduction between GA and P-GA might be attributed to EDTA that was added during the synthesis of P-GA.

Table 2. C/O ratio of GA and P-GA before and after reduction.

Sample	C/O ratio	
	Before reduction	After reduction
GA	1.99	5.52
P-GA	1.83	4.20

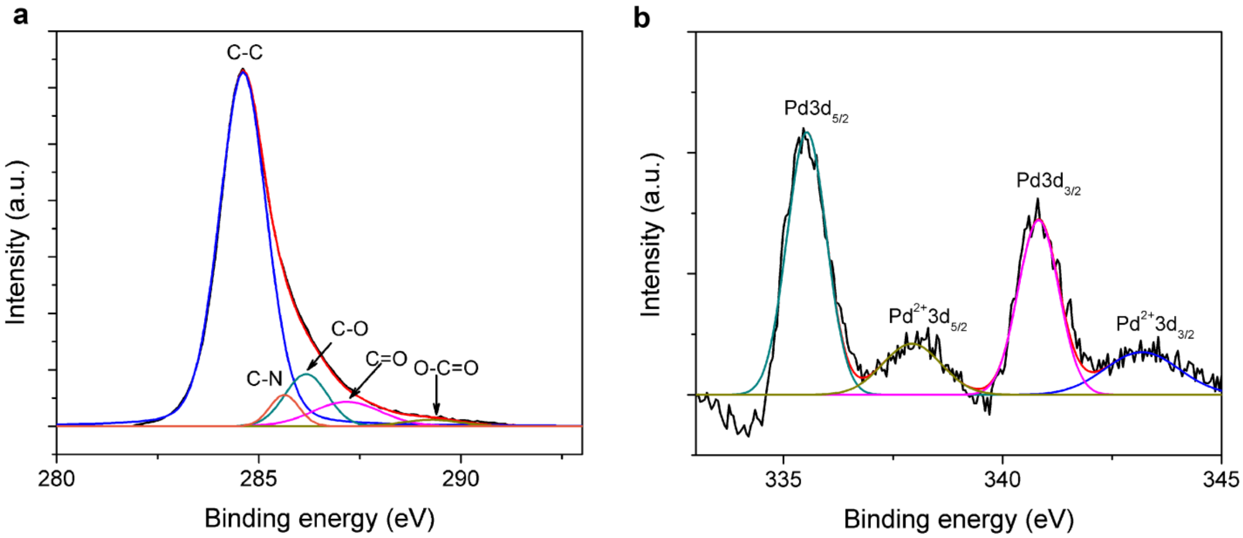

Figure 34. (a) Schematics illustration showing the fabrication process of P-GA. SEM images of the (b, c) GA and (d, e) P-GA. (f) TEM and (g) HRTEM images of P-GA.

7.2.2 Electrochemical performance of electrodes

As the aerogel structure provides highly enhanced surface area and Pd nanoparticles improve the electrical conductivity, P-GA was tested as an electrode material for SCs. The electrochemical studies for the individual electrodes were conducted in a three-electrode configuration in 0.1 M sodium sulfate (Na_2SO_4) electrolyte, with a platinum counter electrode and a saturated calomel electrode (SCE) reference electrode. The Pd content is optimized in this study. Figure 35 shows the electrical resistivity of GA with different Pd precursor ($PdCl_2$) loading concentrations ranging from 0 to 36 mM. The electrical resistivity drops dramatically with increased Pd ion concentrations from 0 to 9 mM, continues to decrease from 9 to 18 mM, then saturates upon increasing the concentration. In addition, cyclic voltammetry (CV) curves of P-GA synthesized from different $PdCl_2$ concentrations ranging from 9 ~ 36 mM are shown in Figure 36. The CV curve of P-GA obtained at a concentration of 18 mM shows larger area than the one at 9 mM, indicating the electrical conductivity is enhanced by introducing more Pd content. However, the

CV curve of P-GA obtained at 18 mM has larger area than the one at 36 mM, revealing that increasing the Pd content after a certain amount does not boost the specific capacitance due to the increased weight contribution from Pd. Therefore, it is a tradeoff between the enhancement of electrical conductivity and the added Pd mass. As a consequence, the P-GA obtained at 18 mM was selected for this study. Figure 37(a) shows the CV collected for P-GA and GA electrodes at a scan rate of 50 mV s^{-1}. The P-GA electrode exhibited much higher current density than GA electrode, indicating better electron transportation. Figure 37(b) shows the CV of P-GA electrode at different scan rates (5 – 500 mV s^{-1}) with a negative voltage window ranging from -0.8V to 0 V. The consistency of these box-like curves at various scan rates reveals the excellent capacitive behavior of P-GA electrode. Figure 37(c) shows the specific capacitances and rate performance of P-GA electrode at various scan rates. The highest specific capacitance obtained for the P-GA electrode was 175.8 F g^{-1} at a scan rate of 5 mV s^{-1}, which is much higher than the value obtained for the GA electrode (51.9 F g^{-1} at 5 mV s^{-1}) and other previously reported carbon aerogel based electrodes [39]. Moreover, the P-GA electrode shows excellent rate capability, with retention of 48.3% of the initial capacitance as the scan rate increases from 5 to 500 mV s^{-1}. It is worth mentioning that the current collector (including both the Ni substrate and Ag paint) has negligible contribution to the capacitance compared to P-GA (Figure 38). Nevertheless, all the specific capacitances of electrodes are calculated based on capacitance after the subtraction of the contribution from current collectors. Galvanostatic charge-discharge (GCD) curves collected for the P-GA electrode is shown in Figure 37(d). The consistent observation of symmetrical GCD curves at various current densities implies the superior columbic efficiency and excellent reversibility of the P-GA electrode. The above experimental results demonstrate that the P-GA electrodes have great potential as high performance negative electrodes.

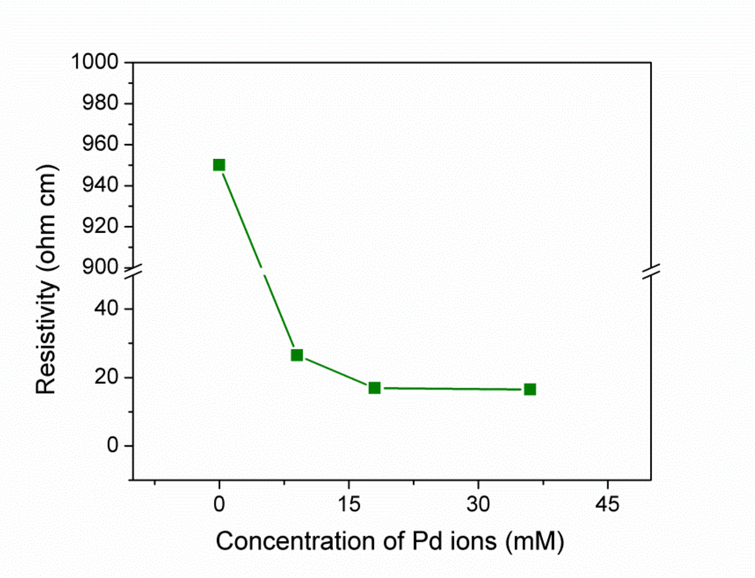

Figure 35. Electrical resistivity of P-GA obtained from $PdCl_2$ at different precursor concentrations.

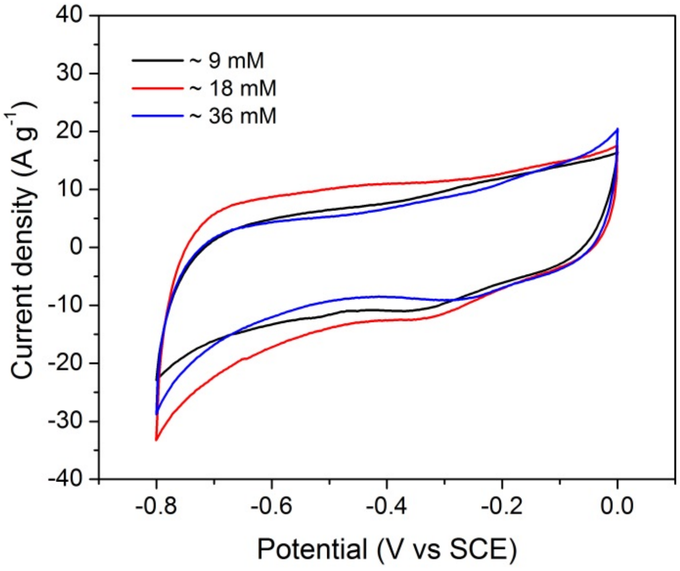

Figure 36. CV curves of P-GA obtained from $PdCl_2$ at different precursor concentrations. We used the data obtained from the 18 mM sample for comparison to that of pristine GA.

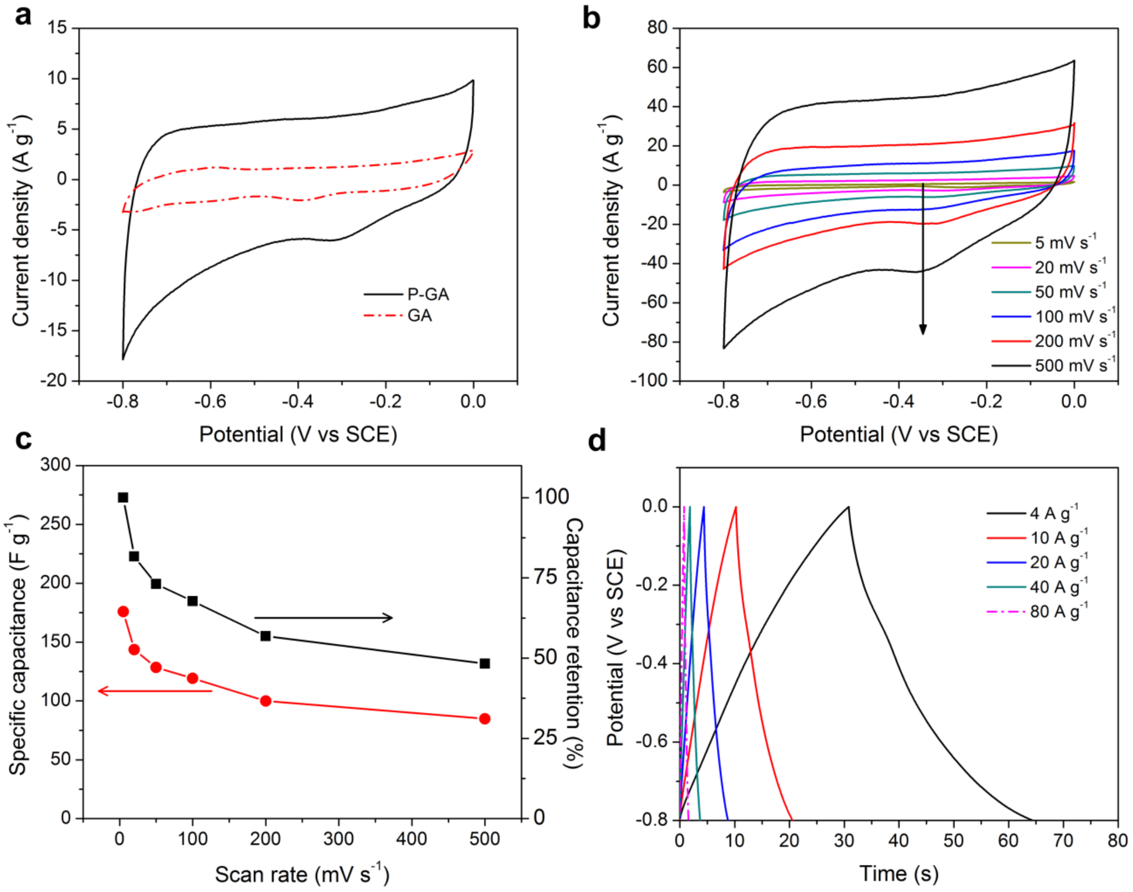

Figure 37. (a) CV curves of P-GA and GA electrodes at a scan rate of 50 mV s^{-1}. (b) CV curves of P-GA electrode at different scan rates (5 – 500 mV s^{-1}). (c) Specific capacitance and capacitance retention for the GA electrode as a function of scan rates. (d) GCD curves of P-GA electrode at different current densities (4 – 80 A g^{-1}).

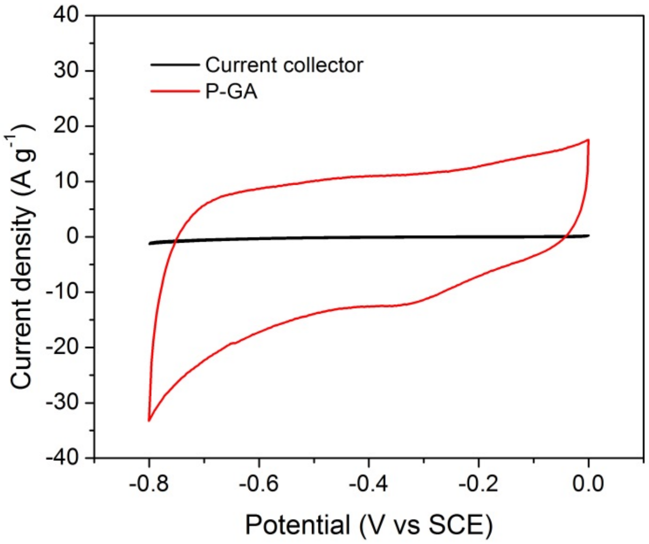

Figure 38. CV curves of P-GA and current collector.

At the same time, an electrode based on MnO_2 was selected as potential cathode for our study. CV of MnO_2 electrode was carried out with a positive voltage window ranging from 0V to 0.8V (Figure 39). The CV curves present consistent box-like shapes as the scan rate increases from 5 to 500 mV s^{-1}, implying good capacitive properties of MnO_2 electrode. Figure 40(a) shows the CV curves of both P-GA and MnO_2 electrodes at a scan rate of 50 mV s^{-1}. The two rectangular shaped CV curves occupy a voltage window from -0.8 V to 0.8V, implying an ASC device assembled from these two electrode could have a potential voltage window of 1.6 V. Specific capacitances of MnO_2 and P-GA at 50 mV s^{-1} are 243.7 and 128.5 F g^{-1} separately (Figure 41). The different specific capacitance of P-GA and MnO_2 electrodes will lead to a mismatching of charges stored. In order to keep the charge balance ($q+=q-$), loading mass of active material from cathode and anode should be adjusted and kept at a constant ratio of ~ 0.53.

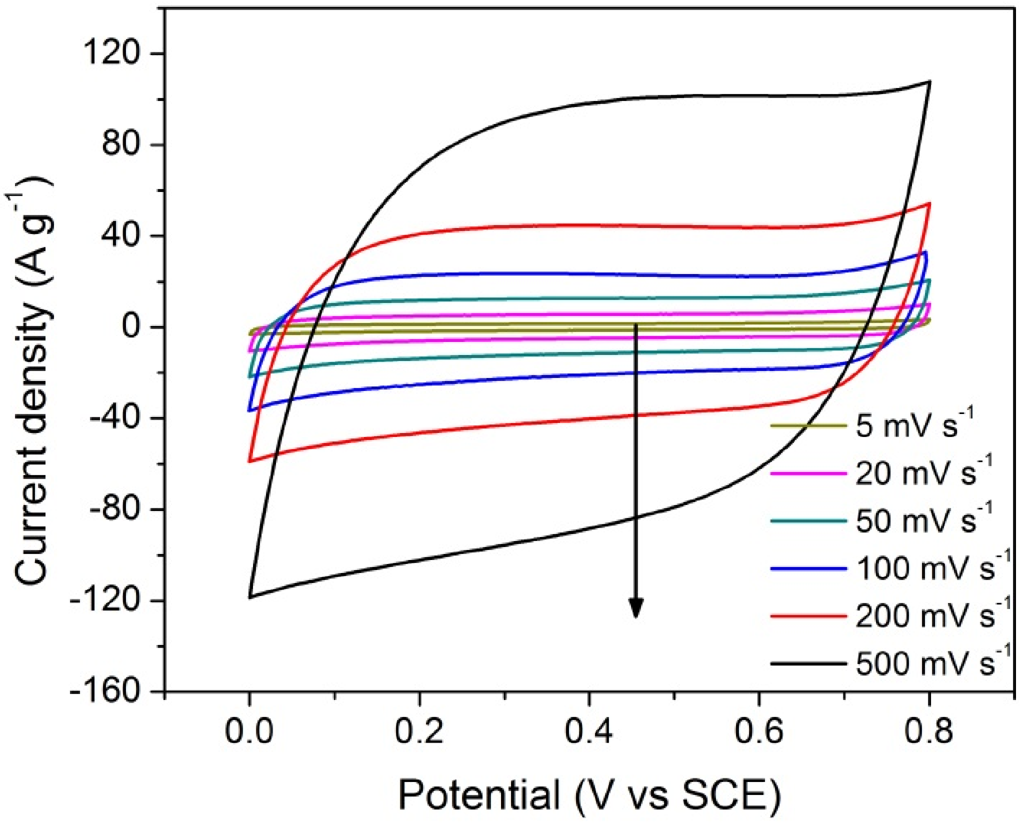

Figure 39. CV curves of MnO_2 at different scan rates (5 – 500 mV s^{-1}).

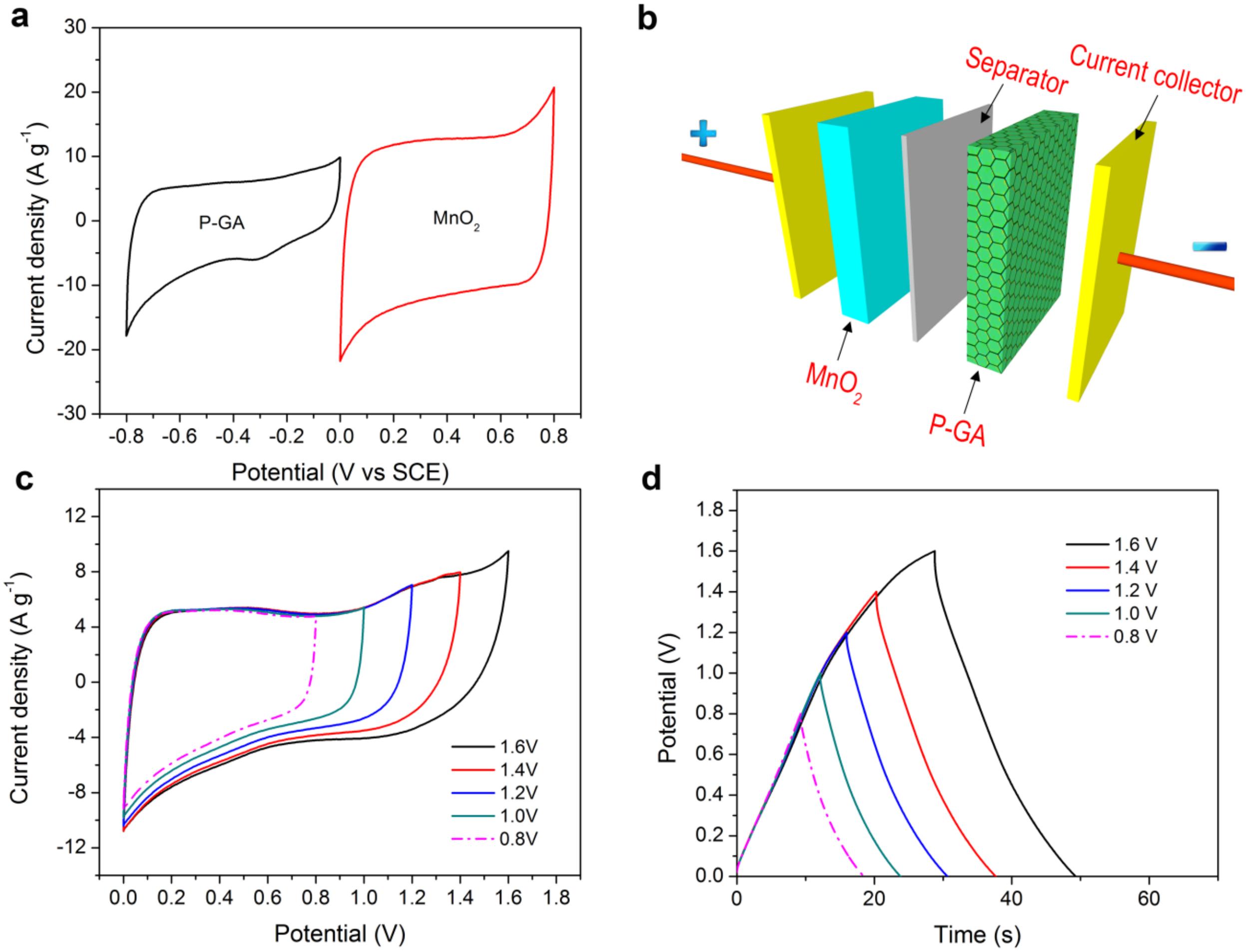

Figure 40. (a) Comparative CV curves of MnO_2 and P-GA electrodes performed in a three-electrode configuration at a scan rate of 50 mV s^{-1}. (b) Schematic of the assembled structure of an ASC based on MnO_2 as cathode and P-GA as anode. (c) CV and (d) GCD curves of an optimized MnO_2//P-GA ASC measured at different voltage windows in a two-electrode configuration.

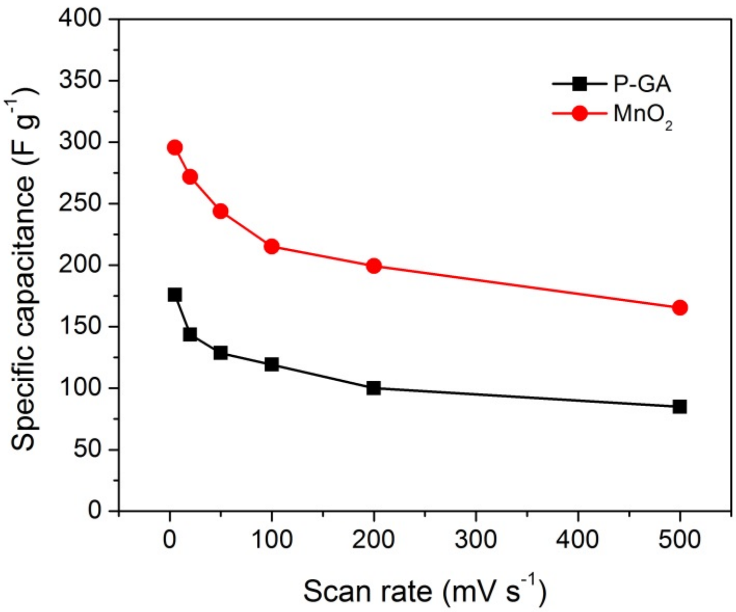

Figure 41. Specific capacitance of MnO_2 and P-GA as a function of scan rate.

7.2.3 Fabrication and characterization of ASCs

An ASC device was then assembled using P-GA as negative electrode and MnO_2 as the positive electrode (assigned as MnO_2//P-GA) as illustrated in Figure 40(b). Figure 40(c) exhibits CV curves of an optimized MnO_2//P-GA ASC at different voltage windows in 0.1 M Na_2SO_4 aqueous solution at scan rate of 100 mV s^{-1}. The assembled ASC shows quasi-rectangular shape even at the voltage window up to 1.6 V, indicating the feasibility of employing P-GA and MnO_2 as negative and positive electrodes respectively and good capacitive behavior of the assembled ASC device. In addition, GCD measurements were also performed to investigate the feasibility of as-assembled MnO_2//P-GA ASC. Figure 40 (e) shows the GCD curves at different voltage windows ranging from 0.8 V to 1.6 V at a current density of 4 A g^{-1}. The GCD curves exhibit stable triangular shape up to 1.6V which further supports the stable electrochemical voltage of the MnO_2//P-GA ASC device. Upon exposure of the ASC device to wider voltage windows (up to 2.0 V) in the GCD test (Figure 42). However, when the voltage windows are higher than 1.6 V, the GCD curves become less symmetrical which considerably reduces the reversibility of the ASCs. Therefore, this study focused on a voltage window of 1.6 V.

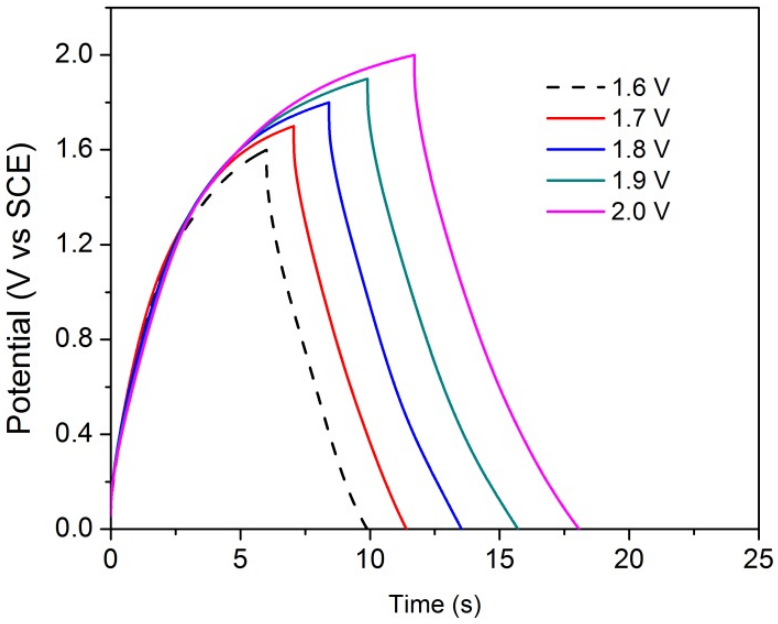

Figure 42. GCD curves of ASC measured at different voltage windows.

Figure 43(a) shows the CV curves of MnO_2//P-GA ASC measured at various scan rates of 5, 20, 50, 100, 200, and 500 mV s^{-1} with a voltage window of 1.6 V. No significant redox peaks are observed indicates ideal capacitive behavior. Moreover, CV profiles remain a relatively rectangular shape without apparent distortion as the scan rate increases from 5 to 500 mV s^{-1}, revealing the favorable fast charge and discharge characteristic for power devices. The maximum specific capacitance for MnO_2//P-GA ASC reaches 108.9 F g^{-1} at a scan rate of 5 mV s^{-1} (Figure 44). Additionally, the specific capacitance still remains at 37.8 F g^{-1} (34.7% retention) even when the scan rate is increased by 100 times to 500 mV s^{-1}. GCD curves of MnO_2//P-GA

ASC at different current densities are shown in Figure 43(b). The good symmetry of the GCD curves validates its efficient capacitive behavior. The electrochemical performance of MnO_2//P-GA ASC is further evaluated using electrochemical impedance spectroscope (EIS) with frequency ranging from 10 mHz to 100 kHz. The Nyquist plots (Figure 43(c) shows a straight line, indicating an ideal capacitive behavior of MnO_2//P-GA ASC. Moreover, the resistance of the device is very close to the intercept of the Nyquist curve on the real axis (the inset of Figure 43(c)) which demonstrates the low internal resistivity of the electrode and good conductivity of the electrolyte. Figure 43(d) shows the Bode plots of the MnO_2//P-GA ASC. The phase angle is close to -90° for frequency up to 1 Hz, suggesting an ideal capacitor is approached for MnO_2//P-GA ASC. The relaxation time (233 ms) is calculated based on the frequency (4.29 Hz) that possesses a phase angle of -45° at which point that the capacitive and resistive impedances are equal.[40] This exceptionally small time constant for the MnO_2//P-GA ASC is competitive compared with other reported values for SCs such as carbon aerogel (2000 ms) [41], activated carbon (700 ms) [42], MnO_2/carbon composite (500 ms) [43], AuPd-MnO_2 core-shell (59 ms) [44], etc.

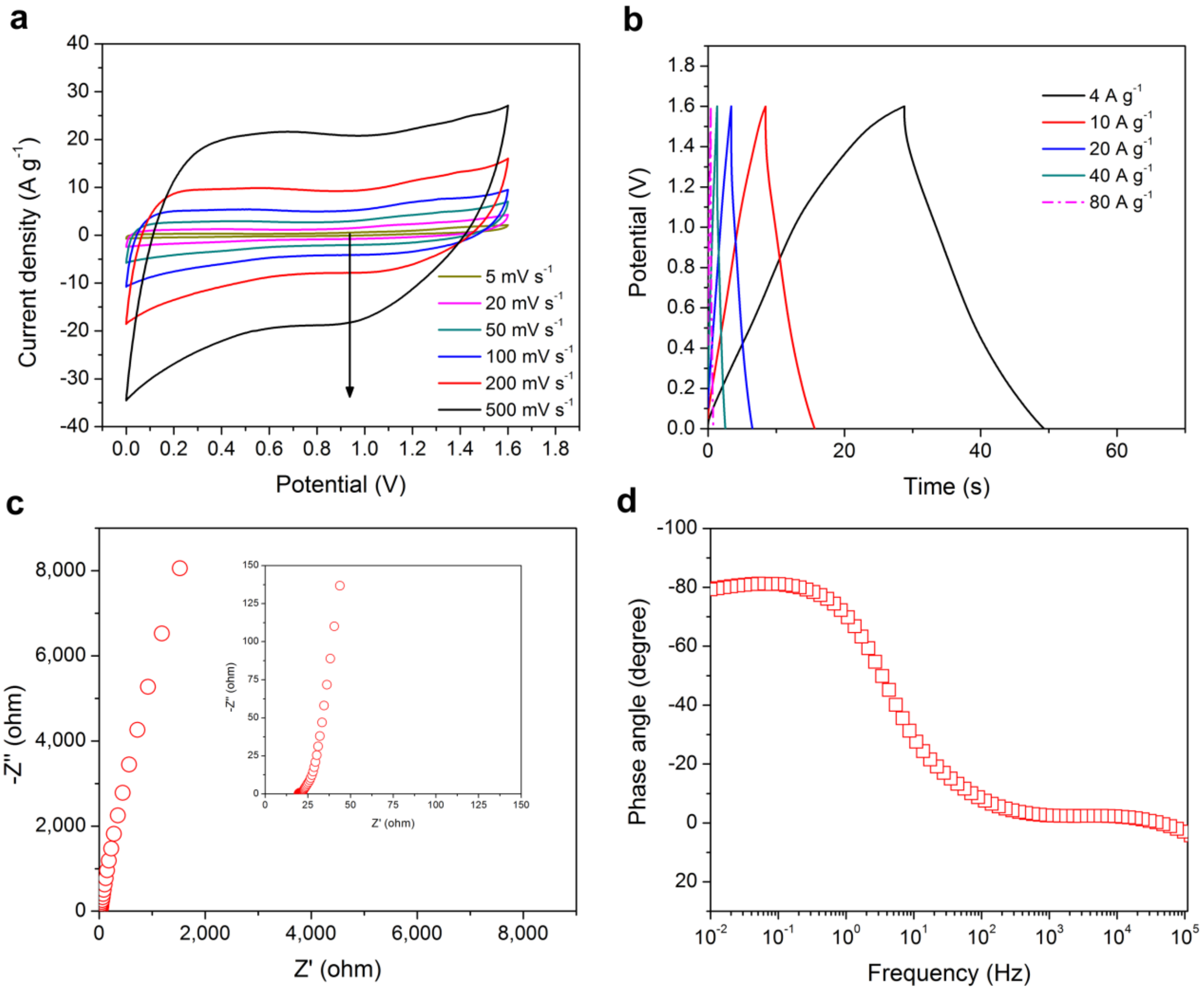

Figure 43. (a) CV curves of MnO_2//P-GA ASC at different scan rates (5 – 500 mV s^{-1}). (b) CV curves of MnO_2//P-GA ASC at different current densities (4 – 80 A g^{-1}). (c) Nyquist and (d) Bode plots for the MnO_2//P-GA ASC.

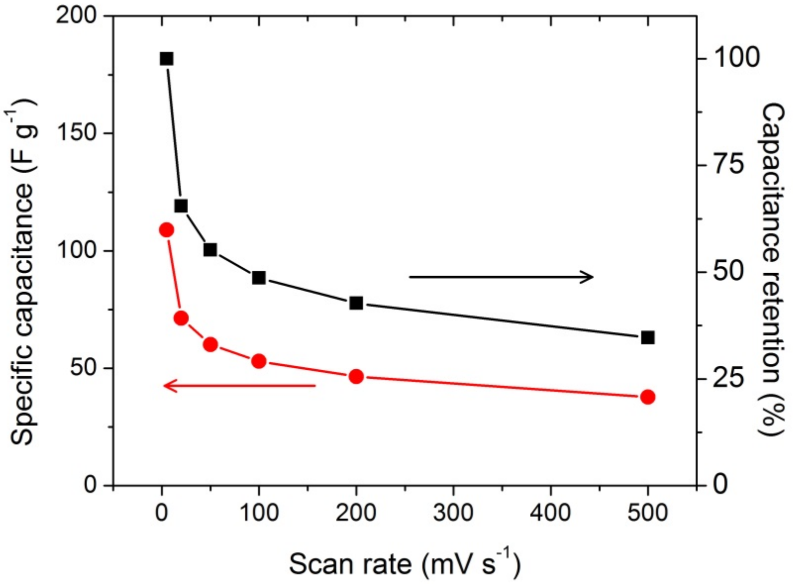

Figure 44. Specific capacitance and capacitance retention for the MnO_2//P-GA ASC as a function of scan rates.

Cycling stablility is a vital characterictic for evaluating the performance of energy storage devices. Figure 45(a) displays the cyclic performance of MnO_2//P-GA ASC at a scan rate of 200 mV s^{-1}. The capacitance still remains at 89.6% of its initial value after 3,000 cycles, suggesting remarkable cycling stability. The two other important parameters, energy density and power densities, have also been widely used to evaluate the performance of energy storge devices. Figure 45 (b) shows Ragone plots (energy density vesus power density) of MnO_2//P-GA ASC. The average energy density is 13.9 Wh kg^{-1} with a power density of 13.3 kW kg^{-1}. These results are higher or comparable to other recently reported values of ASCs, such as MnO_2 nanowire-graphene//graphene (MnO_2 NW-Graphene//Graphene, 7.2 Wh kg^{-1} and 5.0 kW kg^{-1}) [45], nickel hydroxide-graphite//activated graphene oxide ($Ni(OH)_2$-graphite//AGO, 6.9 Wh kg^{-1} and 44.0 kW kg^{-1}) [19], reduced graphene oxide-ruthenium oxide//reduced graphene oxide-polyaniline (RGO-RuO_2//RGO-PANI, 6.7 Wh kg^{-1} and 50.0 kW kg^{-1}) [46], graphene-MnO_2//activated carbon nanofiber (Graphene-MnO_2//ACN, 10 Wh kg^{-1} and 12.0 kW kg^{-1}) [9], and MnO_2//graphene hydrogel (MnO_2//GH, 14.9 Wh kg^{-1} and 10.0 kW kg^{-1}) [34a], etc. Ragone plots (Figure 46) comparing our device to batteries and lithium ion capacitors (LIC) indicates that MnO_2//P-GA ASC has a much higher power density range with a comparable energy density range. Likewise, our device has a much higher energy density range and comparable power density range when compared to electrochemical double layer capacitor (EDLC). To further demonstrate the feasibility of our MnO_2//P-GA ASC, two ASCs were assembled in series to light up a commercially available red light-emitting-diode (LED, 2V) as shown in the inset of Figure 45(b). These promising results for P-GA may lead to other applications such as sensing or catalysis and our fabrication procedure should be generally applicable to other thermally processable precursors.

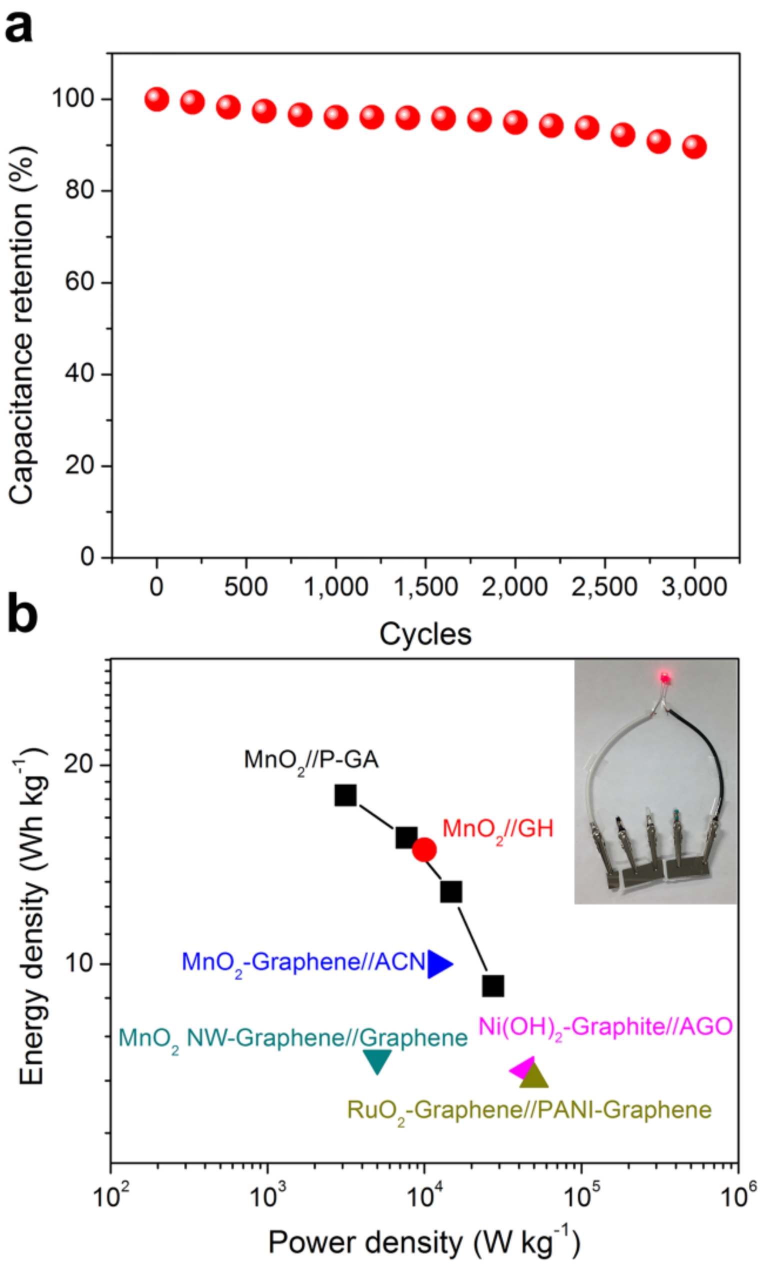

Figure 45. (a) Cycle performance of the device at a scan rate of 200 mv s^{-1}. (b) Ragone plots of MnO$_2$//P-GA ASC compared with other recently reported values of ASCs. The inset shows a LED lighting demonstration, with the diode driven by two devices in series.

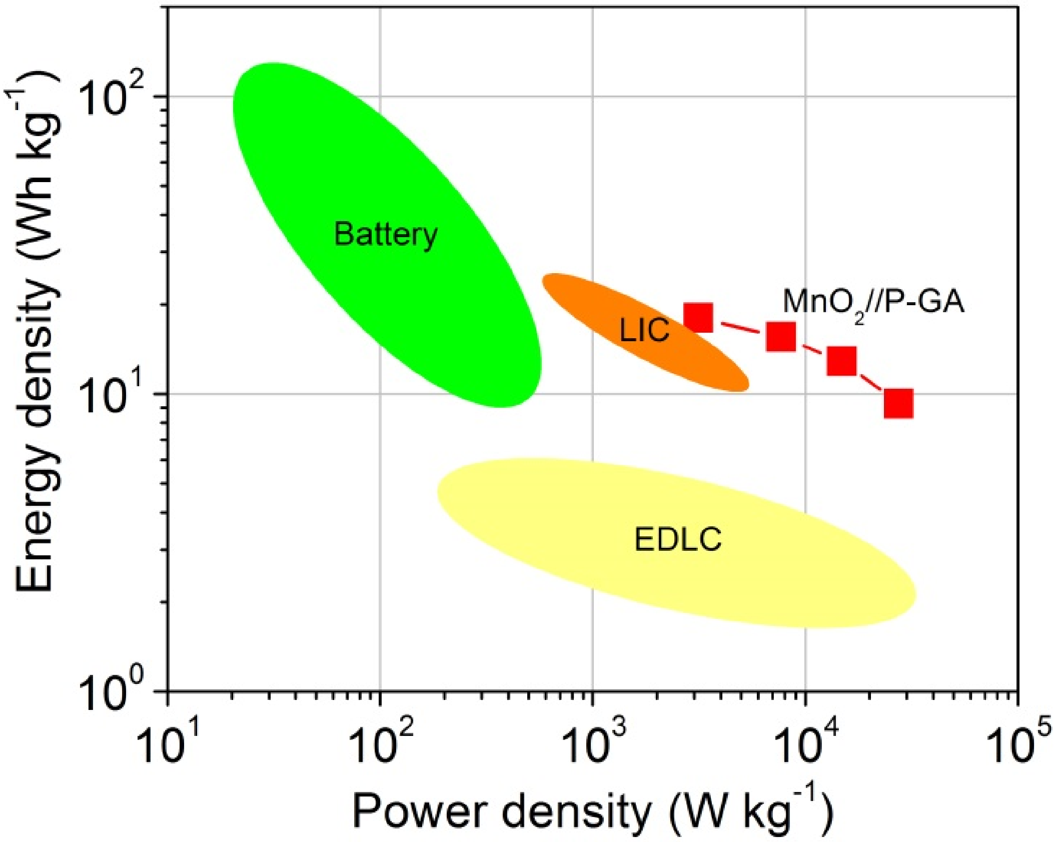

Figure 46. Ragone plots of our device compared with other commercially available devices [20a, 47].

7.3 Conclusion

A novel method to produce GA conformally loaded with Pd nanoparticles was developed. This technique produces P-GA with a high surface area of 328 m^2 g^{-1} and a low electrical resistivity of 16 Ω cm, which is more than a 50 times lower than one without Pd. Electrodes fabricated using P-GA show highly improved electrochemical capacitive behavior than the GA one, which is attributed to the reduced resistivity. Significantly, a high performance ASC based on this P-GA anode and MnO_2 cathode was successfully demonstrated. MnO_2//P-GA ASC shows an average energy and power densities of 13.9 Wh kg^{-1} and 13.3 kW kg^{-1}. These values are substantially enhanced compared to other recently published ASC devices. The employment of P-GA anode for ASCs broadens the pathway of chasing high energy and power densities energy storage devices.

SUMMARY AND OUTLOOK

Motivated by the numerous potential applications of graphene, in this work we have development the primary methods of utilizing the unique properties of graphene in composites. The resulting composites varied widely in form and function but all are dependent on novel developments in processing this relatively new material. In summary, this research focused on two main parts: (1) Studying and utilizing graphene to orient, direct and interface with conjugated polymers in an effort to increase potential device performance and enable facile use of said materials, and (2) Functionalizing graphene aerogels as a high surface area, permeable material with diverse uses.

In the first, a fundamental understanding of P3HT's crystallization was used to establish an understanding of the influence of the presence of graphene on that crystallization. Using QCM, the in situ growth rate of P3HT adsorption selectively on the surface of graphene was seen. This leads to a kinetic interpretation of the crystallization process, providing valuable information for P3HT-graphene composite use.

Using this information, and the expertise of Dr. Khondaker's group to produce uniform RGO electrodes, functioning field-effect transistors with increased performance were fabricated. The increased mobility and on-off ratio are directly related to increased polymer crystallinity and the intimate contact the P3HT has with the underlying graphene. Further, this all comes about due to the strong π-π interaction between graphene and P3HT. The benefit of this procedure is that it is bottom-up self-assembly of organized polymeric structures that, even with carefully controlled annealing have a fundamental crystallinity limit. The process is simple, relatively scalable and energy efficient, as it occurs at >100°C. It can be envisioned that devices that benefit from this type of morphology and with control over the scale and geometries of active materials such as polymer-based solar cells could greatly benefit from this research. Patterning of graphene, transferring it in an organized and reproducible way, and producing complex geometries are active fields of research today and would afford novel geometries from which the bottom-up assembly of P3HT and other conjugated polymers could occur. This leads to exciting new possibilities of cheap and possibly renewable devices utilizing energy sources.

The immediate future of graphene in diverse technologies is already being realized. From large-scale industrial processes such as soil remediation to the high tech fields of single-layer graphene field effect transistors, graphene is still seeing increasing attention from scientists and companies alike. The field effect transistors, sensors and energy storage devices developed in these studies depended entirely on the extraordinary properties of graphene.

The second main part is the functionalization of graphene aerogels with metals. Although several groups have reported loading metal onto the surfaces of graphene, very few do so in graphene aerogels, a high surface area electrically conductive scaffolding. The limitation in this field was that addition sufficient quantity of ionic material in a GO suspension lead to gelation or precipitation. Of these materials, GO was especially sensitive to multivalent metal salts because electrostatic interactions that are normally mutually negative (and therefore repulsive) have an effective linker in the form of cations. The primary novel accomplishment in this aerogel research was that this could be overcome simply by adding a chelating agent such as EDTA or sodium acetate to screen this charge, leaving the GO in stable suspension. Much research has been done decades ago on organic salt-metal interactions but this novel use is only the beginning in this field. Although EDTA and sodium acetate were found to be effective dispersant aids, optimization of the chemistry of these molecules could lead to even higher metal concentrations, and a wider range of metals to use.

From these composites a hydrogen gas sensor and an anode for an asymmetric supercapacitor were developed. The performance of both was made possible by the functionalization of the graphene aerogels with metals nanoparticles. The gas sensor was able to rapidly detect (seconds) 1000 ppm hydrogen gas with rapid recovery (10s of seconds) and do so reproducibility over several cycles. The concentration of maximal efficacy for this system was determined to be ~30mM Pd salt. This metric is important as maximal efficacy for a precious metal that is already a commonly used material for gas sensors related directly to cost efficiency.

Using a wider range of metals, and using other materials that need or can withstand the relatively harsh reduction conditions of GO in the gas phase is an interesting and likely profitable market, as graphene aerogels are ideal candidates as catalyst scaffolding in many applications. Such is possible with the utilization and further optimization of the techniques developed in this research.

APPENDIX A: LIST OF RELEVANT PUBLICATIONS AND PRESENTATIONS

Zhai, L.; Khondaker, S. I.; Thomas, J.; Shen, C.; **McInnis, M.**, “Ordered Conjugated Polymer Nano- and Microstructures: Structure Control for Improved Perfomance of Organic Electronics.” Nano Today 2015, 9 (6), 705-721

Yu, Z.; **McInnis, M.;** Calderon, J.; Thomas, J; Zhai, L., “Functionalized Graphene Aerogel Composites for High-Performance Asymmetric Supercapacitors.” Nano Energy 2015, 11; pp 611-620

Liu, J.; Moo-Young, J.; **McInnis, M.;** Pasquinelli, M.; Zhai, L., “Conjugated Polymer Assemblies on Carbon Nanotubes.” Macromolecules 2014 3 (2), 705-712

Malhotra, A.; **McInnis, M.;** Anderson, J.; Zhai, L., Stimuli-Responsive Conjugated Polymers: From Electronic Noses to Artificial Muscles. In Intelligent Stimuli-Responsive Materials, John Wiley & Sons, Inc.: 2013; pp 423-470.

Anderson, J. M.; **McInnis, M. D**.; Malhotra, A.; Zhai, L., “Aqueous route for the synthesis of platinum, ruthenium and ceria nanoparticles on multi-walled carbon nanotubes for the electrooxidation of methanol and ethanol.” Materials Express 2013, 3 (1), 11-20.

McInnis, M.; Zhai, L., “Conjugated Polymer/Carbon Nanotube Composites.” Reviews in Nanoscience and Nanotechnology 2012, 1 (2), 119-141.

Johns, V. K.; Shi, Z.; Dang, W.; **McInnis, M.;** Weng, Y; Liao, Y., “Photo Retro-Diels-Alder Reactions.” The Journal of Physical Chemistry A (2011, 115 (28), 8093-8099

McInnis, M., “Conjugated Polymer Assemblies on Graphitic Surfaces.” Poster presented at the 244th ACS National Meeting & Exposition (August 19-23, 2012), Philadelphia, PA.

McInnis, M., “Fabrication of Metal Nanoparticle-decorated Graphene Aerogels.” Poster presented at the Florida Space Institute Spacetech 1.0 (September 5, 2014), Rosen College of Hospitality Management.

McInnis, M., “Functionalized Graphene Aerogels.” Poster presented at the 2013 Annual Joint Symposium of the Florida Chapter of the American Vacuum Society and Florida Society for Microscopy (March 4-5, 2014), University of Central Florida.

McInnis, M., “Bottom-up Assembly of Poly(3-hexylthiophene) Nanowires from Graphitic Surfaces for Organic Electronic Devices.” Oral presentation at the 2013 Nanoflorida Conference (September 29-30, 2013), University of Florida.

McInnis, M., “Conjugated Polymer Supramolecular Structures on Graphene for Ordered Heterojunction Solar Cells.” Poster presented at the 2013 Annual Joint Symposium of the Florida Chapter of the American Vacuum Society and Florida Society for Microscopy (March 4-5, 2013), University of Central Florida.

APPENDIX B: PERMISSION FOR COPYRIGHTED MATERIAL

Chapter 7 adapted with permission from: Zenan Yu, Matthew McInnis, Jean Calderon, Sudipta Seal, Lei Zhai, Jayan Thomas, Functionalized graphene aerogel composites for high-performance asymmetric supercapacitors, *Nano Energy*, **2015**, *11,611-620* . Copyright 2015 Elsevier.

Figure 1 used with permission from Geim, A. K.; Novoselov, K. S., The rise of graphene. *Nature Materials* **2007,** *6* (3), 183-191. Copyright 2007 Nature Publishing Group.

Figure 3 used with permission from Ma, W.; Yah, W. O.; Otsuka, H.; Takahara, A., Surface functionalization of aluminosilicate nanotubes with organic molecules. *Beilstein Journal of Nanotechnology* **2012,** *3*, 82-100. Copyright 2012 Beilstein.

Figure 4 used with permission from Liu, J.; Zou, J.; Zhai, L., Bottom-up Assembly of Poly(3-hexylthiophene) on Carbon Nanotubes: 2D Building Blocks for Nanoscale Circuits. *Macromolecular Rapid Communications* **2009,** *30* (16), 1387-1391. Copyright 2009 Wiley.

REFERENCES

1. Geim, A. K.; Novoselov, K. S., The rise of graphene. *Nature Materials* **2007,** *6* (3), 183-191

2. (a) Liu, J.; Zou, J.; Zhai, L., Bottom-up Assembly of Poly(3-hexylthiophene) on Carbon Nanotubes: 2D Building Blocks for Nanoscale Circuits. *Macromolecular Rapid Communications* **2009,** *30* (16), 1387-1391; (b) Zou, J.; Chen, H.; Chunder, A.; Yu, Y.; Huo, Q.; Zhai, L., Preparation of a Superhydrophobic and Conductive Nanocomposite Coating from a Carbon-Nanotube-Conjugated Block Copolymer Dispersion. *Advanced Materials* **2008,** *20* (17), 3337-3341.

3. (a) Arif, M.; Liu, J.; Zhai, L.; Khondaker, S. I., Poly(3-hexylthiophene) crystalline nanoribbon network for organic field effect transistors. *Applied Physics Letters* **2010,** *96* (24), 243304-243304-3; (b) Liu, J.; Arif, M.; Zou, J.; Khondaker, S. I.; Zhai, L., Controlling Poly(3-hexylthiophene) Crystal Dimension: Nanowhiskers and Nanoribbons. *Macromolecules* **2009,** *42* (24), 9390-9393; (c) Liu, J.; Mikhaylov, I. A.; Zou, J.; Osaka, I.; Masunov, A. E.; McCullough, R. D.; Zhai, L., Insight into how molecular structures of thiophene-based conjugated polymers affect crystallization behaviors. *Polymer* **2011,** *52* (10), 2302-2309; (d) Schenning, A. P. H. J.; Meijer, E. W., Supramolecular electronics; nanowires from self-assembled [small pi]-conjugated systems. *Chemical Communications* **2005,** (26), 3245-3258; (e) Grimsdale, A. C.; Müllen, K., The Chemistry of Organic Nanomaterials. *Angewandte Chemie International Edition* **2005,** *44* (35), 5592-5629.

4. Ma, W.; Yah, W. O.; Otsuka, H.; Takahara, A., Surface functionalization of aluminosilicate nanotubes with organic molecules. *Beilstein Journal of Nanotechnology* **2012,** *3*, 82-100.

5. Virkar, A. A.; Mannsfeld, S.; Bao, Z.; Stingelin, N., Organic Semiconductor Growth and Morphology Considerations for Organic Thin-Film Transistors. *Advanced Materials 22* (34), 3857-3875.

6. Sarker, B. K.; Liu, J.; Zhai, L.; Khondaker, S. I., Fabrication of Organic Field Effect Transistor by Directly Grown Poly(3 Hexylthiophene) Crystalline Nanowires on Carbon Nanotube Aligned Array Electrode. *ACS Applied Materials & Interfaces* **2011,** *3* (4), 1180-1185.

7. Joung, D.; Khondaker, S. I., Efros-Shklovskii variable-range hopping in reduced graphene oxide sheets of varying carbon sp(2) fraction. *Physical Review B* **2012,** *86* (23).

8. Hummers Jr, W. S.; Offeman, R. E., Preparation of graphitic oxide. *Journal Of The American Chemical Society* **1958,** *80* (6), 1339-1339.

9. Fan, Z.; Yan, J.; Wei, T.; Zhi, L.; Ning, G.; Li, T.; Wei, F., Asymmetric supercapacitors based on graphene/MnO_2 and activated carbon nanofiber electrodes with high power and energy density. *Advanced Functional Materials* **2011,** *21* (12), 2366-2375.

10. Khomenko, V.; Raymundo-Pinero, E.; Béguin, F., Optimisation of an asymmetric manganese oxide/activated carbon capacitor working at 2V in aqueous medium. *Journal of Power Sources* **2006,** *153* (1), 183-190.

11. (a) Sirringhaus, H.; Tessler, N.; Friend, R. H., Integrated optoelectronic devices based on conjugated polymers. *Science* **1998,** *280* (5370), 1741-1744; (b) Dimitrakopoulos, C. D.; Malenfant, P. R. L., Organic Thin Film Transistors for Large Area Electronics. *Advanced*

Materials **2002,** *14* (2), 99-117; (c) Briseno, A. L.; Mannsfeld, S. C. B.; Jenekhe, S. A.; Bao, Z.; Xia, Y., Introducing organic nanowire transistors. *Materials Today* **2008,** *11* (4), 38-47.

12. (a) Kline, R. J.; McGehee, M. D.; Kadnikova, E. N.; Liu, J.; Fréchet, J. M. J.; Toney, M. F., Dependence of Regioregular Poly(3-hexylthiophene) Film Morphology and Field-Effect Mobility on Molecular Weight. *Macromolecules* **2005,** *38* (8), 3312-3319; (b) Bao, Z.; Dodabalapur, A.; Lovinger, A. J., Soluble and processable regioregular poly(3-hexylthiophene) for thin film field-effect transistor applications with high mobility. *Applied Physics Letters* **1996,** *69* (26), 4108-4110; (c) Kobayashi, S.; Nishikawa, T.; Takenobu, T.; Mori, S.; Shimoda, T.; Mitani, T.; Shimotani, H.; Yoshimoto, N.; Ogawa, S.; Iwasa, Y., Control of carrier density by self-assembled monolayers in organic field-effect transistors. *Nat Mater* **2004,** *3* (5), 317-322; (d) Pal, T.; Arif, M.; Khondaker, S. I., High performance organic phototransistor based on regioregular poly(3-hexylthiophene). *Nanotechnology* **2010,** *21* (32).

13. (a) Sasha, S.; Dmitriy, A. D.; Geoffrey, H. B. D.; Kevin, M. K.; Eric, J. Z.; Eric, A. S.; Richard, D. P.; SonBinh, T. N.; Rodney, S. R., Graphene-based composite materials. *Nature* **2006,** *442* (7100), 282-286; (b) Singh, V.; Joung, D.; Zhai, L.; Das, S.; Khondaker, S. I.; Seal, S., Graphene based materials: Past, present and future. *Progress in Materials Science* **2011,** *56* (8), 1178-1271; (c) Loh, K. P.; Bao, Q.; Eda, G.; Chhowalla, M., Graphene oxide as a chemically tunable platform for optical applications. *Nature Chemistry* **2010,** *2* (12), 1015-1024.

14. Chunder, A.; Liu, J.; Zhai, L., Reduced Graphene Oxide/Poly(3-hexylthiophene) Supramolecular Composites. *Macromolecular Rapid Communications* **2010,** *31* (4), 380-384.

15. Park, Y. D.; Lim, J. A.; Jang, Y.; Hwang, M.; Lee, H. S.; Lee, D. H.; Lee, H.-J.; Baek, J.-B.; Cho, K., Enhancement of the field-effect mobility of poly(3-hexylthiophene)/functionalized carbon nanotube hybrid transistors. *Organic Electronics* **2008,** *9* (3), 317-322.

16. (a) Pang, S.; Tsao, H. N.; Feng, X.; Muellen, K., Patterned Graphene Electrodes from Solution-Processed Graphite Oxide Films for Organic Field-Effect Transistors. *Advanced Materials* **2009,** *21* (34), 3488-+; (b) Becerril, H. A.; Stoltenberg, R. M.; Tang, M. L.; Roberts, M. E.; Liu, Z.; Chen, Y.; Kim, D. H.; Lee, B.-L.; Lee, S.; Bao, Z., Fabrication and Evaluation of Solution-Processed Reduced Graphene Oxide Electrodes for p- and n-Channel Bottom-Contact Organic Thin-Film Transistors. *ACS Nano* **2010,** *4* (11), 6343-6352; (c) Woebkenberg, P. H.; Eda, G.; Leem, D.-S.; de Mello, J. C.; Bradley, D. D. C.; Chhowalla, M.; Anthopoulos, T. D., Reduced Graphene Oxide Electrodes for Large Area Organic Electronics. *Advanced Materials* **2011,** *23* (13), 1558-1562; (d) Lee, C.-G.; Park, S.; Ruoff, R. S.; Dodabalapur, A., Integration of reduced graphene oxide into organic field-effect transistors as conducting electrodes and as a metal modification layer. *Applied Physics Letters* **2009,** *95* (2); (e) Suganuma, K.; Watanabe, S.; Gotou, T.; Ueno, K., Fabrication of Transparent and Flexible Organic Field-Effect Transistors with Solution-Processed Graphene Source-Drain and Gate Electrodes. *Applied Physics Express* **2011,** *4* (2); (f) Lee, J. S.; Kim, N. H.; Kang, M. S.; Yu, H.; Lee, D. R.; Oh, J. H.; Chang, S. T.; Cho, J. H., Wafer-Scale Patterning of Reduced Graphene Oxide Electrodes by Transfer-and-Reverse Stamping for High Performance OFETs. *Small* **2013,** *9* (16), 2817-2825.

17. Wu, X.; Zhou, J.; Xing, W.; Wang, G.; Cui, H.; Zhuo, S.; Xue, Q.; Yan, Z.; Qiao, S. Z., High-rate capacitive performance of graphene aerogel with a superhigh C/O molar ratio. *Journal of Materials Chemistry* **2012,** *22* (43), 23186-23193.

18. (a) Kumar, R.; Varandani, D.; Mehta, B.; Singh, V.; Wen, Z.; Feng, X.; Müllen, K., Fast response and recovery of hydrogen sensing in Pd–Pt nanoparticle–graphene composite layers. *Nanotechnology* **2011,** *22* (27), 275719; (b) Lange, U.; Hirsch, T.; Mirsky, V. M.; Wolfbeis, O. S., Hydrogen sensor based on a graphene – palladium nanocomposite. *Electrochimica Acta* **2011,** *56* (10), 3707-3712.

19. Ji, J.; Zhang, L. L.; Ji, H.; Li, Y.; Zhao, X.; Bai, X.; Fan, X.; Zhang, F.; Ruoff, R. S., Nanoporous Ni(OH)$_2$ thin film on 3D ultrathin-graphite foam for asymmetric supercapacitor. *ACS Nano* **2013,** *7* (7), 6237-6243.

20. (a) Simon, P.; Gogotsi, Y., Materials for Electrochemical Capacitors. *Nature Materials* **2008,** *7* (11), 845-54; (b) Yu, Z.; Duong, B.; Abbit, D.; Thomas, J., Highly Ordered MnO$_2$ Nanopillars for Enhanced Supercapacitor Performance. *Advanced Materials* **2013,** *25* (24), 3302-3306; (c) Wang, G.; Zhang, L.; Zhang, J., A review of electrode materials for electrochemical supercapacitors. *Chemical Society Reviews* **2012,** *41* (2), 797-828; (d) Zhang, L. L.; Zhao, X., Carbon-based materials as supercapacitor electrodes. *Chemical Society Reviews* **2009,** *38* (9), 2520-2531; (e) Yu, Z.; Li, C.; Abbitt, D.; Thomas, J., Flexible, sandwich-like Ag-nanowire/PEDOT: PSS-nanopillar/MnO 2 high performance supercapacitors. *J. Mater. Chem. A* **2014,** *2*, 10923-10929.

21. (a) Miller, J. R.; Simon, P., Electrochemical Capacitors for Energy Management. *Science* **2008,** *321* (5889), 651-652; (b) Miller, J. R.; Burke, A. F., Electrochemical Capacitors: Challenges and Opportunities for Real-World Applications. *Electrochem. Soc. Interface* **2008,** *17* (1), 53-57; (c) Hou, Y.; Cheng, Y.; Hobson, T.; Liu, J., Design and synthesis of hierarchical MnO$_2$ nanospheres/carbon nanotubes/conducting polymer ternary composite for high

performance electrochemical electrodes. *Nano Letters* **2010,** *10* (7), 2727-2733; (d) Yang, Z.; Deng, J.; Chen, X.; Ren, J.; Peng, H., A Highly Stretchable, Fiber-Shaped Supercapacitor. *Angewandte Chemie International Edition* **2013,** *52* (50), 13453-13457.

22. (a) Stoller, M. D.; Ruoff, R. S., Best Practice Methods for Determining An Electrode Material's Performance for Ultracapacitors. *Energy & Environmental Science* **2010,** *3* (9), 1294-1301; (b) Demarconnay, L.; Raymundo-Pinero, E.; Beguin, F., Adjustment of electrodes potential window in an asymmetric carbon/MnO_2 supercapacitor. *Journal Of Power Sources* **2011,** *196* (1), 580-586.

23. Duong, B.; Yu, Z.; Gangopadhyay, P.; Seraphin, S.; Peyghambarian, N.; Thomas, J., High Throughput Printing of Nanostructured Carbon Electrodes for Supercapacitors. *Adv. Mater. Interfaces* **2014,** *1* (1), 1300014.

24. (a) Wang, Y.; Xia, Y., A new concept hybrid electrochemical surpercapacitor: Carbon/$LiMn_2O_4$ aqueous system. *Electrochemistry Communications* **2005,** *7* (11), 1138-1142; (b) Chen, P.-C.; Shen, G.; Shi, Y.; Chen, H.; Zhou, C., Preparation and characterization of flexible asymmetric supercapacitors based on transition-metal-oxide nanowire/single-walled carbon nanotube hybrid thin-film electrodes. *ACS Nano* **2010,** *4* (8), 4403-4411; (c) Xiao, X.; Li, T.; Peng, Z.; Jin, H.; Zhong, Q.; Hu, Q.; Yao, B.; Luo, Q.; Zhang, C.; Gong, L., Freestanding functionalized carbon nanotube-based electrode for solid-state asymmetric supercapacitors. *Nano Energy* **2014,** *6*, 1-9.

25. Yang, P.; Ding, Y.; Lin, Z.; Chen, Z.; Li, Y.; Qiang, P.; Ebrahimi, M.; Mai, W.; Wong, C. P.; Wang, Z. L., Low-Cost High-Performance Solid-State Asymmetric Supercapacitors Based on MnO_2 Nanowires and Fe_2O_3 Nanotubes. *Nano Letters* **2014,** *14*, 731-736.

26. (a) Wang, D.-W.; Li, F.; Cheng, H.-M., Hierarchical porous nickel oxide and carbon as electrode materials for asymmetric supercapacitor. *Journal Of Power Sources* **2008,** *185* (2), 1563-1568; (b) Chen, Y.; Yu, Z.; Chen, Y.; Luo, L.; Wang, X. In *Preparation of NiO nanoparticles as supercapacitor electrode by precipitation using carbon black powder*, Materials for Renewable Energy & Environment (ICMREE), 2011 International Conference on, IEEE: 2011; pp 640-643.

27. (a) Tang, Z.; Tang, C.-H.; Gong, H., A High Energy Density Asymmetric Supercapacitor from Nano-architectured $Ni(OH)_2$/Carbon Nanotube Electrodes. *Advanced Functional Materials* **2012,** *22* (6), 1272-1278; (b) Yan, J.; Fan, Z.; Sun, W.; Ning, G.; Wei, T.; Zhang, Q.; Zhang, R.; Zhi, L.; Wei, F., Advanced asymmetric supercapacitors based on $Ni(OH)_2$/graphene and porous graphene electrodes with high energy density. *Advanced Functional Materials* **2012,** *22* (12), 2632-2641.

28. Zhou, C.; Zhang, Y.; Li, Y.; Liu, J., Construction of high-capacitance 3D CoO@ polypyrrole nanowire array electrode for aqueous asymmetric supercapacitor. *Nano Letters* **2013,** *13* (5), 2078-2085.

29. Wang, X.; Yan, C.; Sumboja, A.; Lee, P. S., High performance porous nickel cobalt oxide nanowires for asymmetric supercapacitor. *Nano Energy* **2014,** *3,* 119-126.

30. Chen, L.-F.; Huang, Z.-H.; Liang, H.-W.; Guan, Q.-F.; Yu, S.-H., Bacterial-Cellulose-Derived Carbon Nanofiber@ MnO_2 and Nitrogen-Doped Carbon Nanofiber Electrode Materials: An Asymmetric Supercapacitor with High Energy and Power Density. *Advanced Materials* **2013,** *25* (34), 4746-4752.

31. Jiang, H.; Li, C.; Sun, T.; Ma, J., A green and high energy density asymmetric supercapacitor based on ultrathin MnO_2 nanostructures and functional mesoporous carbon nanotube electrodes. *Nanoscale* **2012,** *4* (3), 807-812.

32. Sumboja, A.; Foo, C. Y.; Wang, X.; Lee, P. S., Large Areal Mass, Flexible and Free-Standing Reduced Graphene Oxide/Manganese Dioxide Paper for Asymmetric Supercapacitor Device. *Advanced Materials* **2013,** *25* (20), 2809-2815.

33. (a) Zhu, Y.; Murali, S.; Cai, W.; Li, X.; Suk, J. W.; Potts, J. R.; Ruoff, R. S., Graphene and graphene oxide: synthesis, properties, and applications. *Advanced Materials* **2010,** *22* (35), 3906-3924; (b) Yoo, J. J.; Balakrishnan, K.; Huang, J.; Meunier, V.; Sumpter, B. G.; Srivastava, A.; Conway, M.; Mohana Reddy, A. L.; Yu, J.; Vajtai, R., Ultrathin planar graphene supercapacitors. *Nano Letters* **2011,** *11*, 1423-1427; (c) Sun, Y.; Wu, Q.; Shi, G., Graphene based new energy materials. *Energy & Environmental Science* **2011,** *4* (4), 1113-1132; (d) Chen, T.; Xue, Y.; Roy, A. K.; Dai, L., Transparent and Stretchable High-Performance Supercapacitors Based on Wrinkled Graphene Electrodes. *ACS Nano* **2014,** *8* (1), 1039-1046; (e) Choi, H.-J.; Jung, S.-M.; Seo, J.-M.; Chang, D. W.; Dai, L.; Baek, J.-B., Graphene for energy conversion and storage in fuel cells and supercapacitors. *Nano Energy* **2012,** *1* (4), 534-551; (f) Chen, P.; Yang, J.-J.; Li, S.-S.; Wang, Z.; Xiao, T.-Y.; Qian, Y.-H.; Yu, S.-H., Hydrothermal synthesis of macroscopic nitrogen-doped graphene hydrogels for ultrafast supercapacitor. *Nano Energy* **2013,** *2* (2), 249-256.

34. (a) Gao, H.; Xiao, F.; Ching, C. B.; Duan, H., High-performance asymmetric supercapacitor based on graphene hydrogel and nanostructured MnO_2. *Acs Applied Materials & Interfaces* **2012,** *4* (5), 2801-2810; (b) Gong, Y.; Yang, S.; Zhan, L.; Ma, L.; Vajtai, R.; Ajayan,

P. M., A Bottom-Up Approach to Build 3D Architectures from Nanosheets for Superior Lithium Storage. *Advanced Functional Materials* **2014,** *24* (1), 125-130; (c) Cao, X.; Yin, Z.; Zhang, H., Three-Dimensional Graphene Materials: Preparation, Structures and Application in Supercapacitors. *Energy & Environmental Science* **2014,** *7*, 1850-1865.

35. (a) Wu, X.-L.; Wen, T.; Guo, H.-L.; Yang, S.; Wang, X.; Xu, A.-W., Biomass-Derived Sponge-like Carbonaceous Hydrogels and Aerogels for Supercapacitors. *ACS Nano* **2013,** *7* (4), 3589-3597; (b) Wu, Z. S.; Winter, A.; Chen, L.; Sun, Y.; Turchanin, A.; Feng, X.; Müllen, K., Three-Dimensional Nitrogen and Boron Co-doped Graphene for High-Performance All-Solid-State Supercapacitors. *Advanced Materials* **2012,** *24* (37), 5130-5135; (c) Cong, H.-P.; Ren, X.-C.; Wang, P.; Yu, S.-H., Macroscopic multifunctional graphene-based hydrogels and aerogels by a metal ion induced self-assembly process. *ACS Nano* **2012,** *6* (3), 2693-2703.

36. Okamoto, Y., Density-functional calculations of icosahedral M_{13} (M= Pt and Au) clusters on graphene sheets and flakes. *Chemical Physics Letters* **2006,** *420* (4), 382-386.

37. Liu, F.; Song, S.; Xue, D.; Zhang, H., Folded structured graphene paper for high performance electrode materials. *Advanced Materials* **2012,** *24* (8), 1089-1094.

38. Nutt, M. O.; Heck, K. N.; Alvarez, P.; Wong, M. S., Improved Pd-on-Au bimetallic nanoparticle catalysts for aqueous-phase trichloroethene hydrodechlorination. *Appl. Catal. B: Environ.* **2006,** *69* (1), 115-125.

39. (a) Qian, H.; Kucernak, A. R.; Greenhalgh, E. S.; Bismarck, A.; Shaffer, M. S., Multifunctional structural supercapacitor composites based on carbon aerogel modified high performance carbon fiber fabric. *Acs Applied Materials & Interfaces* **2013,** *5* (13), 6113-6122; (b) Zhang, X.; Sui, Z.; Xu, B.; Yue, S.; Luo, Y.; Zhan, W.; Liu, B., Mechanically strong and

highly conductive graphene aerogel and its use as electrodes for electrochemical power sources. *Journal Of Materials Chemistry* **2011,** *21* (18), 6494-6497; (c) Gao, K.; Shao, Z.; Wang, X.; Zhang, Y.; Wang, W.; Wang, F., Cellulose nanofibers/multi-walled carbon nanotube nanohybrid aerogel for all-solid-state flexible supercapacitors. *RSC Advances* **2013,** *3* (35), 15058-15064.

40. Taberna, P.; Simon, P.; Fauvarque, J.-F., Electrochemical characteristics and impedance spectroscopy studies of carbon-carbon supercapacitors. *Journal Of The Electrochemical Society* **2003,** *150* (3), A292-A300.

41. Rasines, G.; Lavela, P.; Macías, C.; Haro, M.; Ania, C.; Tirado, J., Electrochemical response of carbon aerogel electrodes in saline water. *Journal Of Electroanalytical Chemistry* **2012,** *671*, 92-98.

42. Pech, D.; Brunet, M.; Durou, H.; Huang, P.; Mochalin, V.; Gogotsi, Y.; Taberna, P.-L.; Simon, P., Ultrahigh-power micrometre-sized supercapacitors based on onion-like carbon. *Nat. Nanotechnol.* **2010,** *5* (9), 651-654.

43. Yuan, L.; Lu, X. H.; Xiao, X.; Zhai, T.; Dai, J.; Zhang, F.; Hu, B.; Wang, X.; Gong, L.; Chen, J., Flexible Solid-State Supercapacitors Based on Carbon Nanoparticles/MnO_2 Nanorods Hybrid Structure. *ACS Nano* **2012,** *6* (1), 656-661.

44. Yu, Z.; Thomas, J., Energy Storing Electrical Cables: Integrating Energy Storage and Electrical Conduction. *Advanced Materials* **2014,** *26* (25), 4279-4285.

45. Wu, Z.-S.; Ren, W.; Wang, D.-W.; Li, F.; Liu, B.; Cheng, H.-M., High-energy MnO_2 nanowire/graphene and graphene asymmetric electrochemical capacitors. *ACS Nano* **2010,** *4* (10), 5835-5842.

46.	Zhang, J.; Jiang, J.; Li, H.; Zhao, X. S., A high-performance asymmetric supercapacitor fabricated with graphene-based electrodes. *Energy & Environmental Science* **2011,** *4* (10), 4009-4015.

47.	(a) Amatucci, G. G.; Badway, F.; Du Pasquier, A.; Zheng, T., An asymmetric hybrid nonaqueous energy storage cell. *Journal of the Electrochemical Society* **2001,** *148* (8), A930-A939; (b) Sivakkumar, S.; Pandolfo, A., Evaluation of lithium-ion capacitors assembled with pre-lithiated graphite anode and activated carbon cathode. *Electrochimica Acta* **2012,** *65*, 280-287.